ADVANCEMENTS IN MODELING AND SIMULATING NONADIABATIC DYNAMICS IN ELECTROCHEMICAL SYSTEMS

Alec Coffman

A DISSERTATION

in

Chemistry

Presented to the Faculties of the University of Pennsylvania

in

Partial Fulfillment of the Requirements for the

Degree of Doctor of Philosophy

2022

Supervisor of Dissertation

Dr. Joseph E. Subotnik,
Edmund J. and Louise W. Kahn Endowed Term Professor of Chemistry

Graduate Group Chairperson

Dr. Daniel J. Mindiola,
Brush Family Professor of Chemistry

Dissertation Committee

Dr. Jeffery G. Saven, Professor of Chemistry
Dr. Zahra Fakhraai, Associate Professor of Chemistry
Dr. Cherie Kagan, Professor of Electrical And Systems Engineering

ACKNOWLEDGEMENT

No other individual would be fit to be acknowledged here first except for my advisor, Dr. Joseph Subotnik. His support throughout graduate school, both academically and personally, could not be overstated. The intellectual curiosity that Joe brings to every scientific discussion is infectious, and has made the often daunting task of scientific research a pleasant experience at every turn. The way he addresses research problems and how he thinks about questions from multiple angles has deeply impacted my own research, and more importantly given me the skills to continue on with my own research career. In addition, Joe has fostered a supportive and understanding work environment, which is in no small part due to the outstanding quality of his overall character. I consider myself eminently fortunate to have had Joe as an advisor, and his guidance has been and will continue to be a large part of any successes I can claim to have in my scientific career.

I would also like to thank my committee members, Dr. Jeffery Saven, Dr. Zahra Fakhraai, and Dr Cherie Kagan. Their feedback has been consistently valuable, and I appreciate all of their time and effort throughout my graduate school career. In addition, I would like to thank the many members of the Subotnik group that I have had the pleasure of working alongside; Dr. Vale Cofer-Shabica, Dr. Hsing-Ta Chen, Dr. Tian Qiu, Dr. Zuxin Jin, Dr. Tao Li, Dr. Gaohan Miao, Dr. Nicole Bellonzi, Dr. Wenjie Dou, Dr. Amber Jain, Dr. Gregory Medders, Hung-Hsuan Teh, Zeyu Zhou, Vishikh Athavale, Junhan Chen, Yanze Wu, and Samuel May. Apologies to any other individuals I may have forgotten, the above list is certainly in no way exhaustive.

ABSTRACT

ADVANCEMENTS IN MODELING AND SIMULATING NONADIABATIC DYNAMICS IN ELECTROCHEMICAL SYSTEMS

Alec Coffman

Dr. Joseph E. Subotnik

Current methods for modeling electron transfer (ET) dynamics in electrochemical systems rely on boundary condition based methods that often obfuscate any nonadiabatic effects. However, these nonadiabatic effects can play critical roles in many key electrochemical systems, such as ET events coupled to proton transfer, or systems where ET occurs between metal adsorbed redox species and the metal. In this dissertation we present new methods and algorithms for modeling and simulating electrochemical systems exhibiting nonadiabatic effects. First, we examine whether electron friction dynamics can be used in lieu of surface hopping generally for nonadiabatic dynamics. We find that electronic friction is only applicable in specific situations, and that in general a broadened classical master equation solved with surface hopping must be applied in the weak molecule-metal coupling limit. Next, we outline a surface hopping approach for modeling sweep voltammetry experiments, and show a technique for mapping multidimensional, diffusional electrochemical systems to reduced, lower dimensional systems. This surface hopping approach is used to study proton coupled electron transfer (PCET), whereby nuclear quantum effects are incorporated through an explicit proton coordinate. Finally, we present a spatially grid-free algorithm for simulating the above electrochemical systems (including systems where inner-sphere effects are included, such as adsorption), and also demonstrate its computational efficacy in comparison to current simulation techniques common in the field of electrochemistry.

TABLE OF CONTENTS

LIST OF TABLES

LIST OF ILLUSTRATIONS

CHAPTER 1

Introduction

1.1. Born-Oppenheimer Approximation and Nonadiabatic Dynamics

In the field of quantum chemistry, the dynamics and evolution of any quantum system can be fully described by solution of the time-independent Schrödinger equation,

$$i\hbar\frac{\partial\Psi}{\partial t} = \hat{H}\Psi \tag{1.1}$$

where $\hat{H}$ is the total system Hamiltonian, and Ψ is the combined nuclear-electronic wavefunction representing the system of interest. Exact solutions for the above equation exist in principal, but often times one is limited by computational feasibility for all but the most simple and trivial of systems. A common aim in theoretical chemistry is the development of methods, techniques, and algorithms for solving the above equation, with the goal of minimizing computational resources. Additionally, one would hope to solve the above equation making approximations that do not obscure the actual dynamics of the system under study. To that end, a common approximation that has been employed throughout the chemical literature is the Born-Oppenheimer approximation.

The basis of the Born-Oppenheimer approximation is that, given that electrons are several orders of magnitude smaller in size than nuclei, electron motion is much faster than nuclear motion and the two can be separated. Stated another way, electron motion is usually so much faster than nuclear motion that perturbations to the electronic part of the system by the nuclear part will be small on the timescale of electronic motion. This separation of timescale between the electron and nuclear motion allows for one to map each unique electron state to a corresponding electron energy surface, which itself will be a function of the nuclear configuration. Mathematically, this means that the total Hamiltonian can be cast into terms representing the electronic and nuclear subsystems ($\hat{H}^{el}$ and $\hat{H}^{nuc}$ for short),

with no terms representing mixing or interaction between the two sets. This separation of $\hat{H}$ means that the total wavefunction can also be simplified, represented by a product of electronic and nuclear wavefunctions, $\Psi = \psi_{el}\psi_{nuc}$. The electronic part of the system can now be diagonalized and solved first, using the nuclear positions as parameters, leading to a set of electronic solutions,

$$\hat{H}_i^{el}(\mathbf{R})\,|\psi_i\rangle = E_i^{el}(\mathbf{R})\,|\psi_i\rangle\,, \tag{1.2}$$

where $\mathbf{R}$ are nuclear positions, and the index i corresponds to the different possible eigenstates of the diagonalized electronic Hamiltonian. These electronic states give rise to a nuclear-position parameterized adiabatic potential energy surface (PES), E_i^{el}, where the adiabatic states $|\psi_i\rangle$ form an orthonormal set. Now, in the Born-Oppenheimer approximation, the assumption is that only the lowest energy electronic state is important, and dynamics can be propagated on this sole adiabatic PES. Additionally, there exists no energy transfer between nuclei and electron degrees of freedom, and the different electronic states are not coupled. Normally, the adiabatic nature of nuclear perturbations is sufficient for many systems, but this approximation can fail in many critical circumstances. Systems where electronic-nuclear coupling are significant or multiple electronic states are accessible energetically violate this adiabatic approximation. These systems allow for energy exchange between electronic and nuclear degrees of freedom, giving rise to nonadiabatic processes. Nonadiabatic dynamics are common throughout chemistry, arising often in photochemistry, catalysis, energy conversion, and more.

Given the importance of these chemical systems, a host of different methods exist to deal with nonadiabatic effects. One such approach is known as Ehrenfest dynamics, where the contributions of multiple electronic PESs are averaged, giving rise to a potential of mean force (PMF). Dynamics are then propagated along this single PMF, analogous to the adiabatic case, where the original adiabatic PES is replaced with the weighted PMF. While this method is computationally one of the simplest approaches, often times critical information

can be lost upon averaging multiple surfaces or neglecting transitions between adiabatic states. A large catalog of methods exist that extend beyond the simple Ehrenfest picture, but we will limit ourselves to two of the more notable techniques in this work.

The first is fewest switches surface hopping (FSSH), where nuclear motion is propagated along a single adiabatic PES at a given time, but there exists the discrete possibility of "hops" between adiabatic surfaces at each time. In the original FSSH paper by Tully[1], a trajectory is initialized on a given adiabat, where the nuclear positions and momenta are evolved along a single adiabatic surface, while the electronic wavefunction is evolved in time using the Schrödinger equation. The chance of hopping (switching adiabatic surfaces) between electronic states i and j is related at each timestep to the electronic wavefunction amplitudes, $c_{i/j}$,

$$\begin{aligned} g_{i\to j} &= max[0, \delta t \frac{\dot{\rho}_{jj}}{\rho_{ii}}] \\ p_{ij} &= c_i c_j^*, \end{aligned} \tag{1.3}$$

where $g_{i\to j}$ is the probability of switching from adiabatic surface i to adiabatic surface j. Additionally, to guarantee energy conservation, the momentum is rescaled along the direction of the derivative coupling,

$$d_{ik} = \frac{\langle \psi_i | \frac{\partial H}{\partial x} | \psi_j \rangle}{E_j - E_i}. \tag{1.4}$$

Over the many years since Tully's original work, advancements have been made to surface hopping techniques, but most approaches still rely on some form of this basic ansatz above. For example, extensions of the above method allow for surface hopping dynamics to be performed between a molecule and a metal with a continuum of electronic states, where momentum rescaling is no longer needed, as energy is not strictly conserved in the system due to dissipation in the electronic bath.

The second method we will focus on is electronic friction, whereby dynamics are propagated along an adiabatic PMF (similar to Ehrenfest), but there is also a perturbative frictional

force (and associated random force) that arises from the presence of the additional electronic states. While many different methods exist for deriving the electronic friction tensor, it has recently been shown that all of these approaches emerge from one universal electronic friction tensor, based on the quantum classical Liouville equation[2,3,4]. Furthermore, electronic friction methods rely on a slow velocity approximation, which would require fast equilibration. This condition suggests that electronic friction should not be applicable in the low nonadiabatic coupling limit, however recent work[5] has shown that under certain conditions electronic friction can successfully capture nonadiabatic dynamics in the weak coupling limit. The universality of the electronic friction tensor becomes even more interesting in the case of nonadiabatic dynamics of molecule-metal interfaces, a critical part of many novel chemical systems. After all, electron friction is the first order correction to the Born-Oppenheimer approximation for a molecule in the presence of a manifold of electronic states that relax fast relative to other timescales in the system. Given that electronic friction dynamics can easily be modeled with a modified Fokker-Planck equation, and that evidence exists that under specific conditions one can use this approach for modeling a wide coupling regime of nonadiabatic dynamics, one may ask the question; what is the best algorithm/method for modeling nonadiabatic dynamics, specifically in the case of molecule-metal systems? Is it possible to use the universal electronic friction method, despite the fact that its parameter range of validity is not as well documented, or is it better to use the more general surface hopping technique, which lacks a rigorous connection to the QCLE or fundamental derivation like electronic friction? The first thrust of this thesis will set out to address this question, as a means of setting the stage for studying electrochemical systems, where modeling nonadiabatic molecule-metal interactions will be of utmost significance.

1.2. Simulating Electrochemical Voltammetry

Typical voltammetry experiments offer some of the broadest and deepest methods for extracting useful information from and for understanding electrochemical systems. The combination of physical factors (how voltage is change with respect to time, diffusional effects,

ET between redox species and electrode, etc.), and the wide energy/time-scales that they occur over give rise to surprisingly rich diagnostic chemistry. Two of the most common voltammetry techniques that are employed are linear sweep and cyclic voltammetry (LSV and CV), where an external overpotential is varied linearly with time, and the resulting current from this applied overpotential is recorded. In LSV the voltage is usually ramped from a large negative/positive overpotential to a large positive/negative overpotential, while CV extends LSV by returning back to the original starting overpotential. The current vs. potential plot that arises from this experiment provides valuable information about the electrochemical ET in the system, both qualitative and quantitative. For example, the shape, number, and symmetry of peaks in a CV experiment can reveal the electron stoichiometry of ET, the presence of redox intermediates, and whether the ET occurs in solution or when the molecule is electrode-adsorbed. Multiple replicates and calibrations curves of LSV and CV can also be carried out to infer quantitative information about the system, such as the value of the diffusion constant for the redox species, or the bulk concentration of redox species in an unknown system. Additionally, sweep voltammetry experiments are often easy to perform experimentally, and do not perturb or make permanent, irreversible changes to all but the most sensitive of electrochemical systems. Because of the broad utility and application of voltammetry in electrochemistry, and the need to have methodology that allows for comparison to and predictions from experiment, accurate and efficient numerical simulation of sweep voltammetry experiments is of paramount importance.

Despite all the listed advantages of sweep voltammetry, computational methods for modeling ET in sweep voltammetry are lacking in rigor in comparison to many other branches of theoretical chemistry. First, a brief overview of simulating electrochemical voltammetry is warranted; see Fig. 1.1 for a schematic representation. Sweep voltammetry experiments are carried out by modeling redox species mass transfer with a diffusion equation,

$$\frac{\partial c_i}{\partial t} = D_i \frac{\partial^2 c_i}{\partial x^2}, \tag{1.5}$$

where c is the concentration of redox species i and D_i is the diffusion constant for the redox species i, and ET is then incorporated by enforcement of spatial boundary conditions at the electrode surface (often taken to be $x = 0$). While there exist multiple types of boundary conditions that can be used (Nernstian, Butler-Volmer, Marcus-Hush-Chidsey), they all eventually reduce to one or two parameter generalizations that obscure much of the molecular physics of the actual ET event. A high-level method for simulating sweep voltammetry would therefore allow for complicated ET dynamics to be modeled. One natural way to imagine doing this is by formulating a classical master equation for the molecule-metal Hamiltonian of common electrode-redox species electrochemical systems, which yields an analog to Eqn. 1.5,

$$\frac{\partial c_i}{\partial t} = D_i \frac{\partial^2 c_i}{\partial x^2} - k_f c_i + k_b c_j, \tag{1.6}$$

where species j is the oxidized/reduced form of species i, after undergoing ET with the electrode. Now, ET dynamics can be encapsulated into entirely general rate constants k_f and k_b, and the above master equation can be solved with a surface hopping algorithm. Illustrating the equivalence of this method to the current orthodoxy for simulating electrochemical voltammetry experiments, along with extending it to higher dimensional diffusional systems, will be the next focus of this thesis.

1.3. New Methods in Electrochemistry

1.3.1. Quantum Nuclear Effects

Electrochemical voltammetry can often be utilized to understand complex systems in similar branches of chemistry. For example, ET in many biological systems is believed to be intimately coupled to quantized proton motion. One way to better understand to these processes is to study analogous model systems using voltammetry experiments. However, studies like this would require an *a priori* knowledge of how to model systems that engage in this proton coupled electron transfer (PCET). While many advancements have been made in recent years to model PCET in general, few applications have attempted to model it ex-

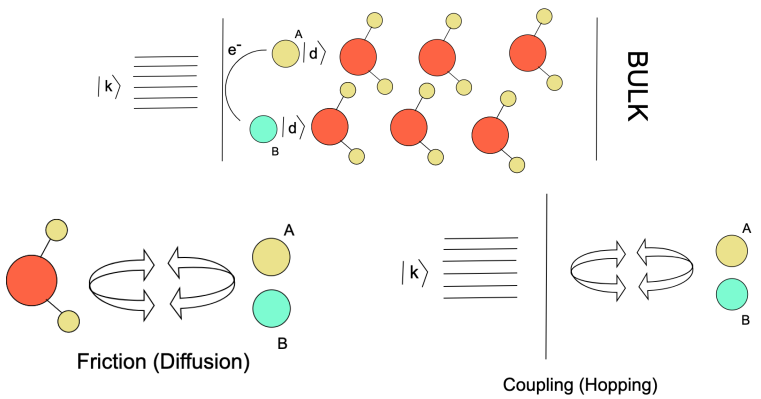

Figure 1.1: Schematic illustration of voltammetry simulations. A and B are the oxidized and reduced forms of an arbitrary redox species, while the the other molecules are solvent molecules (water, as one example). $|k\rangle$ indexes the continuum of electronic states in the metal electrode, while **BULK** signifies the bulk system, far away from the electrode surface. Diffusional effects arise from frictional interactions between the redox species and the solvating molecules, while electronic coupling between the redox species and the electrode lead to "hops", whereby an electron is transferred from the molecule to the metal (or vice-versa).

plicitly in an electrochemical setting, while simultaneously coupled to both diffusive effects and time-varying overpotentials.

Despite being no unique way to generate a theory of voltammetric PCET, there exist many possible routes to formulating such a setup. One way is to utilize a combined quantum classical Liouville equation-classical master equation (QCLE-CME) method. In this treatment, one would start with an exact quantum Liouville equation (QLE) for the total density matrix of the electrochemical system (molecular electronic and vibronic states, plus both a phononic and electronic bath) $\rho(t)$, and use the Born-Markovian approximation to yield a reduced density matrix, $\rho(t) = \rho_b^{eq} \otimes \rho_s(t)$. Here, ρ_b^{eq} is the equilibrium density matrix of the bath and $\rho_s(t)$ is the reduced density matrix of the system. Casting the time evolution of this density matrix into a "Redfield equation", and then Wigner transforming over everything except the quantized coordinate, one arrives at the QCLE for the vibronic states of the system. Under relatively permissive assumptions, this QCLE can be extended to a combined QCLE-CME that can be solved with surface hopping. The next facet of this thesis will be a rigorous derivation of the approach outlined above, complete with a pedagogical

treatment for a general electrochemistry audience that may not be eminently familiar with these approaches from theoretical chemistry. This QCLE-CME will then be used to gain a better understanding of electrochemical PCET, and to determine whether signatures of PCET can solely be determined by analysis of sweep voltammetry experiments.

1.3.2. Grid-Free Voltammetry Simulation

The voltammetry simulation methods discussed in the previous sections all rely on solving ordinary differential equations (ODEs), discretized in both time and space. These discretized ODEs are then solved simultaneously to yield concentrations of redox species at all times and positions. The computational time and effort to numerically solve coupled ODEs goes up precipitously as the number of equations increases. Further complicating matters is that ODEs in voltammetry simulations are often stiff in nature, due to the large separation in scale between the timescales of diffusion, voltage sweeping, and ET. Stiff ODEs are notorious for causing numerical instabilities, and often preclude the simple simulation of complicated voltammetric ET beyond the simplest one electron cases. Additionally, much of the interesting physics in voltammetry experiments occurs very near to the electrode surface, at distances on the molecular scale. Solving coupled, stiff ODEs to determine concentrations far away from the electrode is unfortunately necessary for accurate determination of the redox species concentration near the electrode, and an inordinate amount of computational time and effort is required to acquire these full concentration profiles.

A more desirable approach would therefore involve only determining the concentration nearest to the electrode, and abandon the notion of needing to solve stiff ODEs for positions in space that offer little dynamical info about the ET process. To that end, one can use a Green's function approach and invoke Duhamel's principle to cast diffusion equations of the form in Eqn. 1.6 as an exact integral equation. By deft handling of the resultant singularity in the heat kernel of the Green's function integral, an exact solution for the redox species concentration near the electrode can be found. This method removes the need for

a spatial grid for the concentration of redox species, and relies only on model parameters, initial conditions, and the prior time evolution of the concentration to calculate any future concentration. In addition to vastly improving computation time compared to coupled ODE methods, this approach also opens up avenues for simulating complicated, inner-sphere effects in voltammetry, such as ET between electrode-adsorbed redox species. The final aim of this thesis will be a punctilious derivation of this integral expression for voltammetry simulations, benchmarking it against algorithms in electrochemistry, and extending it to the case of adsorbed voltammetry.

1.4. Outline

In chapter 2 we examine cases where electronic friction dynamics have previously matched surface hopping dynamics in regimes where electronic friction was expected to fail. We look at model systems that break the conditions that allowed for this unexpected equivalence, in an effort to diagnosis when exactly electronic friction dynamics correctly model nonadiabatic effects. Our findings are that electronic friction may fail if there are multiple potential reactive pathways, giving rise to different hopping locations in phase space. Specifically, electronic friction requires the condition that the bath and reaction coordinates are separable, and that the Condon approximation is valid along the generalized reaction coordinate. These findings are evinced by simulation with model systems, and reinforced by analytical derivations carried out originally in this work. This project informs all future work in the thesis, as the discoveries made in this chapter support the rationale in future chapters to restrict our nonadiabatic dynamics methodology to those that can be solved with surface hopping dynamics.

In chapter 3 we present a generalized approach for simulating electron transfer in multidimensional electrochemical systems, with an emphasis on modeling sweep voltammetry experiments. We show that our generalized approach is mathematically equivalent to canonical, boundary condition based approaches currently employed in the electrochemical

literature, and offers complete generality in the description of the electron transfer event, coupled to diffusion, through a classical master equation. Using this approach, we examine two-dimensional diffusional systems, where one coordinate acts as an effective solvent reorganization coordinate, and the other is the traditional mass diffusion coordinate. We find that this system can be marginalized to a simple one-dimensional system with modified Marcus rates, so long as the two coordinates are nearly separable. Additionally, we use the framework crafted in this work to show an often ignored limitation of grid-based voltammetry simulation techniques; namely, the dependence of long time transient currents on grid-spacing. Finally, we provide a foundation for how to coarse-grain rate constants for voltammetry simulation, from spatially variant *ab initio* rate constants.

In chapter 4 we extend the formalism of chapter 3 to include nuclear quantum effects, through the addition of a quantized proton coordinate. First, we present a derivation of a combined quantum classical Liouville equation-classical master equation for proton coupled electron transfer, which can be solved with surface hopping dynamics. This equation is roughly analogous to the master equation derived in chapter 3, with the addition of quantized vibronic states leading to additional ET pathways through coupled proton transfer. Our findings here suggest that inclusion of a quantized proton coordinate give rise to quantitatively different voltammetry curves, although these curves can not be uniquely tied to the nature of the concerted proton transfer/electron transfer event. Therefore, our takeaway is that additional diagnostic tools will be necessary to elucidate whether or not an electrochemical electron transfer is proton coupled.

In chapter 5 we develop a grid-free method for carrying out sweep voltammetry simulations. By using a Green's function solution, we can solve for an exact redox species concentration profile, allowing for explicit and exact calculation of any arbitrary, in solution voltammetry sweep experiment. Coupling this approach to an implicit ordinary differential equation solver, we can also incorporate adsorption effects, in a method that appears computationally equivalent or faster than currently employed techniques for handling electrochemical adsorp-

tion in the literature. This method will open up previously computationally inaccessible pathways for studying inner-sphere electron transfer effects in electrochemical voltammetry simulations.

In chapter 6 we present a brief summary of the work outlined in chapters 2 through 5, and discuss future avenues for extending the work herein.

CHAPTER 2

When is Electronic Friction Reliable for Dynamics at a Molecule-Metal Interface?

This chapter is adapted from *PCCP* **20**, 9847 (2018).

2.1. Introduction

Many critical electron transfer (ET) phenomena occur in the nonadiabatic limit, where the Born-Oppenheimer approximation is no longer valid. One such case is that of a molecule near a metal surface[6,7,8,9,10], where an electron can transfer between a molecule and metal at relatively long distances. Such an ET process is at the heart of many electrochemical systems[11,12,13,14], molecular junctions, and even some scattering problems[15,16]. In general, these nonadiabatic dynamics are challenging to model quantitatively because the systems are very large.

In this work, we focus exclusively on the high temperature limit, $\hbar\omega < kT$ (ω being a typical nuclear frequency), so as to allow for a separation of nuclear and electronic motion and a classical treatment of the nuclear degrees of freedom (DoFs). There are today two common approaches for modeling such coupled nuclear-electronic dynamics: surface hopping (SH) and generalized electronic friction with Langevin dynamics (EF-LD). First, according to SH, one propagates dynamics independently on two diabatic surfaces, while the influence of the metal surface acts as a coupling between impurity occupied/unoccupied diabatic states[17]. Second, the EF-LD method entails running effectively adiabatic dynamics along a potential of mean force (PMF), subject to an external friction and random force (that arises from the continuum of electronic states in the bath[18]). Many electronic friction models have been implemented, based on bootstrapping[19], perturbation theory in quasi-classical or reduced coordinates[20,21,22,23], bosonization techniques[24,25], a nonequilibrium Green function approach[26,27,28,29,30], and influence functionals and more generally path integrals[31,32,33].

Recently, our group has demonstrated that all of these results emerge from one universal electronic friction tensor[2,3,4] based on the quantum-classical Liouville equation[34,35] plus projection operators[36,37]. In general, because the SH method is a perturbative treatment in Γ, the hybridization function that describes the elctron-metal coupling, SH should be valid only in the limit where the electron-metal coupling is small compared to kT ($\Gamma < kT$). By contrast, EF-LD is based on a slow velocity approximation and should require fast equilibration, meaning that $\Gamma > \hbar\omega$ (and small electron-phonon couplings). Recent work has shown that there are ways to bridge the gaps between the two methods, i.e. by employing SH trajectories moving along broadened diabatic surfaces[38], or by discretizing the continuum of electronic states and assuming independent single electron states using an independent-electron surfaced hopping (IESH) method[39,40]. For increased accuracy, one can incorporate nuclear quantum effects into a master equation[41,42]. For efficient dynamics, a local density approximation can be used; see the recent studies by Juaristi and Reuter where electronic friction was used to study the relaxation of CO on Cu and N on Ag[43].

Now, despite the formal arguments above, in a previous work Ouyang et al.[5] found a very curious result: EF-LD dynamics unexpectedly agree with SH dynamics in the limit $\Gamma < \hbar\omega$, as long as there is 1) a sufficiently large exit barrier from one diabatic well with a single exit channel, 2) a source of external (nuclear/phononic) friction, and 3) the coupling Γ doesn't depend on position. Under these restrictive conditions, which preclude any important excited state dynamics, Marcus theory is approximately equal to Kramer's theory in the small Γ limit[5]. Our goal in the present article is to further examine the EF-LD approach and assess its performance in the small Γ limit. It is clear that electronic friction cannot agree with surface hopping in the absence of external friction for weak-molecule metal coupling[17], as shown recently for a 2-D scattering model[44], and yet what if we relax the other two conditions? How will EF-LD perform? We will be particularly interested in multidimensional problems where multiple channels are possible, as well as violations of the Condon approximation.

To make progress, our approach will be to construct several generalized Anderson-Holstein model[45,46] problems, with non-Condon effects. The AH model is the simplest model possible for studying an electronic impurity coupled to a bath of phonons and electrons, and is often used to quantify ET near a metal surface. Our generalized AH model will employ two diabatic potential energy surfaces (PESs), where the two PESs correspond to the impurity being either occupied or unoccupied, and will be of the form

$$H = H_s + H_b + H_c \tag{2.1a}$$

$$H_s = E(\mathbf{x})d^\dagger d + V_0(\mathbf{x}) + \sum_{\alpha=1}^{N} \frac{p_\alpha^2}{2m_\alpha} \tag{2.1b}$$

$$H_b = \sum_k (\epsilon_k - \mu) c_k^\dagger c_k \tag{2.1c}$$

$$H_c = \sum_k W_k(\mathbf{x})(c_k^\dagger d + d^\dagger c_k) \tag{2.1d}$$

$$\Gamma(\epsilon, \mathbf{x}) = 2\pi \sum_k |W_k(\mathbf{x})|^2 \delta(\epsilon_k - \epsilon). \tag{2.1e}$$

Here, μ is the chemical potential, W_k is the coupling between the bath and system modes, Γ is the hybridization function, V_0 is the impurity unoccupied diabatic state, E is the difference in energy between unoccupied and occupied states, and $c_k(c_k^\dagger)$, $d(d^\dagger)$ are the annihilation (creation) operators in the bath and system, respectively. We utilize a small molecule-metal coupling ($\Gamma < kT$) where SH must be reliable regardless of non-Condon contributions. In this regime we will be able to benchmark EF-LD dynamics against SH dynamics. In what follows, we will construct three model Hamiltonians with different forms for E, V_0, and Γ. These three Hamiltonians will be designed to tease out how non-Condon effects can influence the final dynamics.

The organization of this paper is as follows. In Sec. II we present the models under investigation and we define the requisite theory and formulae needed to carry out the dynamics being studied. We will then present the results in Sec. III, discuss our results in Sec. IV, and conclude in Sec. V.

2.2. Theory

We begin by introducing three different generalized AH model problems for analyzing dynamics. Thereafter, we will briefly review how to propagate SH and EF-LD trajectories.

2.2.1. Models

Model A, Two Minima in One Dimension

Our first model is inspired by conical intersections in solutions, where the diabatic coupling is zero at the actual crossing point. Thus, we define two diabatic PESs,

$$V_0(x) = \tfrac{1}{2} m\omega^2 x^2 \tag{2.2a}$$

$$V_1(x) = \tfrac{1}{2} m\omega^2 (x-g)^2 + \Delta G^\circ. \tag{2.2b}$$

$V_0(x)$ and $V_1(x)$ are the potentials corresponding to an impurity unoccupied or occupied and ΔG° is the free energy difference between the two states; x is the reaction coordinate. These PESs are plotted in Fig. 2.1(a). The difference in energy as a function of position is

$$E(x) = V_1(x) - V_0(x) = \frac{1}{2} m\omega^2 (g^2 - 2xg) + \Delta G^\circ. \tag{2.3}$$

We work in the wide band approximation, and the density of states weighted metal-molecule coupling between these two diabats is chosen to be

$$\Gamma(x) = \Gamma_1 (\Gamma_0 + \frac{K(x-d)^2}{1 + K(x-d)^2}) \tag{2.4}$$

where $d = \frac{g}{2} + \frac{\Delta G^\circ}{m\omega^2 g}$ is the x value that minimizes $E(x)$, the crossing point of the two diabatic PESs. Note that $\Gamma(x)$ is minimized at $x = d$, see Fig. 2.1(b).

Model B, Two Minima in Two Dimensions

For our second model problem, we introduce another spatial dimension (y) and modify the molecule-metal coupling so as to investigate how the dynamics change when Γ depends on y (rather than the reaction coordinate x). To visualize these potentials and couplings, see Figs. 2.3(a) and 2.3(b). The two diabats for this model are

$$V_0(x,y) = \tfrac{1}{2}m\omega^2(x^2+y^2) \tag{2.5a}$$

$$V_1(x,y) = \tfrac{1}{2}m\omega^2((x-g)^2+y^2) + \Delta G^\circ. \tag{2.5b}$$

The coupling is now chosen to be

$$\Gamma(y) = \Gamma_0 + \Gamma_1 e^{-\alpha(y-\delta)^2} \tag{2.6}$$

which results in a coupling that is approximately Γ_0 far from δ and $\Gamma_1 + \Gamma_0 \approx \Gamma_1$ ($\Gamma_1 \gg \Gamma_0$) at $y = \delta$.

Model C, Three Minima in Two Dimensions

Our final model problem considers a case with three minima located near the following points: the reactant minima is centered near $\mathbf{r_1} = (0,0)$ and the product minima are near $\mathbf{r_2} = (g, y_A)$ or $\mathbf{r_3} = (g, -y_A)$. With three minima, one can now analyze the relative probabilities of $\mathbf{r_1} \to \mathbf{r_2}$ and $\mathbf{r_1} \to \mathbf{r_3}$. The reactant (unoccupied) diabat is chosen to be the same as V_0 from Eqn. 2.5(a), while the product (occupied) diabat V_1 is as follows:

$$\begin{aligned} V_1(x,y) = \frac{1}{2}m(\omega^2(x-g)^2 + \omega_y^2(y^2+y_A^2)) + \frac{\Delta G_L^\circ + \Delta G_R^\circ}{2} \\ - \sqrt{(m\omega_y^2 y y_A + \frac{\Delta G_L^\circ - \Delta G_R^\circ}{2})^2 + \epsilon^2}. \end{aligned} \tag{2.7}$$

Obviously, the product holds two minima that are centered at the same position in the x-direction (at $x = g$) but with two possibilities in the y direction (roughly $y = \pm y_a$). ϵ is

a small parameter chosen as 10^{-6} to ensure that the diabatic potential is smooth. ΔG_L° is roughly the energy difference between the minima of V_0 and the minima located at $-y_A$, while ΔG_R° is roughly the energy difference between the minima of V_0 and the minima located at y_A. The coupling in this model is expressed as a logistic function,

$$\Gamma(y) = \Gamma_0 + \frac{\Gamma_1 - \Gamma_0}{1 + e^{-\kappa(y-\eta)}} \tag{2.8}$$

where $\Gamma_1 \gg \Gamma_0$ and we chose $\eta = 1$ which ensures the coupling is $\approx \Gamma_1$ near the minima centered at $+y_A$, whereas the coupling is $\approx \Gamma_0$ at the minima centered at $-y_A$. To visualize these potentials and couplings, see Figs. 2.4(a) and 2.4(b). This model provides a mechanism to study dynamics in the case where the reaction and coupling coordinates are mixed, as well as when multiple exit channels are present.

2.2.2. Dynamics

We now review the relevant dynamics protocols.

Surface Hopping

There are two necessary prerequisites when performing SH dynamics, the small coupling limit ($\Gamma < \hbar\omega$) and the high temperature limit ($\hbar\omega < kT$). The basic premise of SH is that one runs dynamics along individual diabatic surfaces with hops between surfaces. We define the phase space probability densities for the nuclear DoFs as $P_0(\mathbf{x}, \mathbf{p}, t)$ and $P_1(\mathbf{x}, \mathbf{p}, t)$ at time t, where $P_0(P_1)$ is the probability density for the electronic impurity to be unoccupied (occupied), assuming the nuclei is at position $\mathbf{x}$ with momentum $\mathbf{p}$. The time evolution of

these probability densities is given by the following equations

$$\begin{aligned}\frac{\partial P_0(\mathbf{x},\mathbf{p},t)}{\partial t} &= \nabla_x V_0(\mathbf{x},\mathbf{p})\cdot\nabla_p P_0(\mathbf{x},\mathbf{p},t) \\ &\quad - \frac{p}{m}\nabla_x P_0(\mathbf{x},\mathbf{p},t) \\ &\quad - \gamma_{0\to1}P_0(\mathbf{x},\mathbf{p},t) + \gamma_{1\to0}P_1(\mathbf{x},\mathbf{p},t)\end{aligned} \tag{2.9a}$$

$$\begin{aligned}\frac{\partial P_1(\mathbf{x},\mathbf{p},t)}{\partial t} &= \nabla_x V_1(\mathbf{x},\mathbf{p})\cdot\nabla_p P_1(\mathbf{x},\mathbf{p},t) \\ &\quad - \frac{p}{m}\nabla_x P_1(\mathbf{x},\mathbf{p},t) \\ &\quad + \gamma_{0\to1}P_0(\mathbf{x},\mathbf{p},t) - \gamma_{1\to0}P_1(\mathbf{x},\mathbf{p},t)\end{aligned} \tag{2.9b}$$

where $\gamma_{0\to1}$ ($\gamma_{1\to0}$) is the hopping rate from surface 0 to 1 (1 to 0)

$$\gamma_{0\to1} = \tfrac{\Gamma(\mathbf{x})}{\hbar} f(E(\mathbf{x})) \tag{2.10a}$$

$$\gamma_{1\to0} = \tfrac{\Gamma(\mathbf{x})}{\hbar}(1 - f(E(\mathbf{x}))) \tag{2.10b}$$

and $f(E(\mathbf{x}))$ is the fermi function, $f(E(\mathbf{x})) = \frac{1}{1+e^{\beta(E(\mathbf{x}))}}$, $\beta = (k_B T)^{-1}$. These SH dynamics are very different from Tully's energy conserving fewest switches surface hopping method; in the present case, the system is open with respect to energy flow between the system and bath and therefore energy conservation is not imposed with each hop.

Electronic Friction

We first define some mathematical identities that are needed for the presentation of EF-LD. For a general problem on a metal surface with multiple nuclear degrees of freedom, the relevant EF-LD dynamics take the form[47]:

$$-m_\alpha \ddot{x}_\alpha = -F_\alpha + \sum_\beta \gamma_{\alpha\beta}\dot{x}_\beta + \delta f_\alpha(t). \tag{2.11}$$

Here α is an index for a nuclear DoF and F_α is the mean force

$$F_\alpha = -(\frac{\partial V_0}{\partial x_\alpha} + \int_{-\Lambda}^{\Lambda} \frac{d\epsilon}{2\pi}(\frac{\partial E}{\partial x_\alpha} + \frac{(\epsilon - E)}{\Gamma}\frac{\partial \Gamma}{\partial x_\alpha})A(\epsilon, \mathbf{x})f(\epsilon)). \tag{2.12}$$

$\gamma_{\alpha\beta}$ is the $\alpha\beta$ element of the electronic friction tensor

$$\begin{aligned}\gamma_{\alpha\beta} = \frac{\hbar}{2}\int \frac{d\epsilon}{2\pi}(\frac{\partial E}{\partial x_\alpha} + \frac{(\epsilon - E)}{\Gamma}\frac{\partial \Gamma}{\partial x_\alpha}) \\ \times (\frac{\partial E}{\partial x_\beta} + \frac{(\epsilon - E)}{\Gamma}\frac{\partial \Gamma}{\partial x_\beta})A(\epsilon, \mathbf{x})^2\frac{f(\epsilon)(1 - f(\epsilon))}{kT}\end{aligned} \tag{2.13}$$

and $\delta f_\alpha(t)$ is the random force with associated correlation function $D_{\alpha\beta}\delta(t - t') = \langle \delta f_\alpha(t)\delta f_\beta(t')\rangle$,

$$\begin{aligned}D_{\alpha\beta} = \hbar\int \frac{d\epsilon}{2\pi}(\frac{\partial E}{\partial x_\alpha} + \frac{(\epsilon - E)}{\Gamma}\frac{\partial \Gamma}{\partial x_\alpha}) \\ \times (\frac{\partial E}{\partial x_\beta} + \frac{(\epsilon - E)}{\Gamma}\frac{\partial \Gamma}{\partial x_\beta})A(\epsilon, \mathbf{x})^2 f(\epsilon)(1 - f(\epsilon)).\end{aligned} \tag{2.14}$$

In the above equations $A(\epsilon, \mathbf{x})$ is the spectral function,

$$A(\epsilon, \mathbf{x}) = \frac{\Gamma(\mathbf{x})}{(\epsilon - E(\mathbf{x}))^2 + (\frac{\Gamma(\mathbf{x})}{2})^2} \tag{2.15}$$

and Λ is the electronic bandwidth, which is chosen such that $\Lambda \gg \Gamma$. When the Condon approximation holds ($\frac{\partial \Gamma}{\partial x_\alpha} = 0$) the above equations simplify considerably. The PMF is given by

$$V_{PMF}(\mathbf{x}) = -\int_{\mathbf{x_0}}^{\mathbf{x}} F(\mathbf{x}') \cdot d\mathbf{x}' \tag{2.16}$$

where F is given in Eqn. 2.12. For graphical purposes, V_{PMF} can be evaluated numerically on a grid.

2.2.3. Simulation Details

Below, we wish to study dynamics in the presence of a thermal environment. Thus, we will include an additional non-electronic source of friction, γ_n. Trajectories for each model

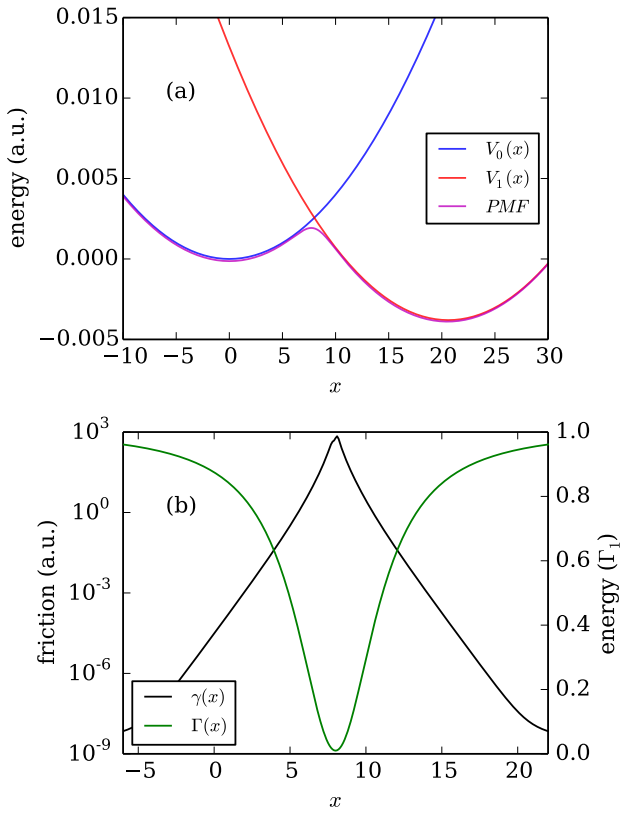

Figure 2.1: (a) Diabatic potentials (Eqn. 2.2) and PMF (Eqn. 2.16) for model A. The crossing point is located at $x = 8$ (b) $\Gamma(x)$ and $\gamma(x)$ as a function of position ($\Gamma(x)$ is in units of Γ_1), $\Gamma_0 = 0.01$, $K = 0.1$.

are initialized on diabat V_0 with a Boltzmann distribution of position and velocity. Rates for SH were obtained by fitting the impurity population as a function of time with an exponential, while rates for EF-LD were found by fitting the position as a function of time to an exponential. Unless stated otherwise, 200 trajectories were run for both SH and EF-LD simulations, and all simulations were performed with $\Gamma_1 = 0.0001$, $m = 2000$, $\omega = 0.0002$, $g = 20.6097$, $\Delta G^\circ = -0.0038$, $\gamma_n = 2m\omega = 0.4$, $\Lambda = 0.1$, and $kT = 0.00095$. All parameters are in atomic units.

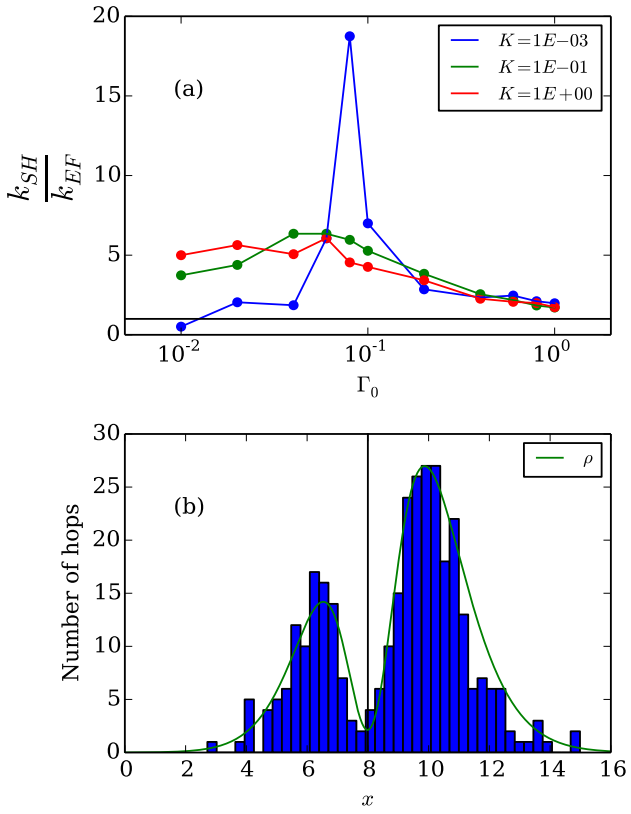

Figure 2.2: Results from model A. (a) Ratio of rates of ET from SH and EF-LD for multiple combinations of parameters K and Γ_0. SH and EF-LD rates agree in the limit of large Γ_0, since the positional dependence weakens as Γ_0 increases. (b) Histogram of positions where hops occur for the parameters in Fig. 2.1(b). The green trace, ρ, is a rescaled distribution capturing the probability of being at a given position multiplied by the hopping probability from diabat 0 to diabat 1: $\rho(x) = Ne^{-\beta V_0(x)} * \Gamma(x) * f(E(x))$. In general, EF-LD appears to disagree with SH when the hopping probability is bimodal.

2.3. Results

2.3.1. Model A

In Fig. 2.1(b) we plot $\Gamma(x)$, $\gamma_e(x)$ for model A. Note that the friction increases dramatically near the crossing point, $x = d$, which should significantly reduce the rate of barrier crossings according to EF-LD. Fig. 2.2(a) shows the ratio of rates obtained from SH versus EF-LD, $\frac{k_{SH}}{k_{EF}}$, for a wide set of parameters for model A. Under a broad set of $\Gamma(x)$ parameterizations, EF-LD underestimates the rate by as much as an order of magnitude compared to SH. One might suppose that the rates from SH are higher due to the ability for hops to occur at positions far from the crossing point, where $\Gamma(x)$ is at a minimum, whereas all EF-LD trajectories must pass through the crossing point region where the friction is very large. To test this, we looked at the positions where hops from diabat 0 to diabat 1 were most likely to occur. Fig. 2.2(b) shows a histogram of such positions, for the case $\Gamma_0 = 0.01, K = 0.1$ where the EF-LD and SH rates are very different. Note that, as expected, the hops occur far from the crossing point, $x = d$, and form a bimodal distribution. Indeed, by investigation one concludes that EF-LD and SH disagree more as the hopping distribution becomes more bimodal.[48]

2.3.2. Model B

Having analyzed how reactions proceed when the Condon approximation is violated along a reaction coordinate, we now address how reactions proceed when the Condon approximation is violated in an orthogonal coordinate (*i.e.* the reaction coordinate is x but Γ depends on y). The PMF for Model B is shown in Fig. 2.3(a). While the PMF is not drastically affected by the y dependence of $\Gamma(y)$, the main dynamical effects can be seen in the friction. Fig. 2.3(b) shows the "effective" force on a particle in the negative x-direction, assuming the velocity in both coordinates is equal to the root-mean square velocity, chosen so as to illustrate the force under a typical velocity. Unlike the one-dimensional case, EF-LD allows for barrier

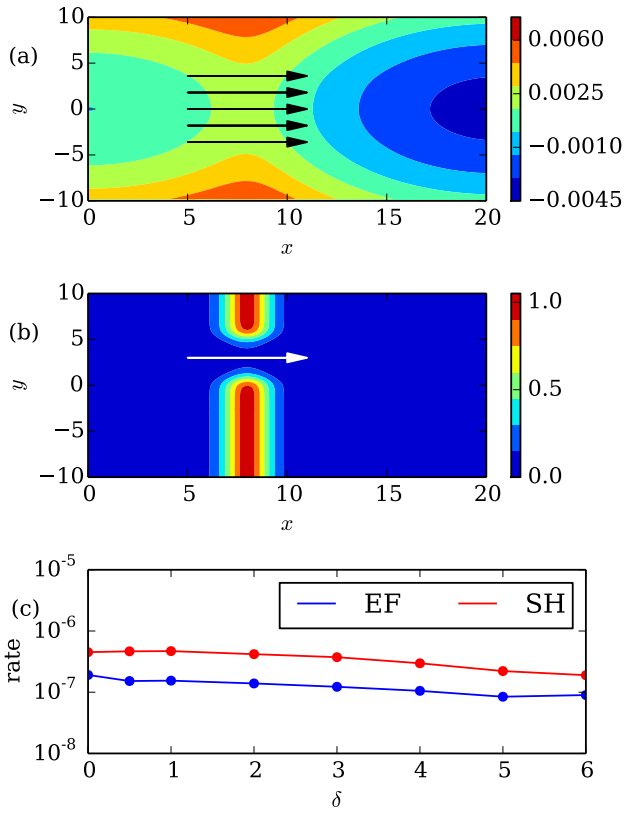

Figure 2.3: (a) PMF for model B. Parameter values are $\Gamma_0 = 1e-5$, $\alpha = 0.5$, $\delta = 3$. The black arrows indicate the overall reaction coordinate. (b) Normalized effective force on a particle in the negative x-direction for the parameterization in (a), assuming a velocity $v_x = v_y = v_{rms} = \sqrt{\frac{3kT}{m}}$. See Eqns. 2.11-2.13; here we plot $\frac{\partial V_0}{\partial x} - F_x + \gamma_{xx}v_x + \gamma_{xy}v_y$. While the PMF predicts equally likely crossings over a wide set of y values, the frictional effects shown in (b) suggest that there is only a narrow channel through which trajectories can pass from the left minima to the right minima. (c) Rates for SH and EF-LD for the same model as Fig. 2.3(a), as a function of δ. Note the success of the EF-LD approach in effectively recovering the correct SH rate.

crossing in the direction of the reaction coordinate through a narrow channel where Γ is maximized and the friction is minimized.

In Fig. 2.3(c) we plot the rates for SH and EF-LD as a function of δ. Although EF-LD slightly underestimates the rate compared to SH, the agreement between the two is obviously much, much closer than that from model A (see Fig. 2.2(a)). We tentatively conclude that, for this two-dimensional problem, similar to what was found in Ref. 5 for a one-dimensional problem, EF-LD agrees with SH dynamics when the problem is effectively one dimensional and the trajectories proceed through an area where the velocities are thermally equilibrated.

2.3.3. Model C

One final example investigates the case where multiple reaction channels exist and the coupling and reaction coordinate are mixed. Fig. 2.4(b) shows the PMF for model C, while Fig. 2.4(c) shows the "effective" force on a particle in the positive y-direction, assuming a positive x velocity and negative y velocity with magnitude equal to the root-mean square velocity. One expects that the minima centered near $+y_A$ will be favored when $\Delta G^\circ_R = \Delta G^\circ_L$, since the coupling $\Gamma(y)$ is higher for $y > 0$. However, as the energy difference is increased by lowering ΔG°_L, we expect to see more trajectories equilibrate in the minima centered at $-y_A$. To test this, we change the value of ΔG°_L and monitor what fraction of trajectories finish in each minima for both SH and EF-LD.

Fig. 2.5(a) shows the ratio of trajectories in each of the two product wells at long times as a function of ΔG°_L. We find that, as the energy bias grows, EF-LD does not recover the correct statistics at long times. Presumably, this failure of EF-LD is caused by the kinetic barrier introduced by the low coupling/high friction separating the two minima (see Fig. 2.4(c)). This barrier will result in EF-LD subsequently underestimating the correct ET rate, as shown in Fig. 2.5(b).

In Figs. 2.5(c) and 2.5(d) we address the question of non-Condon effects and study the equilibrium population and trajectory data when Γ is kept constant, equal to Γ_1. In this

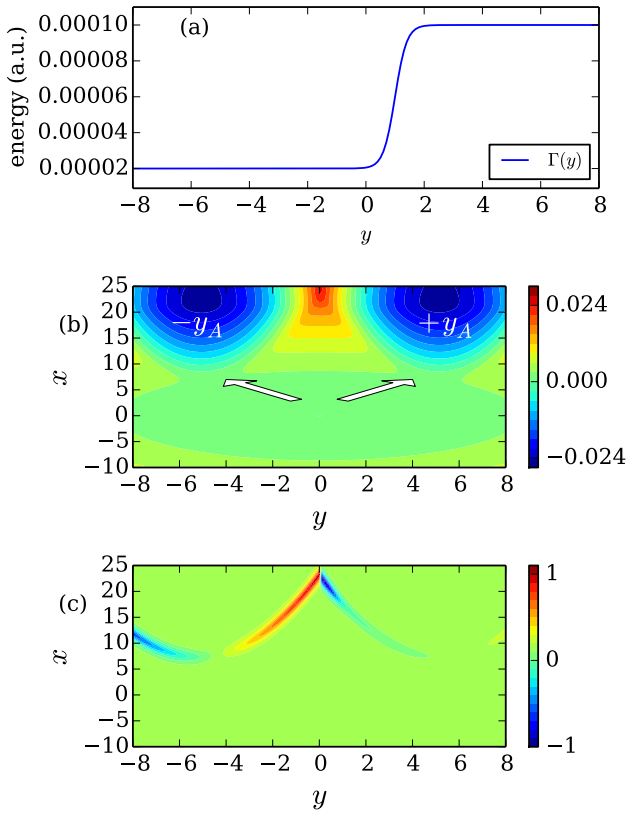

Figure 2.4: (a) $\Gamma(y)$ for model C; the metal-molecule coupling is stronger for the right minima versus the left minima. (b) PMF for model C, $\omega_y = 5\omega = 0.001$, $\Delta G_R^\circ = \Delta G_L^\circ = -0.0038$, $y_A = 5$, $\Gamma_0 = 2e - 5$, $\kappa = 5$, $\eta = 0$. The arrows show the two possible reactive pathways to the product minima at $-y_A$ or $+y_A$. For $\Delta G_L^\circ = \Delta G_R^\circ$, because of $\Gamma(y)$, we expect more trajectories to propagate towards the $+y_A$ well rather than the $-y_A$ well. (c) Normalized effective force on a particle in the negative x-direction for the parameterization in (a), assuming a velocity $-v_y = v_x = v_{rms} = \sqrt{\frac{3kT}{m}}$. See Eqns. 2.11-2.13: here we plot $\frac{\partial V_0}{\partial x} - F_x + \gamma_{xx} v_x + \gamma_{xy} v_y$. Note the frictional barrier between the two minima in (c), as well as a frictional preference for trajectories to move towards the $+y_A$ well rather than the $-y_A$ well.

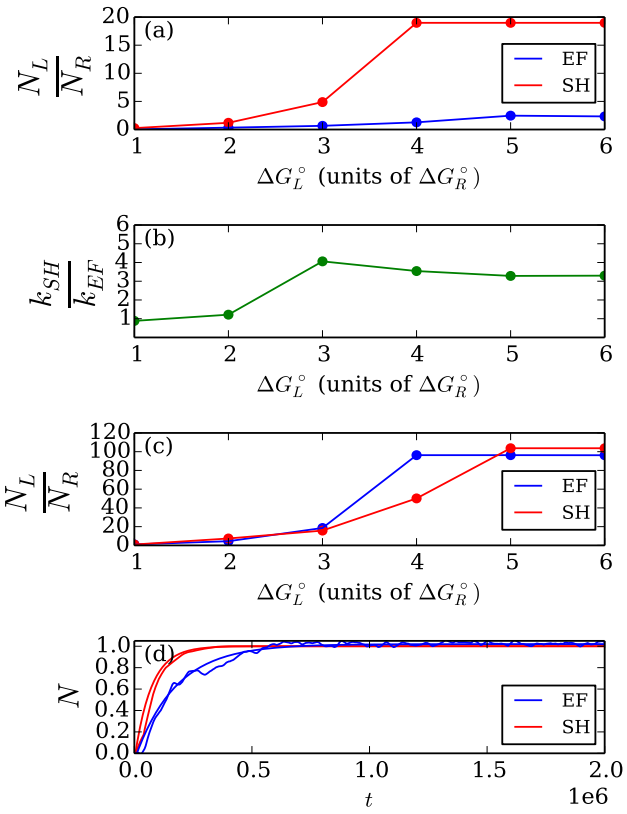

Figure 2.5: Results for model C. (a) Ratio of number of trajectories in left minima versus right minima for SH and EF-LD ($\omega_y = 5\omega = 0.001$, $\Delta G_R^\circ = -0.0038$, $y_A = 5$, $\Gamma_0 = 2e - 5$, $\kappa = 5$) with ΔG_L° varying (ΔG_L° in units of ΔG_R°). Note that EF-LD fails for large ΔG_L°. (b) Ratio of overall rates for reactant going to product (either product basin) for SH and EF-LD for the model in Fig. 2.5(a), with ΔG_L° varying (ΔG_R° in units of ΔG_R°). (c) Ratio of number of trajectories in left minima versus right minima for SH and EF-LD with parameters from (a), except with constant $\Gamma(y) = \Gamma_1$. Note that EF-LD performs quite well for cases when the Condon approximation is not violated. (d) Time data for determining and fitting the overall rate for SH and EF-LD for $\Delta G_L^\circ = 6\Delta G_R^\circ$ for the model in Fig. 2.5(a), except with constant $\Gamma(y) = \Gamma_1$. Again, EF-LD performs well.

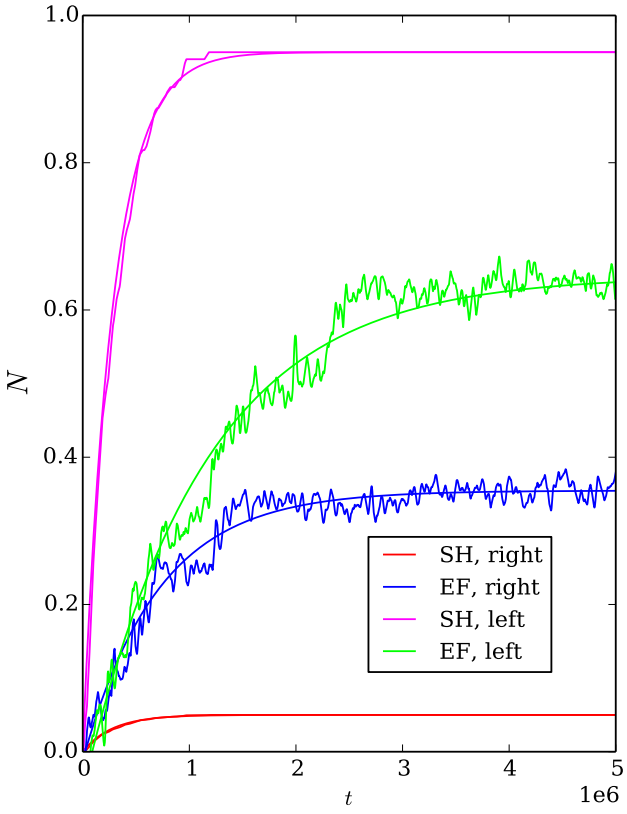

Figure 2.6: The fraction of trajectories in each product basin as a function of time and fits according to SH and EF-LD for $\Delta G^\circ_L = 6\Delta G^\circ_R$ for model C. All other parameters are the same as in Fig. 2.5. Note that both the rate and the equilibrium population in each minima are vastly different, demonstrating that EF-LD fails in this case.

case, EF-LD yields much more similar rates and equilibrium populations compared to SH: thus, the existence of non-Condon effects strongly strains the ability of EF-LD dynamics to recover the correct relative rates of transfer. After all, when the metal-molecule coupling changes significantly, the electronic friction can change dramatically as well. However, within the Condon approximation, EF-LD can treat the competition between two pathways far better apparently.

Finally, Fig. 2.6 plots the population in the product basins as a function of time for $\Delta G_L^\circ = 6\Delta G_R^\circ$ for the parameters in Figs. 2.5(a) and (b) (i.e. with Γ depending on y). Both the rates and final populations in each minima differ greatly between the two methods, suggesting that EF-LD is not suitable for these dynamics.

2.4. Discussion

In this paper we have worked in the limit of weak molecule-metal and we have used three different models to assess when EF-LD is a valid description of dynamics. We have found that the validity of EF-LD seems directly tied to the separability of the reaction coordinate and the nuclear direction that breaks the Condon approximation. If the reaction pathway and coupling coordinate are identical, as in Model A, then EF-LD will not recover the correct dynamics, as evinced by the large disagreement in rates between SH and EF-LD for a wide set of model parameterizations (see Fig. 2.2(a)). This disagreement is empirically tied to the presence of a bimodal hopping distribution. For model B, however, where the coupling and reaction coordinates are not entangled, Fig. 2.3(a) shows good agreement between rates of ET for SH and EF-LD, revealing that EF-LD can succeed as long as equilibration is fast with respect to the reaction coordinate. Finally, if we mix the reaction and coupling coordinates, as illustrated by Model C, Figs. 2.5 and 2.6 show that EF-LD again fails to recover the correct rate and populations. In this case, again, there are two reactive pathways that compete for trajectories, and EF-LD clearly fails if one cannot rely on the Condon approximation

Now, let us reconsider the theoretical argument in Ref. 5. In that paper, using transition

state theory, the authors showed that an adiabatic EF-LD reaction rate was consistent with Marcus's nonadiabatic rate theory if we assumed a single reactive coordinate, equilibrated velocities, and constant Γ. This equivalence was shown using Kramer's theory for an adiabatic EF-LD reaction rate in the limit of large friction. With this fact in mind, we would like to revisit the original proof in Ref. 5 in the context of a multidimensional Hamiltonian. As in Ref. 5 we work exclusively in the high friction (overdamped) limit, and in order to make a simple analytical argument, we will also work in the limit of near separability between reaction and bath coordinates.

With these assumptions in mind, we begin with the multidimensional Smoluchowski equation,

$$\frac{\partial P(\mathbf{x},t)}{\partial t} = \nabla \cdot \mathbf{D}(\mathbf{x}) \cdot [\nabla + \beta \nabla U(\mathbf{x})] P(\mathbf{x},t) \tag{2.17}$$

where $P(\mathbf{x},t)$ is the probability density, $\mathbf{D}(\mathbf{x})$ is the multidimensional diffusion tensor, and $U(\mathbf{x})$ is the potential, which corresponds to a reactive flux

$$\mathbf{J}(\mathbf{x},t) = -\mathbf{D}(\mathbf{x}) \cdot [\nabla + \beta \nabla U(\mathbf{x})] P(\mathbf{x},t). \tag{2.18}$$

Since we desire a steady-state solution for $P(\mathbf{x},t) = P_{ss}(\mathbf{x})$, with vanishing probability as $|\mathbf{x}| \to \infty$, we assume the following functional form for the steady-state probability:

$$P_{ss}(\mathbf{x}) = f(\mathbf{x}) e^{-\beta U(\mathbf{x})}. \tag{2.19}$$

Taking the gradient of both sides and substituting $\nabla P_{ss}(\mathbf{x})$ into equation 2.18 yields

$$\mathbf{J}(\mathbf{x}) = -\mathbf{D}(\mathbf{x}) \cdot [\nabla f e^{-\beta U(\mathbf{x})}]. \tag{2.20}$$

At this point, we assume that the diffusion tensor is invertible, such that

$$\nabla f = -\mathbf{D}(\mathbf{x})^{-1} \cdot \mathbf{J}(\mathbf{x}) e^{\beta U(\mathbf{x})}. \tag{2.21}$$

We now further assume that $\{\mathbf{x}\} = \{\mathbf{Q}\} + \{\mathbf{s}\}$, where $\{\mathbf{s}\}$ is the reaction coordinate and $\{\mathbf{Q}\}$ are the remaining bath coordinates. Because the reaction rate is determined by motion along s, which may depend on Q (though only weakly in the limit of near separability), we integrate both sides over a path s' (which may depend on Q),

$$f(\mathbf{s}, \mathbf{Q}) = -\int_{\infty}^{s} d\mathbf{s}' \cdot \mathbf{D}(\mathbf{s}', \mathbf{Q})^{-1} \cdot \mathbf{J}(\mathbf{s}', \mathbf{Q}) e^{\beta U(\mathbf{s}', \mathbf{Q})}. \tag{2.22}$$

Finally, at steady state where J is a constant, given our assumption of near separability between reaction and bath coordinates, we expect $\mathbf{J}(\mathbf{s}, \mathbf{Q}) = \mathbf{J}(\mathbf{Q}) = |J(\mathbf{Q})|\hat{s}$ and thus:

$$f(\mathbf{s}, \mathbf{Q}) = |J(\mathbf{Q})| \int_{s}^{\infty} ds' (\hat{s}' \cdot \mathbf{D}(\mathbf{s}', \mathbf{Q})^{-1} \cdot \hat{s}') e^{\beta U(\mathbf{s}', \mathbf{Q})}. \tag{2.23}$$

Now, to find the rate, we evaluate the flux divided by the population for every bath coordinate,

$$\begin{aligned} k(\mathbf{Q}) &= \frac{|J(\mathbf{Q})|}{\int_{-\infty}^{s_B} ds P_{ss}(\mathbf{s}, \mathbf{Q})} \\ k(\mathbf{Q}) &= \left[\int_{-\infty}^{s_B} ds \; e^{-\beta U(\mathbf{s}, \mathbf{Q})} \int_{s}^{\infty} ds' \; \beta \gamma_e^{s's'} e^{\beta U(\mathbf{s}', \mathbf{Q})} \right]^{-1} \end{aligned} \tag{2.24}$$

where we have used the relationship $\gamma_e \cdot \mathbf{D} = \mathbf{D} \cdot \gamma_e = \beta^{-1} \mathbb{1}$ to replace the element of the diffusion tensor with the corresponding element of the friction tensor. Obviously, $k(\mathbf{Q})$ is a simple 1D rate constant analagous to the rate in Ref. 5:

$$k^{1D} = \left[\int_{-\infty}^{s_B} ds \; e^{-\beta U(s)} \int_{s}^{\infty} ds' \; \beta \gamma_e e^{\beta U(s')} \right]^{-1}. \tag{2.25}$$

And, as shown in Ref. 5, this expression is equivalent to the following expression in the limit of small Γ (where γ_e is effectively a delta function), which is also equivalent to Marcus theory:

$$k^{1D} \approx \frac{1}{Z_0} \frac{\Gamma}{\beta \hbar} \left| \frac{dE(s)}{ds} \Big|_{s=s_B} \right|^{-1} e^{-\beta U(s_B)}. \tag{2.26}$$

Thus, in the end we have shown that a multidimensional problem with electronic friction can still be reduced to Marcus theory. However, a few conditions must be met. First, the potential $U(\mathbf{s},\mathbf{Q})$ must be separable in the reaction and bath coordinates, $U(\mathbf{s},\mathbf{Q}) = U(\mathbf{s}) + U(\mathbf{Q})$, and the difference in energy $E = U_1 - U_0$ must be independent of Q. Second, $\gamma_e^{s's'}$ must equal $\frac{\beta\hbar}{\Gamma} f(E(\mathbf{s},\mathbf{Q}))(1 - f(E(\mathbf{s},\mathbf{Q})))(\frac{dE}{ds})^2$, which only occurs when Γ is constant with respect to the reaction coordinate s. In other words, given our assumption of near separability, one can break the Condon approximation, but only in the Q-direction, not the s-direction, (i.e. $\frac{\partial\Gamma}{\partial s}$ must be zero, but $\frac{\partial\Gamma}{\partial Q}$ can be nonzero). Overall, this heuristic argument provides a mathematical justification for the results we have found above for models A, B, and C. For model B, where the conditions above hold, we find that EF-LD recovers SH results. This equivalence does not hold for model A or model C, where the reaction coordinate and the coordinate over which Γ varies are either identical or mixed, respectively.

2.5. Conclusions

In the end, whereas Ref. 5 demonstrated analytically that EF-LD will fail if there are excited state dynamics, the present results suggest something more general: EF-LD may fail if there are two different, non-equivalent pathways — along the ground or excited states — consistent with different hopping locations in phase space and different metal-molecule couplings. In other words, we have found that (i) separability of the reaction and bath coordinates and (ii) the validity of the Condon approximation in the reaction coordinate are not only sufficient but also necessary if one wishes to safely invoke EF-LD trajectories. Furthermore, we remind the reader that transition state theory does not have any validity without external friction and equilibrated velocities, and thus EF-LD cannot agree with SH without any external friction for weak molecule-metal coupling[5,17]. Thus, in the end, the promising analytic transition state theory result in Ref. 5 that allowed Kramer's theory to recover the Marcus theory result in the nonadiabatic limit would appear to be a very limited success story.

Looking forward, the most natural next step is to begin investigating both ab initio and model problems with increasing numbers of nuclear coordinates, where we may test the electronic friction approach in a truly condensed phase environment. In particular, we would like to apply EF-LD trajectories to the case of electron transfer at metal surfaces but, as a practical matter, we must first ascertain how the metal-molecule coupling changes for realistic problems and learn when multiple pathways are possible (which is likely the case for radical chemistry). Many exciting questions remain regarding the intersection of electronic structure theory and nonadiabatic dynamics at metal surfaces.

CHAPTER 3

Modeling Electron Transfer in Diffusive Multidimensional Electrochemical Systems

This chapter is adapted from Ref. 49.

3.1. Introduction

Within the field of electrochemistry, one of the open questions is: what is the simplest computational model for capturing the details of Tafel plots and cyclic voltammograms for realistic experiments? Historically, when modeling such electron transfer (ET) events at the electrode surface, the usual approach has been to enforce either static or local empirical boundary conditions, especially Nernstian equilibrium or Butler-Volmer kinetics[50]. These boundary conditions are simple to implement and applicable in many common applications, even in the presence of diffuse charges on surfaces[51]. Nevertheless, the above approaches do not address the actual mechanism of a complicated ET event[52]; for instance, the Butler-Volmer approach hides a great deal of physics (all barrier heights and shapes, reorganization free energies, solvent recrossing probabilities) in one empirical parameter, namely the transfer coefficient.

Many efforts to improve upon the canonical techniques of electrochemistry have been constructed, most commonly using Marcus-Hush (MH) theory which usually assumes symmetric parabolas[53,54]. However, there has also been some development for asymmetric parabolas[55] and non-parabolic surfaces (where local low-frequency vibrations can alter the effective force constant of the two oxidative states differently[56]). More generally, one can estimate rate constants for electron transfer using Fermi's golden rule and evaluating a one-dimensional integral (sometimes called a Marcus-Hush-Chidsey integral[57,58]). And quite often, by fitting experimental I-V curves to Fermi's golden rule (FGR) rates, one can extract reasonable thermodynamic parameters, e.g. reorganization energies[59]. However, even this approach is

not without limitations[60], and FGR integrals have been shown to be insufficient for replicating some voltammetry experiments quantitatively[55]; in fact, sometimes more involved FGR treatments of I-V curves perform worse than the simpler Butler-Volmer equations[61]. Current electrochemical research is exploring alternatives to Bulter-Volmer, including phase-field models[62], density functional theory (DFT) aided molecular dynamics simulations[63,64], and other approaches.

In the end, the potential energy surfaces as relevant to electrochemistry are large and quite complicated, and the statistical mechanics of sampling such configurations is daunting. As far as we are aware, there is still no complete and practical methodology for simulating electrochemical phenomena that (i) can describe complex chemical transformations (including multi-electron transfer events) using (ii) only a few parameters (ideally extracted from electronic structure theory). We also note that modern simulations using the Nernstian and Butler-Volmer boundary conditions should be valid only when electron transfer at the surface is relatively fast and largely decoupled from other surface processes. Unlike these approaches, the ideal electrochemical simulation (iii) should be applicable whether electron transfer, mass diffusion, or some other transformation is rate limiting. From our point of view, even though there is also a long history of studying ET coupled to diffusion in solution[65,66,67,68], as well as photoinduced ET and ion recombination in different enviornments[69,70,71], there has still been very little development of the theory of electrochemical dynamics compared to the vast theoretical developments in photochemistry and photodynamics. This gap between photochemistry and electrochemistry poses both a challenge and opportunity for chemical theory. Recently, there has has been recognition of the importance of modeling electrochemical ET through a more complete Marcus picture[72], but previous works in this vein have usually assumed restrictive conditions, for example, focusing primarily on *equilibrium* statistical fluctuations[73]. Thus far, little attention has been given to methods that explicitly model the *dynamics* of electrochemical ET with molecular motion *in bulk and at the surface.*

In this paper we analyze the simplest such multidimensional approach for simulating electrochemical dynamics: we study electron transfer with molecular motion possible along two different nuclear coordinates, one a solvent reorganization coordinate and the other a diffusion coordinate, under an applied potential. By modeling ET with a stochastic, nonadiabatic surface hopping[1] (SH) ansatz, we will build new intuition for how to understand I-V curves dynamically. An outline of this paper is as follows. In Sec. II we compare the standard approaches for electrochemical simulations, highlighting how these different approaches relate to one another. In Sec. III we present results for each approach, comparing and contrasting when a two-dimensional simulation can be reduced to a more simpler one-dimensional case. Finally, in Sec. IV, we discuss how to connect mass transport models with ab initio models of electrochemical dynamics and we point out the obvious improvements needed in order to make progress. We conclude in Sec. V.

3.2. Methods

3.2.1. Basic electrochemical methods in one dimension

As is standard, we begin our discussion with an analysis of electrochemical dynamics in one dimension, where mass transport and diffusion are paramount.

Mass transport with Butler-Volmer and Nernstian boundary conditions

Historically, simulation of electrochemical systems has been carried out by modeling solute mass transport and incorporating electrode boundary conditions that obey either Nernstian or Butler-Volmer boundary conditions. For the most part, this approach requires only a simple grid in one-dimension (to simulate diffusive motion of the electroactive species in solution) and the implementation of species exchange at the surface (to simulate charge transfer).

To illustrate this approach, consider the following equation:

$$\mathrm{A} + \mathrm{e}^- \underset{\mathrm{k_b}}{\overset{\mathrm{k_f}}{\rightleftharpoons}} \mathrm{B}$$

Here, species A is reduced at the electrode to form B, and the reaction is reversible. The kinetics obey

$$\begin{aligned} \vec{J_A} &= -D_A^x \frac{\partial c_A}{\partial x}\hat{x} \\ \vec{J_B} &= -D_B^x \frac{\partial c_B}{\partial x}\hat{x} \end{aligned} \tag{3.1a}$$

$$\begin{aligned} \frac{\partial c_A}{\partial t} &= -\vec{\nabla}\cdot\vec{J_A} = D_A^x \frac{\partial^2 c_A}{\partial x^2} \\ \frac{\partial c_B}{\partial t} &= -\vec{\nabla}\cdot\vec{J_B} = D_B^x \frac{\partial^2 c_B}{\partial x^2}, \end{aligned} \tag{3.1b}$$

where $\hat{x}$ is the unit vector for the diffusive coordinate, J_A (J_B) is the current of species A (B) and D_A^x (D_B^x) is the diffusion coefficient in the x direction (which we take as equal for both species A and B). Equation 3.1 is an almost complete protocol for simulating electrochemical systems, but does require boundary conditions. The system is governed by the following initial conditions,

$$c_A(t=0,x) = c_A^{bulk} = 1 \tag{3.2a}$$

$$c_B(t=0,x) = c_B^{bulk} = 0 \tag{3.2b}$$

and bath boundary conditions

$$c_A(t,x=\infty) = c_A^{bulk} = 1 \tag{3.3a}$$

$$c_B(t,x=\infty) = c_B^{bulk} = 0 \tag{3.3b}$$

The initial conditions above state that only A is present at time zero and the boundary conditions are defined so that the concentrations of A and B are equal to their bulk concentrations infinitely far from the electrode. What remains to be determined, however, are the dynamical boundary conditions at the electrode surface, where two options are standard.

Nernstian: On the one hand, Nernstian boundary conditions enforce the proper equilibrium ratio for the surface concentration of species A divided by the surface concentration of species B at all times. We assume the surface concentrations at the boundary are related to the ratio of the forward and backward rate constants, k_f and k_b[50,74]:

$$\frac{c_B}{c_A}|_{x=0} = \frac{k_f}{k_b} = e^{-\beta(\Delta G(t) - \Delta G^\circ)}. \tag{3.4}$$

Butler-Volmer: On the other hand, Butler-Volmer boundary conditions stipulate that the concentration gradient at the electrode surface must be equal to the net flux:

$$D_A^x \frac{\partial c_A}{\partial x}|_{x=0} = k_f c_A|_{x=0} - k_b c_B|_{x=0}, \tag{3.5}$$

The forward and backward rates are given by

$$k_f = k^\circ e^{-\alpha\beta(\Delta G(t) - \Delta G^\circ)} \tag{3.6a}$$

$$k_b = k^\circ e^{(1-\alpha)\beta(\Delta G(t) - \Delta G^\circ)} \tag{3.6b}$$

where k° is the standard rate constant, α is the transfer coefficient, $\beta = (kT)^{-1}$, $\Delta G(t)$ is the external potential, and ΔG° is the redox potential of the A/B redox couple[50,74]. In the standard electrochemical literature, the value of the transfer coefficient is usually related to the symmetry of the energy barrier in going from A to B, and is equal to 0.5 in the case where the barrier from A to B is completely symmetric. For both Nernstian and Butler-Volmer dynamics we also assume that the flux of species A and B are equal and opposite at the electrode, $J_A = -J_B$. When supplemented with one more equation to ensure mass conservation, the above equations define either Nernstian (equation 3.4) or Butler-Volmer (equations 3.5 and 3.6) electrochemical dynamics. For more details about the implementation of these conditions, see Appendix III.

Solving the above boundary value problem has a long history, attempted first by Randles[75]

and Sevcik[76]. In the case of Nernstian dynamics for a linear sweep voltammetry experiment, there exists analytical values for the peak current and peak potential, I_p and ΔG_p, found by Laplace transforming the diffusion equations in 3.1(b) and employing the initial and boundary conditions in equations 3.2-3.4[77]. Assuming units of current in amperes, electrode area A in cm^2, diffusion constant D in cm^2/s, the scan rate ν in V/s and concentration c_A in mol/cm^3, one arrives at

$$I_p = (2.69 \times 10^5) n^{3/2} A D_A^{1/2} \nu^{1/2} c_A(t=0) \tag{3.7}$$

for the peak current and

$$\Delta G_p = \Delta G_{p/2} - 2.20 \frac{RT}{n\mathfrak{F}} \tag{3.8}$$

for the peak potential (in V). Here n is the number of electrons transferred in the ET event, $\mathfrak{F}$ is the Faraday constant, and $\Delta G_{p/2}$ is the half-peak potential[50], i.e. the driving force for which the current is half of the maximum current in equation 3.7. Equation 3.7 shows that, for Nernstian systems where ET kinetics are reversible, I_p is proportional to $\nu^{1/2}$ and does not depend on k°. For systems that exhibit more complicated dynamics than those of the reversible case, the values of I_p and ΔG_p become more complicated functions of a unitless parameter $\Lambda \equiv \frac{k^\circ}{\sqrt{\frac{D\nu\mathfrak{F}}{RT}}}$[78], which can be seen as a measure of the relative rates of ET kinetics (k°) and mass transfer kinetics ($\sqrt{\frac{D\nu\mathfrak{F}}{RT}}$). The statements above can be extended beyond linear sweeps to the case of cyclic voltammetry, although again, exact analytical expressions exist only for the Nernstian case[79,80].

A generalized SH approach with flexible boundary conditions

The Butler-Volmer dynamics described above show similarities to a stochastic master equation approach. In fact, with a little work, it can be easily shown that equations 3.1 and 3.5 are identical to classical surface hopping solving for the dynamics of coupled nuclear and electronic motion near a metal surface. To be precise, consider the following generalized Anderson-Holstein (AH) Hamiltonian, where an electronic impurity (i.e. a redox-active

molecule) is coupled to a collection of nuclei (with position $\hat{q}_\alpha$ and momentum $\hat{\Pi}_\alpha$ and $[\hat{q}_\alpha, \hat{\Pi}_\alpha] = i\hbar$) and a bath of metallic fermions (indexed by k):

$$H = H_s + H_b + H_c \tag{3.9a}$$

$$H_s = E(\vec{r})d^\dagger d + U_A(\vec{r}) + \frac{\vec{p}\cdot\vec{p}}{2m} + H_p \tag{3.9b}$$

$$H_p = \sum_\alpha \left[\frac{1}{2}\left(\frac{\Pi_\alpha^2}{m_\alpha} + m_\alpha\omega_\alpha^2 q_\alpha^2\right) + \left(g_\alpha q_\alpha \vec{r} + \frac{(g_\alpha\vec{r})^2}{2m_\alpha\omega_\alpha^2}\right)\right] \tag{3.9c}$$

$$H_b = \sum_k (\epsilon_k - \mu)c_k^\dagger c_k \tag{3.9d}$$

$$H_c = \sum_k W_k(\vec{r})(c_k^\dagger d + d^\dagger c_k) \tag{3.9e}$$

Here H_s represents a Hamiltonian for a molecule with molecular orbital d near a metal surface; H_p represents a collection of nuclear coordinates that lead to friction for the molecule; H_b represents a metal surface with multiple electronic states, indexed by k; and H_c represents the coupling between electrons in the metal and molecule. $\vec{r}$ is the position operator for the electronic impurity; in principle, $\vec{r}$ in equation 3.9 represents a multidimensional nuclear coordinate, however, in one dimension $\vec{r}$ becomes a scalar variable x. g_α is the coupling between the molecule and the collection of nuclei indexed by coordinate α, $d/d^\dagger$ represent creation and annihilation operators for a molecular orbital near a surface, μ is the chemical potential of the metal, $c_k/c_k^\dagger$ are the annihilation and creation operators for the metallic bath of electronic states, and W_k is the coupling between the electronic bath and the molecular orbital d. In practice, we will use the function Γ,

$$\Gamma(\vec{r}, \epsilon) = 2\pi \sum_k |W_k(\vec{r})|^2 \delta(\epsilon_k - \epsilon), \tag{3.10}$$

to characterize the strength of the electron-metal coupling, where $\frac{\hbar}{\Gamma}$ is the lifetime of an electron placed on the molecule. In the wide band limit, one can assume $\Gamma(\vec{r}, \epsilon)$ depends only on $\vec{r}$ (and not on ϵ).

The model in equation 3.9 incorporates two potential energy surfaces (PESs): we define U_A to be the diabatic PES for the case where the impurity is unoccupied and we define U_B

to be the diabatic PES for the case where the impurity is occupied. Thus, the function E in equation 3.9(b) can be defined as the difference between the diabatic states, $E(\vec{r}) \equiv U_B(\vec{r}) - U_A(\vec{r})$. Furthermore, in one dimension, it is standard to choose flat potential energy surfaces with no x dependence[81], such that

$$U_B \equiv U_A + \Delta G \tag{3.11a}$$

$$E = \Delta G. \tag{3.11b}$$

A Classical Master Equation (CME) for solving the AH model: As shown in Ref. 17, if we consider the limit of weak coupling Γ and high temperature (where all nuclear motion is classical), and the limit of strong friction so that all translational motion is diffusive and governed by the Smoluchowski equation, one can propagate dynamics for the Hamiltonian in equation 3.9 by solving the relevant master equation of the form:

$$\begin{aligned} \frac{\partial c_A}{\partial t} =& -\vec{\nabla} \cdot \vec{J_A} - (k_f c_A - k_b c_B)\delta(x) \\ =& D_A^x \frac{\partial^2 c_A}{\partial x^2} - (k_f c_A - k_b c_B)\delta(x) \end{aligned} \tag{3.12a}$$

$$\begin{aligned} \frac{\partial c_B}{\partial t} =& -\vec{\nabla} \cdot \vec{J_B} + (k_f c_A - k_b c_B)\delta(x) \\ =& D_B^x \frac{\partial^2 c_B}{\partial x^2} + (k_f c_A - k_b c_B)\delta(x). \end{aligned} \tag{3.12b}$$

Here, we have assumed $\Gamma(x) = \Gamma_0 \delta(x)$ so that all hopping occurs at only $x = 0$. The relevant electrode and bath boundary conditions are

$$c_A(t, x = -1) = c_A(t, x = 0) \tag{3.13a}$$

$$c_B(t, x = -1) = c_B(t, x = 0) \tag{3.13b}$$

$$c_A(t, x = \infty) = 1 \tag{3.13c}$$

$$c_B(t, x = \infty) = 0. \tag{3.13d}$$

Here, we have invoked a fictitious boundary point at $x = -1$[82]. In principle, equation 3.12 can be solved by sampling over a swarm of trajectories hopping back and forth between surfaces and undergoing stochastic motion with Langvein forces. However, to save time, we will integrate 3.12 directly, solving for the time dependence of the probability densities as they are propagated with the coupled Smoluchowski equations.

Now, to prove the equivalence between equations 3.1, 3.5, and 3.12 we simply integrate both sides of equation 3.12 over a small length ϵ, where $\epsilon \to 0$:

$$\begin{aligned} \int_{-\epsilon}^{\epsilon} \frac{\partial c_A}{\partial t}\, dx &= \int_{-\epsilon}^{\epsilon} (D_A^x \frac{\partial^2 c_A}{\partial x^2} - (k_f c_A + k_b c_B)\delta(x))\, dx \\ 0 &= D_A \frac{\partial c_A}{\partial x}|_{x=0} - k_f c_A|_{x=0} + k_b c_B|_{x=0} \end{aligned} \tag{3.14a}$$

$$\begin{aligned} \int_{-\epsilon}^{\epsilon} \frac{\partial c_B}{\partial t}\, dx &= \int_{-\epsilon}^{\epsilon} (D_B \frac{\partial^2 c_B}{\partial x^2} + (k_f c_A - k_b c_B)\delta(x))\, dx \\ 0 &= D_B \frac{\partial c_B}{\partial x}|_{x=0} + k_f c_A|_{x=0} - k_b c_B|_{x=0}. \end{aligned} \tag{3.14b}$$

These are the Butler-Volmer boundary conditions. Apparently, adjusting the boundary conditions at $x = 0$ (the electrode surface) can reproduce Butler-Volmer dynamics entirely and with more generality, giving us another view of electrochemical dynamics. Note that, with the diffusion equations in equation 3.12, we find that the units of k_f and k_b are $\frac{cm}{s}$, not s^{-1}.

Including reactions far from the surface: Before proceeding further, one more point is now appropriate. The differential equation modeling electron transfer (equation 3.12) can be modified easily to include pre- and post- reactions. For the series of chemical reactions

$$\begin{aligned} \mathrm{A} + \mathrm{e}^- &\underset{\mathrm{k_b}}{\overset{\mathrm{k_f}}{\rightleftharpoons}} \mathrm{B} \\ \mathrm{B} &\xrightarrow{\mathrm{k_r}} \mathrm{Z} \end{aligned} ,$$

where Z is an electronically inactive species, the differential equation in equation 3.12 simply

becomes

$$\frac{\partial c_A}{\partial t} = D_A^x \frac{\partial^2 c_A}{\partial x^2} - (k_f c_A - k_b c_B)\delta(x) \tag{3.15a}$$

$$\frac{\partial c_B}{\partial t} = D_B^x \frac{\partial^2 c_B}{\partial x^2} + (k_f c_A - k_b c_B)\delta(x) - k_r c_B. \tag{3.15b}$$

In this case, k_f and k_b have different units from k_r; the rate constants k_f and k_b have units of $\frac{cm}{s}$ and k_r has units of s^{-1}. Note that the delta function $\delta(x)$ from equations 3.12 and 3.15 has units of cm^{-1}.

Ramp speed and measuring current

In order to model a linear sweep voltammetry or a cyclic voltammetry experiment, one must propagate the diffusion equations forward in time, while also changing the potential ($\Delta G(t)$ in equations 3.6 and 3.11). For our purposes, we will imagine that the potential is ramped according to the following equation

$$\Delta G(t) = \Delta G_i + \nu t \tag{3.16}$$

where ν is the scan rate and ΔG_i is the starting potential. For the cyclic voltammetry experiments, once $\Delta G(t) = \Delta G_f = -\Delta G_i$ the scan is reversed and carried out until $\Delta G(t) = \Delta G_i$. Current in these experiments can be calculated in at least two equivalent ways:

$$I(t) = n\mathfrak{F}AD_A^x \frac{\partial c(t)}{\partial x}|_{x=0} \tag{3.17a}$$

or

$$I(t) = n\mathfrak{F}A(k_f(t)c_A(t) - k_b(t)c_B(t))|_{x=0}. \tag{3.17b}$$

Here $\mathfrak{F}$ is the Faraday constant, A is the area of the electrode surface, and n is the number of electrons transferred in the electron transfer. For simplicity, we set $n\mathfrak{F}A = 1$.

3.2.2. Electrochemical dynamics in two dimensions

SH in 2D: explicitly modeling ET through a solvent reorganization coordinate

As described above, simple Butler-Volmer kinetics model electrochemical ET effectively through one parameter α; thus, the kinetics implicitly assume that ET dynamics are dictated by slow, rate-limiting motion along a generalized diffusion coordinate from bulk to the surface. While this approach is often reasonable in solution (for outer sphere ET), it is also true that dynamics are often limited by water reorganization and other solvent effects (as argued originally by Marcus[83]). Thus, one can easily imagine at least two possible reaction coordinates. With this motivation in mind, and having already reviewed the basic theory of one-dimensional electrochemical dynamics for modeling CV experiments, we will now construct a multidimensional problem by including an additional degree of freedom into our Hamiltonian: an effective solvent reorganization coordinate ζ. Mathematically, we choose a Hamiltonian of the form from equation 3.9, with $\vec{r} = (x, \zeta)$. For simplicity, we suppose that the PESs for species A and B are quadratic wells, with nuclear frequency ω, mass m, and centered at ζ_A (ζ_B),

$$U_A(x, \zeta) = \tfrac{1}{2} m\omega^2 (\zeta_A(x) - \zeta)^2 \tag{3.18a}$$

$$U_B(\zeta) = \tfrac{1}{2} m\omega^2 (\zeta_B - \zeta)^2 + \Delta G \tag{3.18b}$$

$$E(x, \zeta) = U_B - U_A = \tfrac{1}{2} m\omega^2 (\zeta_B^2 - \zeta_A^2(x) - 2(\zeta_B - \zeta_A(x))\zeta) + \Delta G \tag{3.18c}$$

where U_A can have an x dependence through the diabat minimum position $\zeta_A(x)$, and ΔG is determined by the external voltage. Note that U_B is always independent of x.

To model the electrochemical dynamics, we discretize our electrochemical system on a 2D

grid, and we solve the following differential equations:

$$\begin{aligned}\vec{J_A} &= (-D_A^x \frac{\partial c_A}{\partial x} + \frac{F_A^x}{\gamma_x} c_A)\hat{x} + (-D_A^\zeta \frac{\partial c_A}{\partial \zeta} + \frac{F_A^\zeta}{\gamma_\zeta} c_A)\hat{\zeta} \\ \vec{J_B} &= (-D_B^x \frac{\partial c_B}{\partial x} + \frac{F_B^x}{\gamma_x} c_B)\hat{x} + (-D_B^\zeta \frac{\partial c_B}{\partial \zeta} + \frac{F_B^\zeta}{\gamma_\zeta} c_B)\hat{\zeta}\end{aligned} \tag{3.19a}$$

$$\begin{aligned}\frac{\partial c_A}{\partial t} =& D_A^x \frac{\partial^2 c_A}{\partial x^2} + D_A^\zeta \frac{\partial^2 c_A}{\partial \zeta^2} - \frac{F_A^x}{\gamma_x}\frac{\partial c_A}{\partial x} - \frac{\partial F_A^x}{\partial x}\frac{c_A}{\gamma_x} \\ & - \frac{F_A^\zeta}{\gamma_\zeta}\frac{\partial c_A}{\partial \zeta} - \frac{\partial F_A^\zeta}{\partial \zeta}\frac{c_A}{\gamma_\zeta} - (k_f c_A - k_b c_B) \\ \frac{\partial c_B}{\partial t} =& D_B^x \frac{\partial^2 c_B}{\partial x^2} + D_B^\zeta \frac{\partial^2 c_B}{\partial \zeta^2} - \frac{F_B^x}{\gamma_x}\frac{\partial c_B}{\partial x} - \frac{\partial F_B^x}{\partial x}\frac{c_B}{\gamma_x} \\ & - \frac{F_B^\zeta}{\gamma_\zeta}\frac{\partial c_B}{\partial \zeta} - \frac{\partial F_B^\zeta}{\partial \zeta}\frac{c_B}{\gamma_\zeta} + (k_f c_A - k_b c_B)\end{aligned} \tag{3.19b}$$

$$\begin{aligned}c_A(t, x = -1, \zeta) &= c_A(t, x = 0, \zeta) \\ c_B(t, x = -1, \zeta) &= c_B(t, x = 0, \zeta).\end{aligned} \tag{3.19c}$$

D^x, D^ζ are diffusion coefficients in the x and ζ directions, respectively, γ_x, γ_ζ are friction coefficients in the x and ζ directions, respectively ($\gamma_x = \frac{kT}{D^x}$, $\gamma_\zeta = \frac{kT}{D^\zeta}$), and F^x, F^ζ are the mean force acting on a given species in the x and ζ directions, respectively. From equation 3.18, the relevant forces are:

$$F_A^\zeta(x, \zeta) = m\omega^2(\zeta_A(x) - \zeta) \tag{3.20a}$$

$$F_A^x(x, \zeta) = -m\omega^2(\zeta_A(x) - \zeta)\frac{d\zeta_A}{dx} \tag{3.20b}$$

$$F_B^\zeta(\zeta) = m\omega^2(\zeta_B - \zeta) \tag{3.20c}$$

$$F_B^x(\zeta) = 0 \tag{3.20d}$$

To visualize the effect of ΔG on the PESs, see figure 3.1. The addition of the ζ coordinate allows us to model electron transfer in the form of "hops" between the species, represented by hopping rates k_f and k_b. These hopping rates depend on the coordinate ζ, and are given

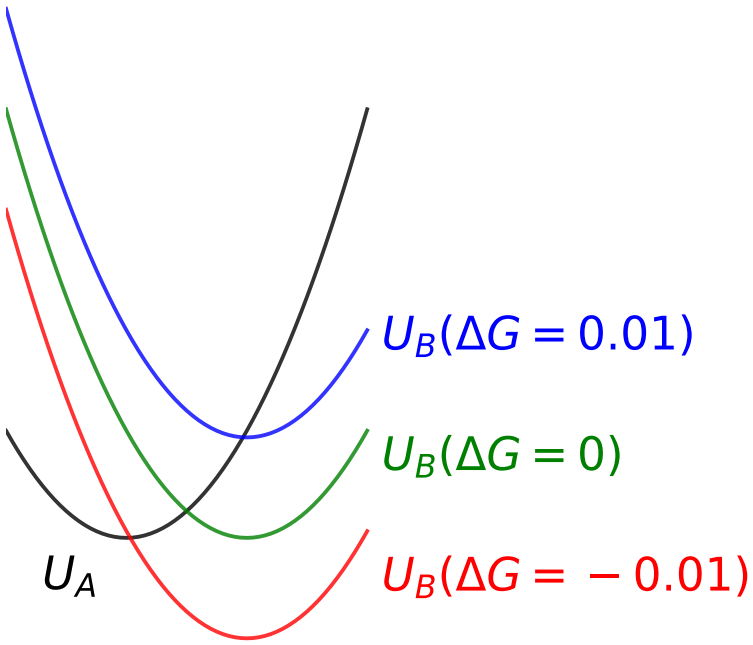

Figure 3.1: Illustration of the vertical shift in energy that occurs when changing the external voltage, and subsequently ΔG, on the PES U_B from equation 3.18.

by

$$k_f(x,\zeta) = \frac{\Gamma(x)}{\hbar} f(E(x,\zeta)) \tag{3.21a}$$

$$k_b(x,\zeta) = \frac{\Gamma(x)}{\hbar}(1 - f(E(x,\zeta))) \tag{3.21b}$$

$$\Gamma(x) = \Gamma_0 \delta(x) \tag{3.21c}$$

where $\Gamma(x)$ is the function that represents the strength of the electrode-molecule coupling and $f(E) = \frac{1}{1+e^{\beta E}}$ is the fermi function.

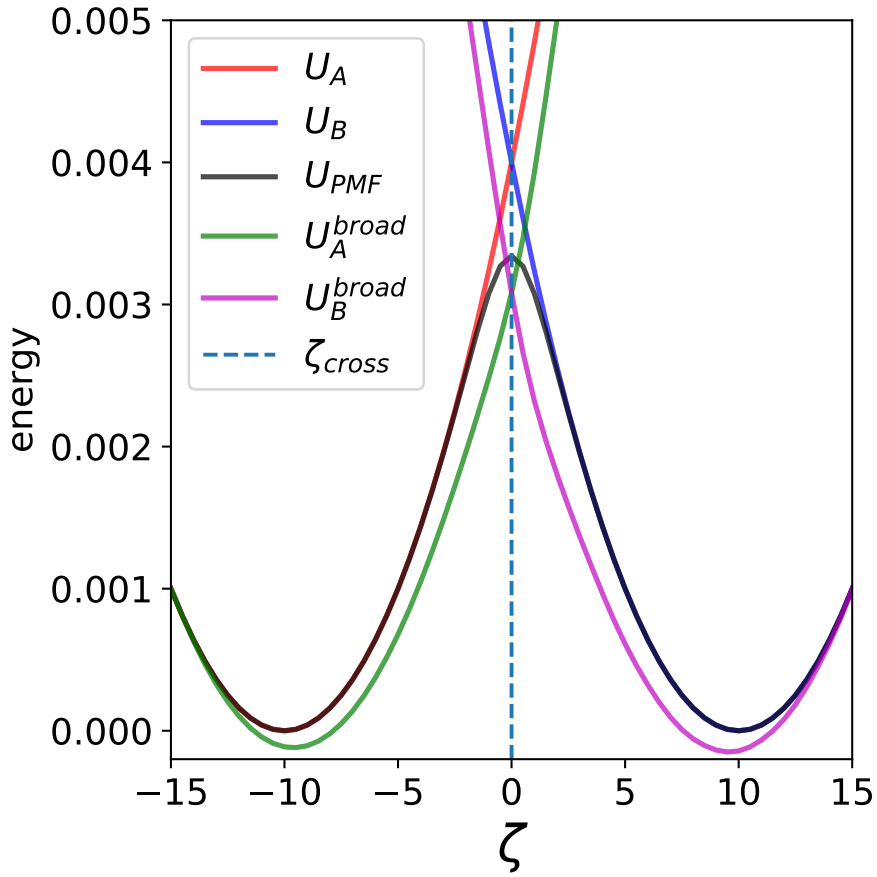

Figure 3.2: Potential energy surfaces as a function of the solvent reorganization coordinate ζ, unbroadened (U_A and U_B) and broadened (U_A^{broad} and U_B^{broad}), and potentials of mean force (U_{PMF}), for diabats in equation 3.18 and 3.29, with $m = 2000$, $\omega = 0.0002$, $\zeta_A = -10$, $\zeta_B = 10$, $\Gamma = 0.002$, and $\Delta G = 0$. All parameters are in atomic units (a.u.).

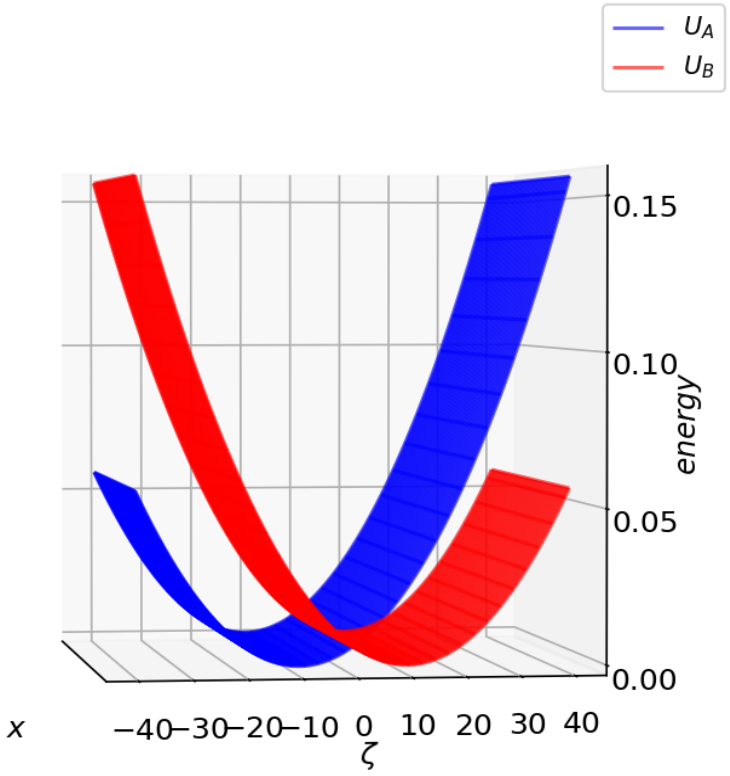

Figure 3.3: Potential energy surfaces as a function of the diffusion coordinate x and solvent reorganization coordinate ζ, with $m = 2000$, $\omega = 0.00025$, $\zeta_A = -10$, $\zeta_B = 10$, $\Gamma = 10^{-6}$, and $\Delta G = 0$. All parameters are in atomic units (a.u.).

The system is governed by the following initial conditions,

$$c_A(t=0,x,\zeta) = \frac{e^{-\beta U_A(x,\zeta)}}{\int d\zeta e^{-\beta U_A(x,\zeta)}} \tag{3.22a}$$

$$c_B(t=0,x,\zeta) = 0 \tag{3.22b}$$

and boundary conditions

$$c_A(t,x=\infty,\zeta) = \frac{e^{-\beta U_A(x,\zeta)}}{\int d\zeta e^{-\beta U_A(x,\zeta)}} \tag{3.23a}$$

$$c_B(t,x=\infty,\zeta) = 0 \tag{3.23b}$$

$$c_A(t,x,\zeta=\pm\infty) = c_B(t,x,\zeta=\pm\infty) = 0, \tag{3.23c}$$

The initial conditions in equation 3.22 enforce the fact that only A is present initially, and at a uniform concentration everywhere in the x direction; furthermore, there is a Boltzmann distribution in the ζ direction. The boundary conditions in equation 3.23 enforce the fact that there is no concentration of either species at the boundaries of the ζ coordinate ($\zeta \to \pm\infty$), and that the concentration of A and B are equal to their initial concentrations infinitely far from the electrode in the x direction ($x \to \infty$). For simplicity, we fix the diffusion constant to be constant and equal for both species A and B ($D_A^x = D_B^x = D_A^\zeta = D_B^\zeta$).

Nuances of broadening: a broadened classical master equation (BCME)

In cases where the metal molecule coupling Γ is larger than kT, level broadening becomes important: for molecules chemisorbed or physisorbed on surfaces, electrons are shared in an adiabatic state quantum mechanically between molecule and surface, and electronic motion is not simply hopping back and forth. To capture the more complex hybridized dynamics that arise from the continuum of electronic states in the metal, a reasonable fix is to modify

our diabatic forces as follows[38]:

$$F_A^{x,broad}(x,\zeta) = -m\omega^2(\zeta_A(x)-\zeta)\tfrac{d\zeta_A}{dx} - \tfrac{dE}{dx}(n(E(x,\zeta)) - f(E(x,\zeta))) \tag{3.24a}$$

$$F_A^{\zeta,broad}(x,\zeta) = m\omega^2(\zeta_A(x)-\zeta) - \tfrac{dE}{d\zeta}(n(E(x,\zeta)) - f(E(x,\zeta))) \tag{3.24b}$$

$$F_B^{x,broad}(x,\zeta) = -\tfrac{dE}{dx}(n(E(x,\zeta)) - f(E(x,\zeta))) \tag{3.24c}$$

$$F_B^{\zeta,broad}(x,\zeta) = m\omega^2(\zeta_B-\zeta) - \tfrac{dE}{d\zeta}(n(E(x,\zeta)) - f(E(x,\zeta))). \tag{3.24d}$$

Here $n(E)$ is the broadened population and W is the electronic bandwidth,

$$n(E) = \int_{-W}^{W} \frac{d\epsilon}{2\pi} \frac{\Gamma}{(\epsilon - E)^2 + \frac{\Gamma^2}{4}} f(\epsilon), \tag{3.25}$$

chosen such that $W \gg \Gamma$. To visualize the surfaces from equation 3.18 and 3.24, see figure 3.2, and to visualize the 2D surfaces, see figure 3.3.

Measuring current in 2D

For all calculations where we explicitly model ζ, one can calculate current in two different ways:

$$\begin{aligned} I(t) =& n\mathfrak{F}AD_A^x \int_{\zeta_i}^{\zeta_f} d\zeta \frac{\partial c_A(t,\zeta_i)}{\partial x}|_{x=0} \\ I(t) \approx& n\mathfrak{F}AD_A^x \sum_i^{N_\zeta} d\zeta \frac{\partial c_A(t,\zeta_i)}{\partial x}|_{x=0} \end{aligned} \tag{3.26a}$$

or

$$\begin{aligned} I(t) =& n\mathfrak{F}A \int_{\zeta_i}^{\zeta_f} d\zeta (k_f(t,\zeta_i)c_A(t,\zeta_i) - k_b(t,\zeta_i)c_B(t,\zeta_i))|_{x=0} \\ I(t) \approx& n\mathfrak{F}A \sum_i^{N_\zeta} d\zeta (k_f(t,\zeta_i)c_A(t,\zeta_i) - k_b(t,\zeta_i)c_B(t,\zeta_i))|_{x=0}. \end{aligned} \tag{3.26b}$$

Coarse graining and marginalizing out ζ: The 1D Marcus-Hush (MH) model

Equation 3.19 represents a general approach to modeling electrochemical ET and yet one often seeks the simplest possible approach. To that end, one often seeks to marginalize out the reorganization coordinate direction, leading to the following marginal probability distribution $c(x,t)$:

$$\begin{aligned} \vec{J_A} &= -D_A^x \frac{\partial c_A}{\partial x}\hat{x} \\ \vec{J_B} &= -D_B^x \frac{\partial c_B}{\partial x}\hat{x} \end{aligned} \tag{3.27a}$$

$$\begin{aligned} \frac{\partial c_A}{\partial t} =& -\vec{\nabla}\cdot\vec{J_A} - (\widetilde{k_f}c_A - \widetilde{k_b}c_B)\delta(x) \\ =& D_A^x \frac{\partial^2 c_A}{\partial x^2} - (\widetilde{k_f}c_A - \widetilde{k_b}c_B)\delta(x) \\ \frac{\partial c_B}{\partial t} =& -\vec{\nabla}\cdot\vec{J_B} + (\widetilde{k_f}c_A - \widetilde{k_b}c_B)\delta(x) \\ =& D_B^x \frac{\partial^2 c_B}{\partial x^2} + (\widetilde{k_f}c_A - \widetilde{k_b}c_B)\delta(x). \end{aligned} \tag{3.27b}$$

Obviously, equation 3.27 is equivalent to equation 3.12, although in this case the motion in the ζ direction gives a new average hopping rate, $\widetilde{k}_{f/b}$,

$$\widetilde{k_f} = \frac{\Gamma_0}{\hbar}\frac{\int_{-\infty}^{\infty} d\zeta\ e^{-\beta U_A(0,\zeta)} f(E(0,\zeta))}{\int_{-\infty}^{\infty} d\zeta\ e^{-\beta U_A(0,\zeta)}} \tag{3.28a}$$

$$\widetilde{k_b} = \frac{\Gamma_0}{\hbar}\frac{\int_{-\infty}^{\infty} d\zeta\ e^{-\beta U_B(\zeta)}(1-f(E(0,\zeta)))}{\int_{-\infty}^{\infty} d\zeta\ e^{-\beta U_B(\zeta)}}. \tag{3.28b}$$

The rates $\widetilde{k_f}$, $\widetilde{k_b}$ are just the original hopping rates weighted by the Boltzmann average of being at a given position in ζ at $x = 0$. Equation 3.28 arises from the assumption that equilibration in ζ is fast relative to other time scales in the simulation. For the Hamiltonian in equation 3.9 with roughly equal diffusion in x and ζ, the relevant condition for fast nuclear equilibration relative to the timescale of driving force is $\frac{m\omega^2}{\gamma} = \frac{Dm\omega^2}{kT} > \frac{\nu}{kT}$. This condition states that the time required to change the driving force by kT should be larger than the relaxation time of a damped harmonic oscillator (which in the overdamped limit is $\frac{m\omega^2}{\gamma}$). This condition should be satisfied for almost all experiments.

Implementation of $\tilde{k}_f$ and $\tilde{k}_b$ as the rate constants for Butler-Volmer dynamics in equation 3.5 in lieu of the rate constants in equation 3.6 is known in the electrochemical literature as the Marcus-Hush (MH) boundary conditions[84]. Obviously, equations 3.28a and 3.28b are equivalent to the Marcus electrochemical rate constants; in this paper, even though we are in the slightly overdamped regime, the Zusman corrections (for solvent overdamping effects on the rate constant) should be small and will not be considered. Below, we will refer to the utilization of the rate constants $\tilde{k}_f$ and $\tilde{k}_b$ in the SH framework as a 1D MH model. Note that, if Γ is larger than kT, then the potentials U_A and U_B (within the BCME approximation) in the above equations need to be replaced with the broadened PESs,

$$U_A^{broad}(0,\zeta) = \frac{1}{2}m\omega^2(\zeta_A(0)-\zeta)^2 + \int_{\zeta_0}^{\zeta} d\zeta'(n(E(0,\zeta')) - f(E(0,\zeta')))\frac{dE}{d\zeta'} \tag{3.29a}$$

$$U_B^{broad}(0,\zeta) = \frac{1}{2}m\omega^2(\zeta_B-\zeta)^2 + \Delta G + \int_{\zeta_0}^{\zeta} d\zeta'(n(E(0,\zeta')) - f(E(0,\zeta')))\frac{dE}{d\zeta'}. \tag{3.29b}$$

3.2.3. Alternative to solving ODE: diagonalizing the Fokker-Planck operator

The simplest means to propagate the electrochemical dynamics in equations 3.12, 3.19, and 3.27 is to use an implicit ordinary differential equation (ODE) solver. Note that an implicit ODE solver is necessary because a more conventional explicit ODE solver (e.g. RK4[85]) is unstable for this purpose. The root of the problem is the stiff behavior of these ODEs[86]; for the 1D data in the results and discussion, we have chosen to use the Real-valued Variable-coefficient Ordinary Differential Equation ('vode') solver with the backward difference formula (BDF) method[87].

As an alternative to 'vode', there is another approach: namely, one can cast $\frac{\partial c_A}{\partial t}$ ($\frac{\partial c_B}{\partial t}$) as a matrix equation and diagonalize the corresponding matrix operator to obtain an exact answer for the time evolution of c_A (c_B)[88]. Diagonalization of this 'Fokker-Planck' operator has been previously applied to study ET dynamics in a two state system with diffusion[89].

For our purposes, equation 3.12 can be written in the following way:

$$\frac{\partial c_A}{\partial t} = \mathfrak{L}_A^x c_A - (k_f c_A - k_b c_B)\delta(x) \tag{3.30a}$$

$$\frac{\partial c_B}{\partial t} = \mathfrak{L}_B^x c_B + (k_f c_A - k_b c_B)\delta(x). \tag{3.30b}$$

Here, we define superoperators:

$$\mathfrak{L}_A^x = \frac{\partial}{\partial x}(D_A^x \frac{\partial}{\partial x} - \frac{F_A^x}{\gamma_x}) \tag{3.31a}$$

$$\mathfrak{L}_B^x = \frac{\partial}{\partial x}(D_B^x \frac{\partial}{\partial x} - \frac{F_B^x}{\gamma_x}), \tag{3.31b}$$

and we allow for a drift term $\frac{F^x}{\gamma_x}$ for generality; note that, for the case of equation 3.12, $F^x \equiv 0$. Similarly, equation 3.19 can be written as:

$$\frac{\partial c_A}{\partial t} = (\mathfrak{L}_A^x + \mathfrak{L}_A^\zeta)c_A - (k_f c_A - k_b c_B)\delta(x) \tag{3.32a}$$

$$\frac{\partial c_B}{\partial t} = (\mathfrak{L}_B^x + \mathfrak{L}_B^\zeta)c_B + (k_f c_A - k_b c_B)\delta(x) \tag{3.32b}$$

$$\mathfrak{L}_A^\zeta = \frac{\partial}{\partial \zeta}(D_A^\zeta \frac{\partial}{\partial \zeta} - \frac{F_A^\zeta}{\gamma_\zeta}) \tag{3.32c}$$

$$\mathfrak{L}_B^\zeta = \frac{\partial}{\partial \zeta}(D_B^\zeta \frac{\partial}{\partial \zeta} - \frac{F_B^\zeta}{\gamma_\zeta}). \tag{3.32d}$$

By combining $\mathfrak{L}_A^x, \mathfrak{L}_B^x, \mathfrak{L}_A^\zeta, \mathfrak{L}_B^\zeta, k_f$, and k_b we obtain the general matrix equation for both c_A and c_B,

$$\begin{pmatrix} \dot{c_A} \\ \dot{c_B} \end{pmatrix} = \begin{pmatrix} \mathfrak{L}_A - k_f\delta(x) & k_b\delta(x) \\ k_f\delta(x) & \mathfrak{L}_B - k_b\delta(x) \end{pmatrix} \begin{pmatrix} c_A \\ c_B \end{pmatrix} + \vec{y} \tag{3.33}$$
$$\dot{\vec{c}} = \mathfrak{M}\vec{c} + \vec{y}$$

where $\mathfrak{L}_A = \mathfrak{L}_A^x$ ($\mathfrak{L}_B = \mathfrak{L}_B^x$) in the 1D model and $\mathfrak{L}_A = \mathfrak{L}_A^x + \mathfrak{L}_A^\zeta$ ($\mathfrak{L}_B = \mathfrak{L}_B^x + \mathfrak{L}_B^\zeta$) in the

2D model. Here, the term $\vec{y}$ is used to include the bath conditions from equations 3.13 and 3.23 which maintain a static condition at the bath boundary, i.e. $\dot{\vec{c}}(x=\infty)=\vec{0}$. In other words, $\vec{y}(x\neq\infty)=0$ and $\vec{y}(x=\infty)=-(\mathfrak{M}\vec{c})(x=\infty)$.

Obviously, $\mathfrak{M}$ is in general non-Hermitian, given that (i) $\mathfrak{L}_A$ ($\mathfrak{L}_B$) is non-Hermitian if there is a potential U_A (U_B), and (ii) the off-diagonal elements of $\mathfrak{M}$ are not equal ($k_f \neq k_b$) unless $E=0$. Since diagonalization of non-Hermitian matrices is often unstable, one would like to transform $\mathfrak{M}$ into a Hermitian matrix. To do so, there is a common method[90] for converting the non-Hermitian operator $\mathfrak{L}_A$ ($\mathfrak{L}_B$) to a Hermitian operator $\widetilde{\mathfrak{L}}_A$ ($\widetilde{\mathfrak{L}}_B$),

$$\widetilde{\mathfrak{L}}_A = e^{\frac{\beta U_A}{2}}\mathfrak{L}_A e^{-\frac{\beta U_A}{2}} \tag{3.34a}$$

$$\widetilde{\mathfrak{L}}_B = e^{\frac{\beta U_B}{2}}\mathfrak{L}_B e^{-\frac{\beta U_B}{2}}. \tag{3.34b}$$

With the above transformation of $\mathfrak{L}_A$ ($\mathfrak{L}_B$) in mind, we can define a similarity transformation matrix S as

$$S = \begin{pmatrix} e^{\frac{\beta U_A}{2}} & 0 \\ 0 & e^{\frac{\beta U_B}{2}} \end{pmatrix}, \tag{3.35}$$

such that the new operator $\widetilde{\mathfrak{M}}$

$$\widetilde{\mathfrak{M}} = S\mathfrak{M}S^{-1} = \begin{pmatrix} \widetilde{\mathfrak{L}}_A - k_f\delta(x) & k_b\delta(x)e^{-\frac{\beta E}{2}} \\ k_f\delta(x)e^{\frac{\beta E}{2}} & \widetilde{\mathfrak{L}}_B - k_b\delta(x) \end{pmatrix} \tag{3.36}$$

is Hermitian and can be easily diagonalized. While the eigenvectors of $\widetilde{\mathfrak{M}}$ will differ from those of $\mathfrak{M}$, $\mathfrak{M}$ and $\widetilde{\mathfrak{M}}$ are related by a similarity transformation, so that the eigenvalues are identical for both and one can analyze the dynamics of the system at any arbitrary time. Note that, in equation 3.36 for a 2D simulation, k_f, k_b, and E are functions of the coordinates x and ζ.

Simulating a linear sweep voltammetry experiment can be done with matrix algebra by diagonalization of $\widetilde{\mathfrak{M}}$ at each time step (since $\widetilde{\mathfrak{M}}$ is a function of $\Delta G(t)$), yielding $\widetilde{\mathfrak{M}}=$

$P\Lambda P^T$. The eigenvalues Λ are always nonpositive, corresponding to decay rates along modes represented by the eigenvectors of P, and for such a dissipative system, there is always one zero eigenvalue corresponding to the equilibrium, or steady state[91]. At this point, we can change variables and recast the differential equation for the time evolution of c_A and c_B into renormalized coordinates:

$$\vec{b} \equiv P^T S \vec{c} \tag{3.37a}$$

$$\vec{z} \equiv P^T S \vec{y}. \tag{3.37b}$$

The final equation of motion becomes:

$$\dot{\vec{b}} = \Lambda \vec{b} + \vec{z}. \tag{3.37c}$$

Equation 3.37c can be solved exactly, with solution for any arbitrary time step given by

$$\vec{b}(t) = \vec{b}_{eq} + (\vec{b} - \vec{b}_{eq}) e^{\Lambda t} \tag{3.38a}$$

$$\vec{b}_{eq} = -\Lambda^{-1} \vec{z}. \tag{3.38b}$$

Finally, using equation 3.37a, we can convert $\vec{b}(t)$ back to $\vec{c}(t) = \begin{pmatrix} c_A \\ c_B \end{pmatrix}$ using P and S: $\vec{c} = S^{-1} P \vec{b}$. Hence, one can easily calculate the current at each time step with complete numerical stability.

3.2.4. Parameterization

We will work in standard units throughout this paper and, unless stated otherwise, set $\Delta G^\circ = 0$ V, $m = 1.82 \cdot 10^{-27} kg$ (2000 a.u.), $T = 300K$ (0.00095 a.u.), $\zeta_A(x) = \zeta_A^0 = -5.29$ Å (-10 a.u.), $\zeta_B = 5.29$ Å (10 a.u.), $W = 10^3 \cdot \Gamma$, $N_x = 50$, and $N_\zeta = 101$. The size of the grid in x is given by $L_x = 6\sqrt{D^x t_T}$, where t_T is the total time of the simulation, defined by the starting and ending ΔG and ν, $t_T = \frac{|\Delta G_f - \Delta G_i|}{\nu}$ for linear sweeps and $t = \frac{2|\Delta G_f - \Delta G_i|}{\nu}$

for cyclic sweeps. The size of the grid in ζ is given by $L_\zeta = 4(\zeta_B - \zeta_A)$, with endpoints $[4\zeta_A, 4\zeta_B]$, and the grid spacing in both x and ζ is uniform, such that $dx = \frac{L_x}{N_x}$ and $d\zeta = \frac{L_\zeta}{N_\zeta}$. The current values in figures 3.5, 3.6, 3.7, 3.8, 3.10 and 3.11 are rescaled by a factor of 10^9.

3.3. Results

We have thus far presented several distinct approaches for simulating electrochemical systems. To better understand these approaches, we will now consider a host of different situations and quantitatively analyze the prediction of each approach. When will different approaches agree? And if they disagree, which approach is appropriate?

3.3.1. Verification of 1D model

Our first goal is to numerically demonstrate the equivalence of surface hopping with boundary conditions (equations 3.12 and 3.13) against the Nernstian (equations 3.1 and 3.4) and Butler Volmer (equations 3.1 and 3.5) approaches. In figure 3.4 we plot simulated cyclic voltammograms for two chemical reaction types, with both methods for calculating current (equations 3.17(a)-(b)) and three different dynamics methods; Nernstian (equations 3.1 and 3.4), Butler-Volmer (equations 3.1 and 3.5), and surface hopping (equations 3.12 and 3.13). In all cases, we see excellent agreement between the surface hopping dynamics and the standard Nernstian and Butler-Volmer approaches (however current is calculated).

In addition to the case of a symmetric barrier between oxidation and reduction, the surface hopping method can also handle the case of an asymmetric barrier, $\alpha \neq 0.5$[92]. In figure 3.5 we plot results for the same models and parameterizations as in figure 3.4, but with $\alpha = 0.2$. Obviously, we do not expect Nernstian dynamics to recover the correct current due to the asymmetric barrier, but we do see quantitative agreement between the hopping approach and Butler-Volmer kinetics, providing additional validation for the hopping approach.

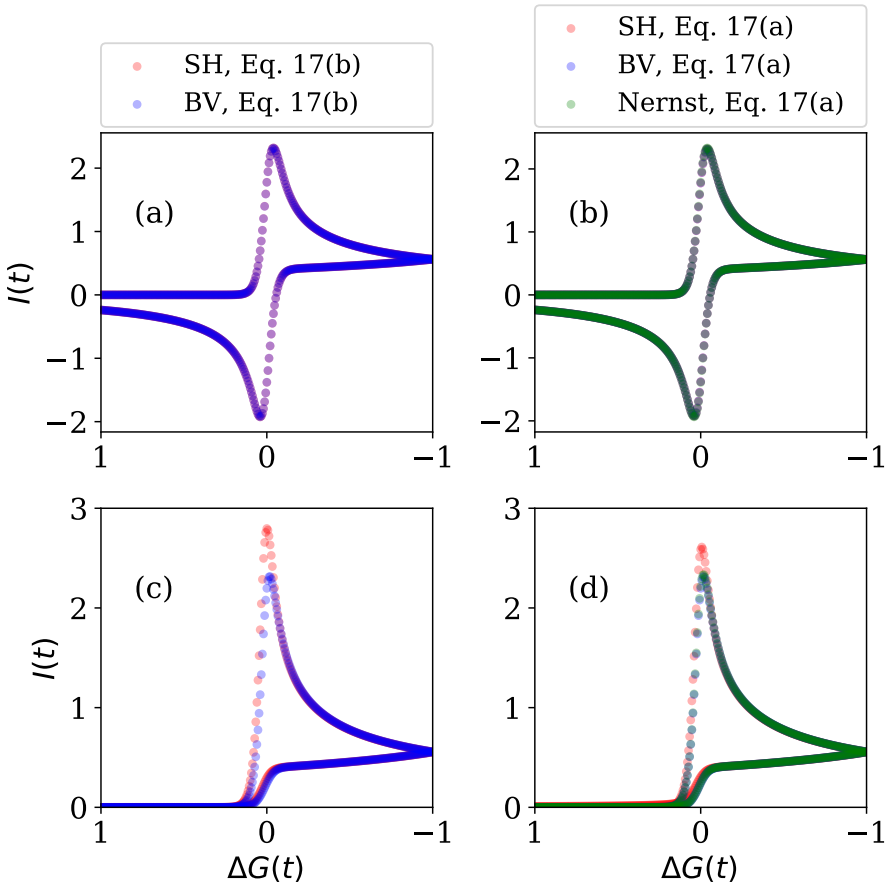

Figure 3.4: 1D Cyclic voltammograms (CV) for the reaction $A + e^- \underset{k_b}{\overset{k_f}{\rightleftharpoons}} B$, both with ((c) and (d)) and without ((a) and (b)) the post reaction $B \xrightarrow{k} Z$. (a) CV measuring current by the difference in forward and backward rates, without the post reaction $B \xrightarrow{k} Z$. (b) CV measuring current by the flux of A at the electrode, without the post reaction $B \xrightarrow{k} Z$. (c) CV measuring current by the difference in forward and backward rates, with the post reaction $B \xrightarrow{k} Z$. (d) CV measuring current by the flux of A at the electrode, with the post reaction $B \xrightarrow{k} Z$. Note that k_f and k_b are not explicitly modeled when using Nernst boundary conditions, preventing the use of the difference in forward and backward rates as a measure of current. Parameters are set to $D^x = 1$ cm^2/sec, $\nu = 1$ V/sec, $\Delta G_i = 1$ V, $\Delta G_f = -1$ V, $N_x = 200$, $k = 100$ sec^{-1}, $k^\circ = 1000$ cm/sec, $\alpha = 0.5$. We see quantitative agreement between the surface hopping dynamics and both Nernstian and Butler-Volmer dynamics, suggesting that all the approaches are applicable for simulating these systems.

3.3.2. Cases where 2D and 1D MH model agree

Next, we examine situations under which the 1D MH model can recover the same result as that of the full 2D model. Plotted in figures 3.6 and 3.7 are linear sweep voltammograms

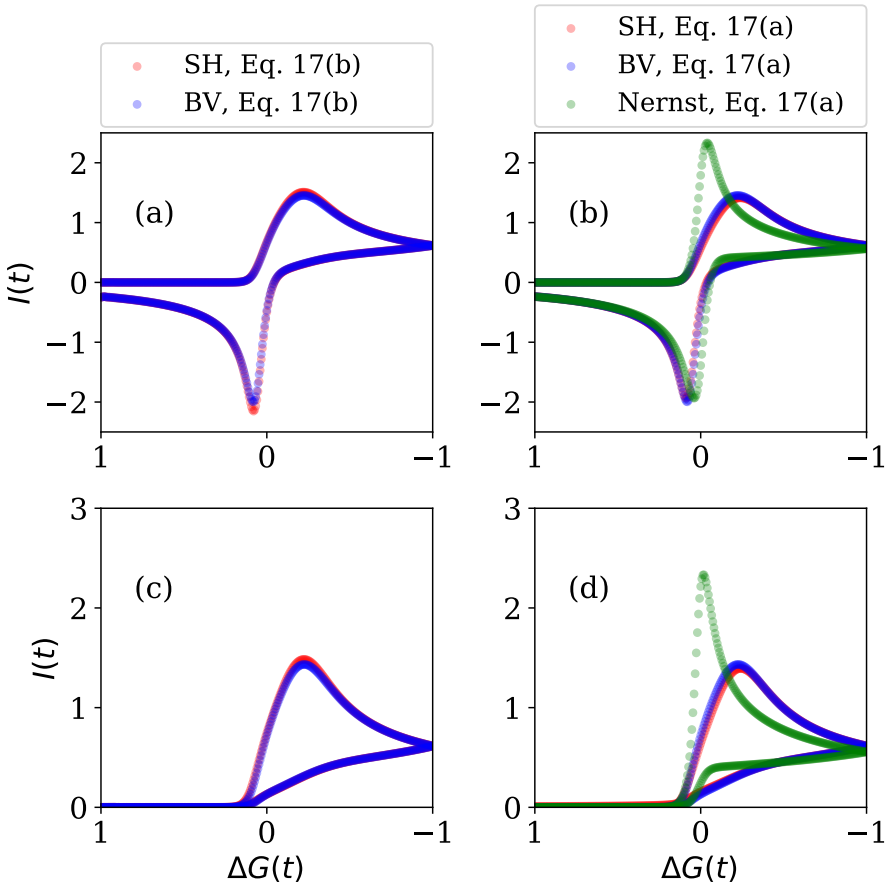

Figure 3.5: 1D Cyclic voltammograms (CV) for the same conditions as in figure 1, but with an asymmetric barrier between oxidation and reduction, given by $\alpha = 0.2$. Parameters are set to $D^x = 1$ cm^2/sec, $\nu = 1$ V/sec, $\Delta G_i = 1$ V, $\Delta G_f = -1$ V, $N_x = 200$, $k = 100$ sec^{-1}, $k^\circ = 1$ cm/sec, $\alpha = 0.2$. Note that k° is decreased relative to the symmetric case; if the kinetics are very facile, as evinced by a large k°, then the asymmetry of the barrier will have no effect on the dynamics. Similarly to the $\alpha = 0.5$ case, we see quantitative agreement between the hopping approach and the Butler-Volmer approach. Note that Nernstian dynamics cannot recover the correct answer, since we have introduced an asymmetric barrier and relatively slow ET kinetics in this case.

for cases where the 1D MH model agrees with the 2D model, for four different coupling strengths and two different reorganization energies. In the case of moderate reorganization energies (figure 3.6), all three methods (1D, 1D MH, and 2D) give the same results for large enough Γ, but as λ_0 increases the agreement between the 1D model and the 1D MH/2D model decreases (figure 3.7).

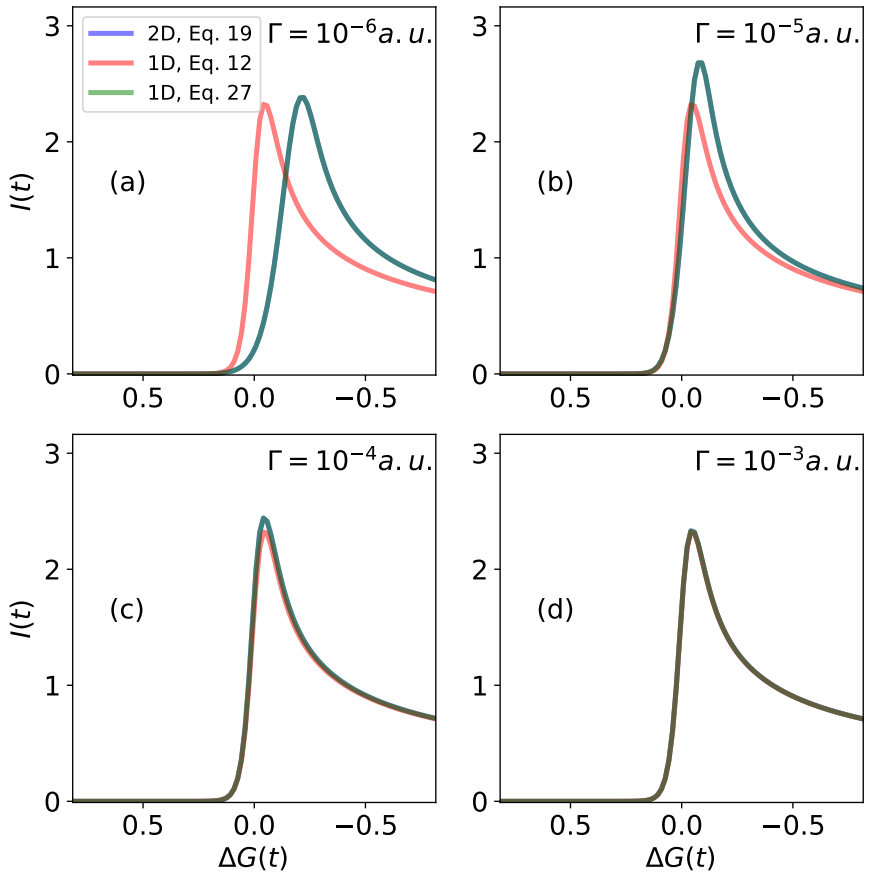

Figure 3.6: Linear sweep voltammograms for simulations where the 1D MH model (equation 3.27) and full 2D model (equation 3.19) agree, with an intermediate reorganization energy. $\Delta G_i = 0.816$ V, $\Delta G_f = -0.816$ V, $D = 5.5 \cdot 10^{-4}$ cm^2/sec, $\omega = 1.03 \cdot 10^{13}$ sec^{-1}, $\lambda_0 = 26.32kT$, and $\nu = 112$ V/sec for each subplot. (a) $\frac{\Gamma}{\hbar} = 1.40 \cdot 10^7$ cm/sec, (b) $\frac{\Gamma}{\hbar} = 1.40 \cdot 10^8$ cm/sec, (c) $\frac{\Gamma}{\hbar} = 1.40 \cdot 10^9$ cm/sec, (d) $\frac{\Gamma}{\hbar} = 1.40 \cdot 10^{10}$ cm/sec. These plots suggest that utilizing the 1D MH model in lieu of the 2D model is appropriate regardless of coupling strength for moderate reorganization energies, although at lower coupling strengths the regular 1D model (equation 3.12) fails and does not agree with the 2D model. Note that the green and blue traces representing the 1D MH and 2D models, respectively, seem indistinguishable due to the quantitative agreement between the two methods.

The regime under which the 1D, the 1D MH and 2D models all agree can be considered the case where the dynamics are mass transfer limited, i.e. the dynamics along the x coordinate are rate limiting. By contrast, the high reorganization energy/low coupling regime can be understood as the case where the dynamics are limited by motion along the solvent reorganization coordinate ζ. Nevertheless, from the fact that the 1D MH model always

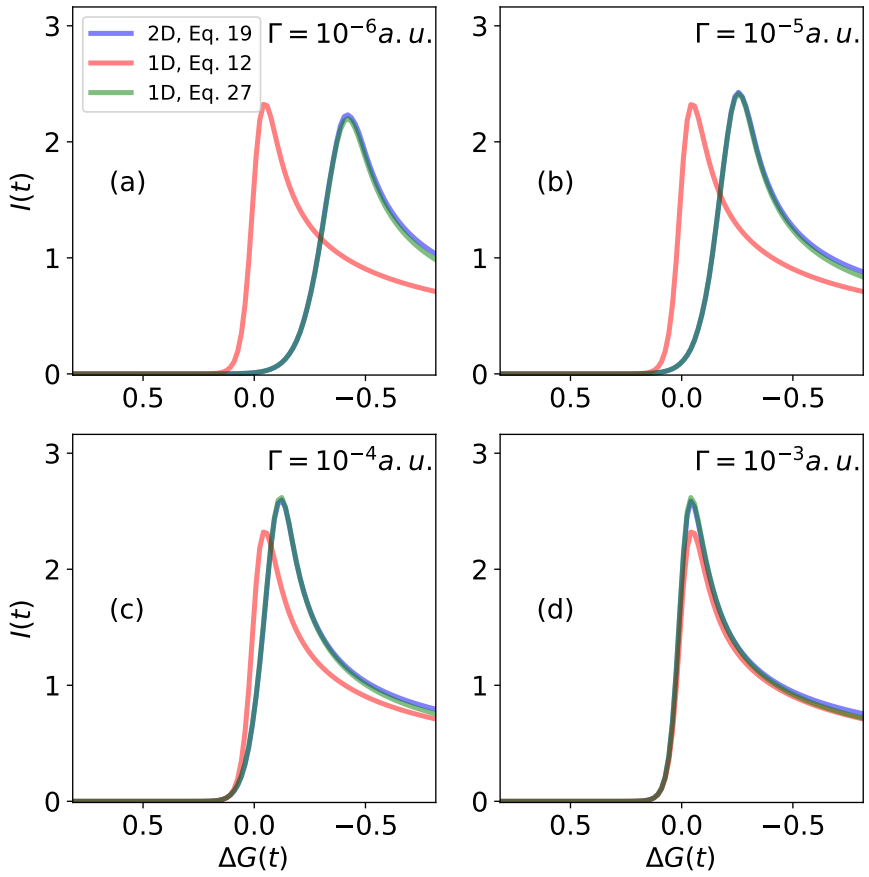

Figure 3.7: Linear sweep voltammograms for simulations where the 1D MH model (equation 3.27) and full 2D model (equation 3.19) agree, with a moderately large reorganization energy. $\Delta G_i = 0.816$ V, $\Delta G_f = -0.816$ V, $D = 5.5 \cdot 10^{-4}$ cm^2/sec, $\omega = 1.24 \cdot 10^{13}$ sec^{-1}, $\lambda_0 = 37.89kT$, and $\nu = 112$ V/sec for each subplot. (a) $\frac{\Gamma}{\hbar} = 1.40 \cdot 10^7$ cm/sec, (b) $\frac{\Gamma}{\hbar} = 1.40 \cdot 10^8$ cm/sec, (c) $\frac{\Gamma}{\hbar} = 1.40 \cdot 10^9$ cm/sec, (d) $\frac{\Gamma}{\hbar} = 1.40 \cdot 10^{10}$ cm/sec. These plots suggest that utilizing the 1D MH model in lieu of the 2D model is appropriate regardless of coupling strength for large reorganization energies. Again, as in figure 3.6, the regular 1D model is valid only when the coupling strength is large ($\frac{\Gamma}{\hbar} > \omega$).

recaptures the 2D results, it appears the 1D MH model may be adequate for capturing the dynamics of electrochemical systems in all cases. And yet, there should be instances where the average hopping rate of the 1D MH model should not be adequate for modeling the full dynamics of the 2D system. Let us now address this hypothesis.

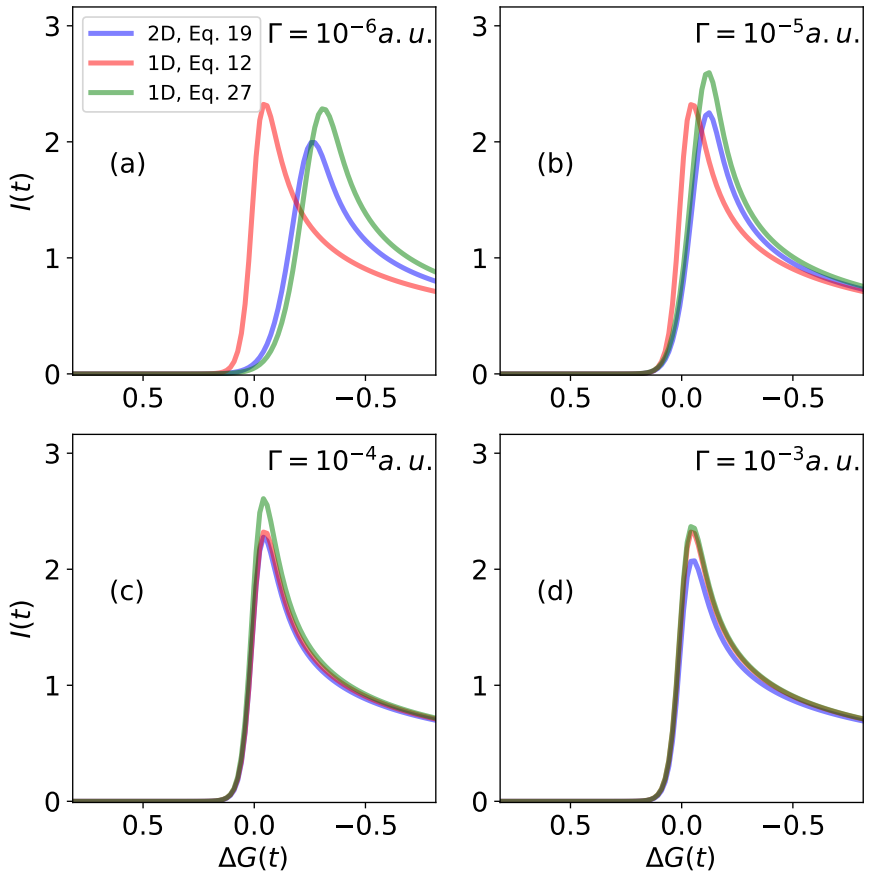

Figure 3.8: Linear sweep voltammograms for simulations where the 1D MH model (equation 3.27) and full 2D model (equation 3.19) do not agree, with $\zeta_A^0 = -5.82$ Å and $\zeta_A^\infty = -5.29$ Å in equation 3.39. $\Delta G_i = 0.816$ V, $\Delta G_f = -0.816$ V, $\sigma = \frac{10}{dx^2}$, $D = 5.5 \cdot 10^{-4}$ cm^2/sec, $\omega = 1.03 \cdot 10^{13}$ sec^{-1}, $\lambda_0 = 29.01kT$, and $\nu = 112$ V/sec for each subplot. (a) $\frac{\Gamma}{\hbar} = 1.40 \cdot 10^7$ cm/sec, (b) $\frac{\Gamma}{\hbar} = 1.40 \cdot 10^8$ cm/sec, (c) $\frac{\Gamma}{\hbar} = 1.40 \cdot 10^9$ cm/sec, (d) $\frac{\Gamma}{\hbar} = 1.40 \cdot 10^{10}$ cm/sec. By shifting ζ_A in the 2D model, and breaking separability of x and ζ in the Hamiltonian, we see that the 1D MH and 2D models can yield somewhat different results.

3.3.3. Cases where 2D and 1D MH don't agree

In order to construct a situation where the 1D MH and 2D models differ, let us choose non-separable PESs, where ζ and x are entangled. Since the 1D MH model simulates dynamics only in x, we suspect that entanglement of x and ζ should give rise to different results compared to the 2D model. To do this, instead of using $\zeta_A(x) = \zeta_A^0$ (in equation 3.18) as a

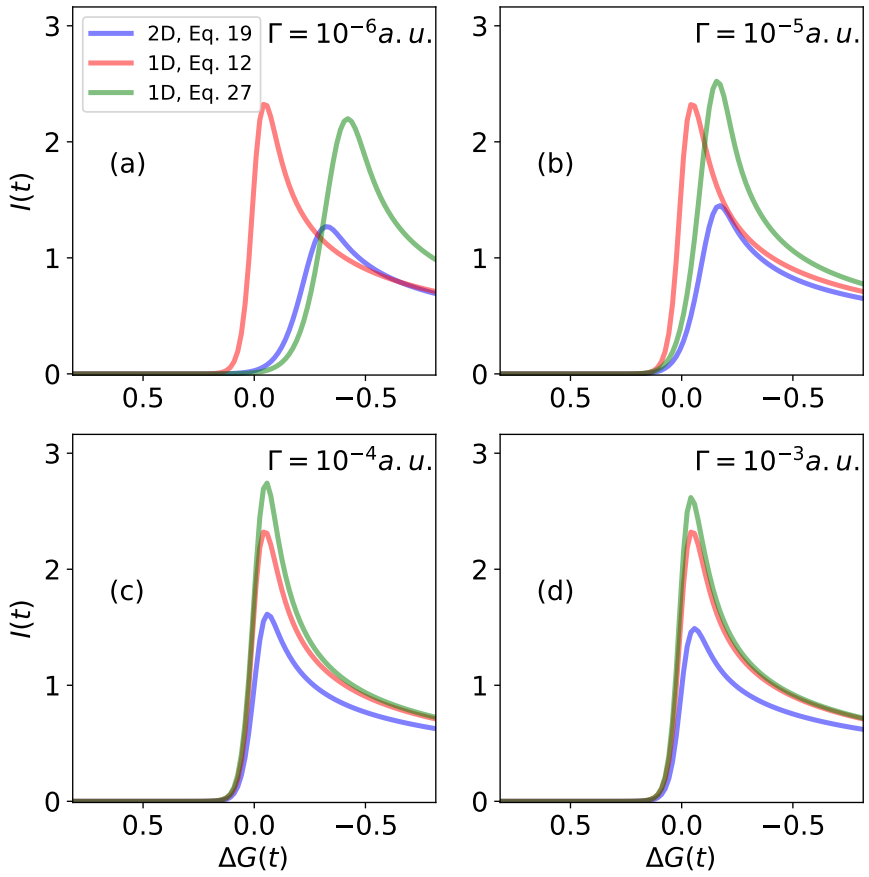

Figure 3.9: Linear sweep voltammograms for simulations where the 1D MH model (equation 3.27) and full 2D model (equation 3.19) do not agree at all, with $\zeta_A^0 = -6.35$ Å and $\zeta_A^\infty = -5.29$ Å in equation 3.39. $\Delta G_i = 0.816$ V, $\Delta G_f = -0.816$ V, $\sigma = \frac{10}{dx^2}$, $D = 5.5 \cdot 10^{-4}$ cm^2/sec, $\omega = 1.03 \cdot 10^{13}$ sec^{-1}, $\lambda_0 = 31.84kT$, and $\nu = 112$ V/sec for each subplot. (a) $\frac{\Gamma}{\hbar} = 1.40 \cdot 10^7$ cm/sec, (b) $\frac{\Gamma}{\hbar} = 1.40 \cdot 10^8$ cm/sec, (c) $\frac{\Gamma}{\hbar} = 1.40 \cdot 10^9$ cm/sec, (d) $\frac{\Gamma}{\hbar} = 1.40 \cdot 10^{10}$ cm/sec. By shifting ζ_A even more at $x = 0$, we see a complete breakdown of the 1D MH model as far as replicating the 2D model results.

constant value, we choose the functional form

$$\zeta_A(x) = (\zeta_A^0 - \zeta_A^\infty)e^{-\sigma x^2} + \zeta_A^\infty, \quad \sigma \gg \frac{1}{(dx)^2}. \tag{3.39}$$

This creates a situation where the diabat well minimum for species A takes on the value ζ_A^0 at $x = 0$ and the value ζ_A^∞ for all other x. The switch off occurs over a length scale much smaller than the grid spacing dx. Consider now a situation where $\zeta_A^\infty = -5.29$ Å for all x

values except at the electrode surface. When species A approaches the metal from $x > 0$, necessarily there must be additional relaxation as the solute concentration c_A adjusts to the new surface at $x = 0$. Moreover, this adjustment cannot be measured by a simple difference in reorganization energy at $x = 0$. In such cases, the solute concentrations c_A and c_B need not relax faster than the timescales k_f and k_b.

Plotted in figures 3.8 and 3.9 are linear sweep voltammograms for different ζ_A positions at $x = 0$ for four different coupling strengths. While the difference between the 1D MH and 2D models is modest in figure 3.8 ($\zeta_A(x = 0) = -5.82$ Å), the difference becomes readily apparent in figure 3.9 ($\zeta_A(x = 0) = -6.35$ Å). Effectively, we find that the 1D MH model is adequate for situations where the two dimensions are separable, but the 1D MH model fails when separability is no longer guaranteed. Now, one may well question whether the data in figures 3.8 and 3.9 is anomalous and caused by a discontinuous PES. To that end, in Appendix II we study smaller σ values for $\zeta_A(x)$ and investigate model Hamiltonians that smoothly bridge the gap between separable and inseparable. We find that, even with smooth PESs, the 1D MH model still fails without separability. In the future, understanding the nature of the PESs and the separability of the diffusion and solvent reorganization coordinates will be essential: after all, the reorganization energy for an ion must depend strongly on proximity to the metal surface.

3.4. Discussion

3.4.1. Electrostatic interactions

At this point, we have shown that, in many cases, 1D simulations of electrochemical voltammetry experiments are appropriate – unless there is significant non-separability between the diffusion and solvent reorganization coordinates. That being said, there is still one additional important consideration that all the simulations in this work do not account for: electrostatic interactions between charged particles (redox species and/or electrolyte ions). These effects can have a measurable effect on the dynamics and subsequent I-V curve for

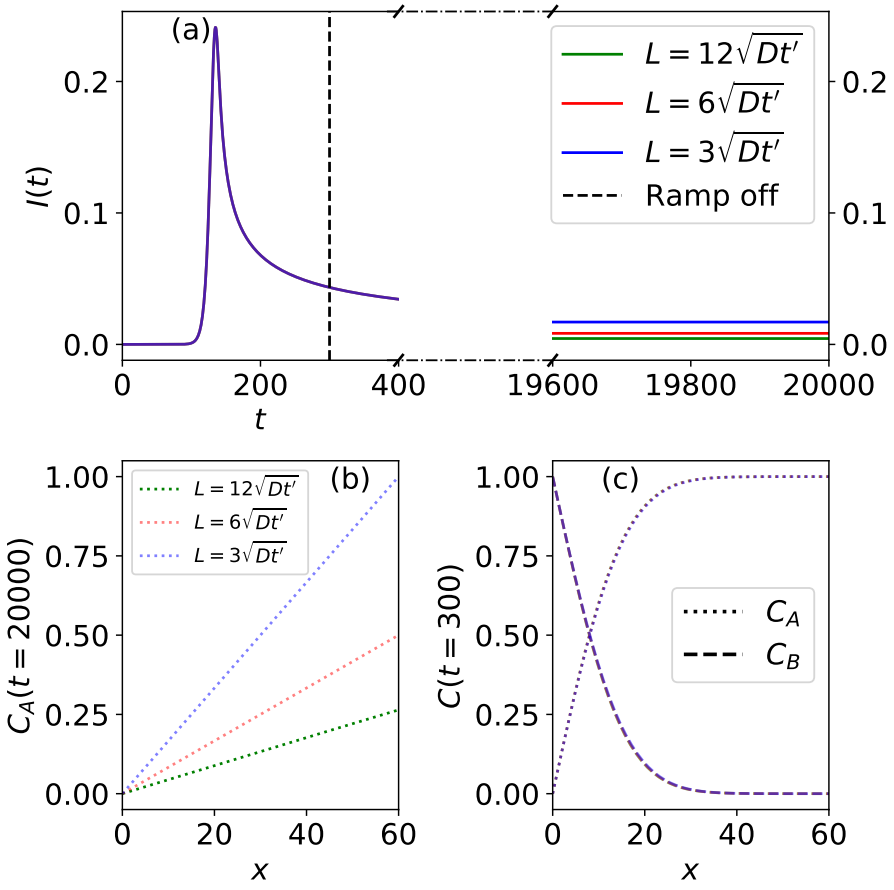

Figure 3.10: Linear sweep voltammogram and concentration profile for a simulation that is allowed to run for long times after completing the sweep, for different length grids ($x_f - x_0$). $D = 1, \nu = 0.01$, and $t' = 300$. t' is the time at which the potential ramp is turned off. (a) Linear sweep voltammograms for the case where the simulation grid length is set to $12\sqrt{Dt'}$, $6\sqrt{Dt'}$ and $3\sqrt{Dt'}$. The dotted line is the point at which the potential is no longer ramped and held at that value for the remainder of the simulation. (b) Concentration profiles for A at the end of the simulation, from $x = 0$ to $x = 3\sqrt{Dt'}$. (c) Concentration profiles for A and B at the time at which the potential ramp is turned off, from $x = 0$ to $x = 3\sqrt{Dt'}$. At short times all three grid spacings provide the same concentration and current profile, but at long times begin to diverge. The effect of grid length on the outcome of these steady-state simulations suggests that accurate modeling of electrostatic interactions between particles is necessary for a complete understanding of the dynamics of these systems at long times.

a given simulation. The importance of accounting for these interactions can be ascertained by investigating the concentrations and current profile in a simulation that is allowed to run for long times after reaching the final voltage in a linear sweep experiment.

To that end, consider figure 3.10 where dx is fixed but we choose a different number of grid points. We present 1D linear sweep voltammograms using the surface hopping approach. We find that, at long times, the concentration profiles of c_A and c_B differ greatly as a function of the length of the 1D-grid, which is also detectable through a slight difference in the steady-state current between the simulations. In fact, a simple analysis shows that the steady state current using equation 3.17(a) is

$$\begin{aligned} I_{ss} &= n\mathfrak{F}AD_A^x \frac{\partial c_A^{ss}}{\partial x}|_{x=0} \\ I_{ss} &= n\mathfrak{F}AD_A^x \frac{c_A^{ss}(x=dx) - c_A^0}{dx}, \end{aligned} \tag{3.40}$$

where c_A^0 is the steady state concentration of A at the electrode surface, whose ratio is almost (but not exactly) equal to the ratio of backward and forward hopping rates,

$$\frac{c_A^0}{c_B^0} = \frac{k_b}{k_f} + \kappa = e^{\beta\Delta G} + \kappa, \tag{3.41}$$

where κ is a small number representing the deviation of the steady state concentrations at the electrode surface from the Nernstian value.

To develop an analytical expression for I_{ss}, we note that, since the diffusion constants of both A and B are equal, the flux of A and B are equal and that $c_A + c_B = c_A^{bulk} + c_B^{bulk}$ everywhere in the simulation grid. In addition, we know that the long time concentration profile of c_A and c_B must be linear (satisfying the condition $\frac{\partial c^{ss}}{\partial t} = D^x \frac{\partial^2 c^{ss}}{\partial x^2} = 0$),

$$c_A^{ss}(x) = \frac{c_A^{bulk} - c_A^0}{L_x} x + c_A^0 \tag{3.42a}$$

$$c_B^{ss}(x) = \frac{c_B^{bulk} - c_B^0}{L_x} x + c_B^0. \tag{3.42b}$$

Finally, substituting equation 3.42a into equation 3.40 yields a steady state concentration of

$$I_{ss} = \frac{n\mathfrak{F}AD_A^x(c_A^{bulk} - c_A^0)}{L_x} \approx \frac{n\mathfrak{F}AD_A^x c_A^{bulk}}{L_x} \frac{e^{-\beta\Delta G}}{1 + e^{-\beta\Delta G}}, \tag{3.43}$$

since $c_A^0 \approx c_A^{bulk} \frac{1}{1+e^{-\beta\Delta G}}$ when $c_B^{bulk} = 0$.

A similar analysis can be done using the difference in forward and backward rates, equation 3.17(b), for the current:

$$\begin{aligned} I_{ss} =& n\mathfrak{F}A(k_f c_A^{ss} - k_b c_B^{ss})|_{x=0} \\ I_{ss} =& \frac{n\mathfrak{F}A\Gamma}{\hbar} e^{-\alpha\beta\Delta G}(c_A^0 - c_B^0 e^{\beta\Delta G}). \end{aligned} \tag{3.44}$$

Insertion of equation 3.41 for c_A^0 into 3.44 (and assuming $c_B^0 \approx c_A^{bulk} \frac{e^{-\beta\Delta G}}{1+e^{-\beta\Delta G}}$) yields

$$\begin{aligned} I_{ss} =& \frac{n\mathfrak{F}A\Gamma}{\hbar} e^{-\alpha\beta\Delta G}(c_B^0(e^{\beta\Delta G} + \kappa) - c_B^0 e^{\beta\Delta G}) \\ I_{ss} =& \frac{n\mathfrak{F}A\Gamma}{\hbar} e^{-\alpha\beta\Delta G}\kappa c_B^0 \approx \frac{n\mathfrak{F}A\Gamma}{\hbar} e^{-\alpha\beta\Delta G}\kappa c_A^{bulk} \frac{e^{-\beta\Delta G}}{1+e^{-\beta\Delta G}}. \end{aligned} \tag{3.45}$$

Comparison of equations 3.43 and 3.45 shows that $\kappa = \frac{\hbar D_x e^{\alpha\beta\Delta G}}{\Gamma L_x}$ for the case where $c_B^{bulk} = 0$, such that $c_B^0 = c_A^{bulk} - c_A^0$.

Figure 3.10 and equation 3.43 demonstrate that, in the long time limit, where mass diffusion is rate-limiting, the steady-state current is actually independent of coupling strength[93]. That being said, figure 3.10 and equation 3.43 also show a fundamental artifact of all electrochemical simulations using equations 3.17 and 3.26; steady state current should not depend on the choice of grid. The problem of grid length has been previously recognized for unequally spaced grids[94,95,96], and the general boundary flux problem is known to have a simulation box size dependence[97,98,99]. Looking forward, our belief is that an accurate treatment of electrostatic interactions in simulations should mitigate the aberrant behavior shown in figure 3.10, such that the steady state solution for $c_A(x)$ and $c_B(x)$ will not necessarily be linear between 0 and L (equation 3.42), and our modeling should be more accurate at long times. Including these electrostatic interactions within the surface hopping framework will be the focus of ongoing work.

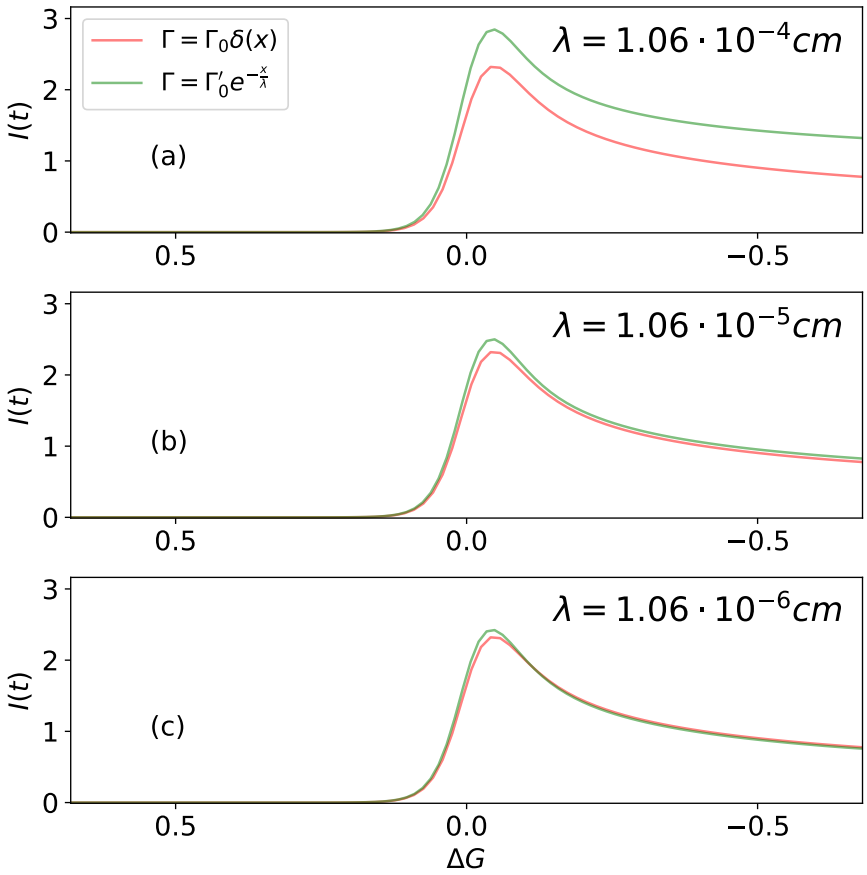

Figure 3.11: Linear sweep voltammograms for simulations with two different types of x dependence for Γ, $\Gamma(x) = \Gamma_0' e^{-\lambda x}$ (equation 3.46), $\Gamma(x) = \Gamma_0 \delta(x)$ (equation 3.12), and we fix $\Gamma_0 = \frac{\Gamma_0'}{\lambda}$. $\Delta G_i = 0.816$ V, $\Delta G_f = -0.816$ V, $D = 5.5 \cdot 10^{-4}$ cm^2/sec, $\frac{\Gamma_0}{\hbar} = 1.40 \cdot 10^8$ cm/sec, and $\nu = 112$ V/sec for each subplot. $N_x = 500$ for the $\Gamma(x) = \Gamma_0' e^{-\frac{x}{\lambda}}$ model and $N_x = 50$ for the $\Gamma(x) = \Gamma_0 \delta(x)$ model. (a) $\lambda = 1.06 \cdot 10^{-4}$ cm, (b) $\lambda = 1.06 \cdot 10^{-5}$ cm (c) $\lambda = 1.06 \cdot 10^{-6}$ cm. The results in (a) show the case where appreciable hopping occurs past the first grid point in the more sparse simulation, illustrating the breakdown of the δ-function approximation. Overall, this data confirms how one should construct Γ_0 for a sparse grid so as to match ab initio rate constants which drop off with length $\frac{1}{\lambda}$ from the surface.

3.4.2. Coarse-graining ab initio rate constants

The final issue we would like to address in this paper is the question of how we might parameterize the rate constants k_f and k_b in equations 3.6, 3.21, and 3.28. Throughout this paper, we have assumed that Γ is equal to a certain value at $x = 0$ and zero for all other

x. Of course, in reality, Γ should vary smoothly in the x direction. Thus, how should we construct $\Gamma(x)$ in practice?

In figure 3.11, we carried out simulations using equation 3.12 but on a much denser grid ($N_x = 500$) where Γ is a smooth function of x:

$$\Gamma(x) = \Gamma_0' e^{-\frac{x}{\lambda}}. \tag{3.46}$$

In figure 3.11 we also plot electrochemical simulations with $N_x = 50$ using $\Gamma(x) = \Gamma_0 \delta(x)$, where $\Gamma_0 \equiv \Gamma_0' \lambda$. From the results shown in figure 3.11, simulations with dense or sparse grids yield equivalent answers, as long as λ is small enough such that there is no appreciable ability to hop beyond the first grid point in the more sparse simulation. Thus, altogether, the data in figure 3.11 suggests that if one can compute an ab initio reaction rate $k_f(x)$ for a species near a metal surface, one needs only to calculate

$$k_f = \int_0^\infty k_f(x) dx \tag{3.47}$$

in order to parameterize a 1D model for electrochemical dynamics ($x = 0$ represents the metal surface). We remind the reader that the final k_f value will in fact have units of $\frac{cm}{s}$ compared to the ab initio reaction rate $k_f(x)$ which has units of s^{-1}. This simple relationship in equation 3.47 opens up many avenues for future explorations.

3.5. Conclusion

In this paper we have 1) shown the equivalence of the surface hopping approach with traditional electrochemical methods and 2) quantified instances under which a 2D surface hopping model can or cannot be marginalized to a simpler 1D MH model. Regarding the latter question, we find the key consideration is one of separability: If the solvent reorganization coordinate (ζ) and the diffusion coordinate (x) are nearly separable, a 1D MH model is good enough, and when compared with a multidimensional approach, the 1D MH is far

more reliable than Butler-Volmer or Nernstian dynamics. Nevertheless, if there is no separability between ζ and x, a 2D treatment is necessary and can be easily accomplished with a multidimensional SH approach.

Looking forward, if one seeks to model I-V curves under external potentials, the new approaches presented here should be of great value. After all, current voltammetry simulation packages, such as DigiElch[100], usually assume 1D systems with predetermined rate constants, chosen as linearized Marcus rates (as one would usually associate with Butler-Volmer dynamics) or full Marcus rates (which, if calculated properly, should come from averaging over solvent fluctuations, as in equation 3.28). By contrast, our guiding principle is that the time has come to utilize modern nonadiabatic dynamics algorithms to study electrochemical ET for arbitrary PESs. Using the simple analysis in the discussion section, our hope is that, in the near future, we will be able to simulate unknown mechanistic pathways for unexplained chemical systems, with realistic parameters taken from ab initio DFT studies.

3.6. Acknowledgments

We thank Abe Nitzan, Alexander Soudackov, and Adam Willard for very helpful conversations. This material is based upon work supported by the Air Force Office of Scientific Research (AFOSR) under award number FA9550-18-1-0420.

3.7. Appendix I: Stencil details for 2D simulations

When simulating 2D voltammetry experiments using the diagonalized Fokker-Planck operator, one requires a high order of accuracy for approximating the second derivative calculation with respect to ζ. To achieve convergent results using this approach, a higher order second derivative stencil was utilized. Specifically, we used a centered difference, 17-stencil, which is accurate to sixteenth order with respect to the grid spacing in ζ, $\mathcal{O}(d\zeta^{16})$. For calculating the derivative at grid point ζ_i the stencil contains the points $[\zeta_i - 8d\zeta, \zeta_i + 8d\zeta]$, with weights calculated by elimination of lower order error terms using the Taylor expan-

sions of $[\zeta_i - 8d\zeta, \zeta_i + 8d\zeta]$[101]. For the x-direction, we used a simple 3-stencil with points $[x_i - dx, x_i, x_i + dx]$ for points x_i.

3.8. Appendix II: The transition from a separable to a nonseparable Hamiltonian

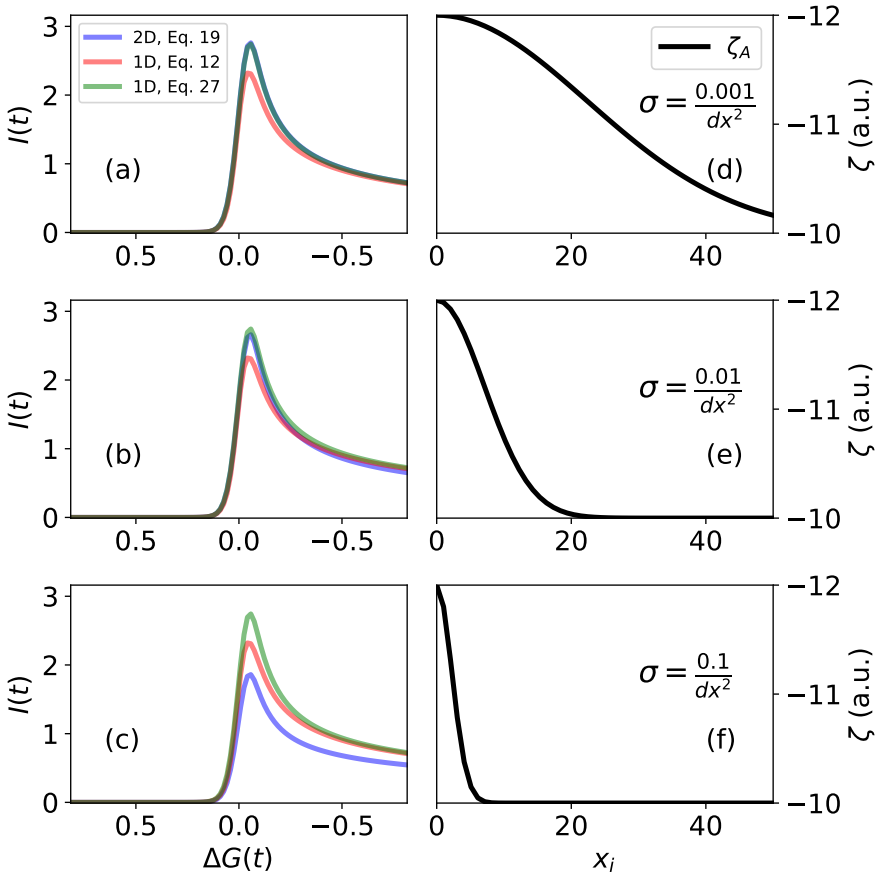

Figure 3.12: (left) Linear sweep voltammograms and (right) ζ_A positions as a function of x for different σ values in $\zeta_A(x)$ (see equation 3.39). $\Delta G_i = 0.816$ V, $\Delta G_f = -0.816$ V, $\zeta_A^0 = -6.35$ Å (-12 a.u.), $\zeta_A^\infty = -5.29$ Å (-10 a.u.), $D = 5.5 \cdot 10^{-4}$ cm^2/sec, $\omega = 1.03 \cdot 10^{13}$ sec^{-1}, $\lambda_0 = 31.84kT$, $\frac{\Gamma}{\hbar} = 1.40 \cdot 10^9$ cm/sec, and $\nu = 112$ V/sec for each subplot. (a) & (d) $\sigma = \frac{0.001}{dx^2}$, (b) & (e) $\sigma = \frac{0.01}{dx^2}$, (c) & (f) $\sigma = \frac{0.1}{dx^2}$. For small σ values, where ζ_A depends slowly on x and motion in x and ζ is largely separable, we see quantitative agreement between the 1D MH and 2D models. However, for large σ values, where there is no separability, the 1D MH and 2D models do not agree.

In figures 3.8 and 3.9 we plot results for the case that $\zeta_A(x) \approx \zeta_A^0$ at $x = 0$ and $\zeta_A(x) \approx \zeta_A^\infty$

for $x \neq 0$ (see equation 3.39). In practice, this choice of $\zeta_A(x)$ corresponds to choosing a sufficiently large value of σ for the analytical expression, $\zeta_A(x) = (\zeta_A^0 - \zeta_A^\infty)e^{-\sigma x^2} + \zeta_A^\infty$. Thus, in this limit, the x and ζ directions are far from separable: the reorganization energy (characterizing the shift of ζ as a function of charge states) depends critically and dramatically on the distance to the metal (x).

Now, that being such, one can increase separability by choosing a smaller value of σ (see equation 3.39), so that the reorganization energy changes more slowly as a function of x. To that end, in figure 3.12 we plot (on the left) linear sweep voltammograms for different σ values and (on the right) the well minimum position ζ_A as a function of the grid point in x, x_i. For small σ values, where there is little difference between $\zeta_A(x)$ values at the first few grid points, we find that the 1D MH model and the full 2D model agree quantitatively. This results confirms our intuition: the full 2D dynamics can be reduced to 1D when the x and ζ directions are close to separable.

3.9. Appendix III: Implementation of 1D BV and Nernstian boundary conditions

For Nernstian dynamics (equation 3.4) and Butler-Volmer dynamics (equations 3.5 and 3.6) there are two unknowns ($c_A(x = 0)$ and $c_B(x = 0)$) at the surface, but only one equation. As such, one additional equation is needed. To that end, it is standard[50] to use the additional constraint that the flux of species A and B are equal and opposite at the boundary,

$$J_A|_{x=0} = D_A^x \frac{\partial c_A}{\partial x}|_{x=0} = k_f c_A|_{x=0} - k_b c_B|_{x=0} \tag{3.48a}$$

$$J_B|_{x=0} = D_B^x \frac{\partial c_B}{\partial x}|_{x=0} = -k_f c_A|_{x=0} + k_b c_B|_{x=0}. \tag{3.48b}$$

Using a 2 stencil with a forward difference approximation for the spatial derivatives ($\frac{\partial c_i}{\partial x} = \frac{c_{i,1} - c_{i,0}}{dx}$ for species i), one can arrive at the following boundary values for Nernstian dynamics:

$$c_{A,0} = \frac{c_{B,1} + \frac{D_A^x}{D_B^x} c_{A,1}}{\frac{D_A^x}{D_B^x} + e^{-\beta \Delta G}} \tag{3.49a}$$

$$c_{B,0} = c_{A,0} e^{-\beta \Delta G}, \tag{3.49b}$$

and for Butler-Volmer dynamics:

$$c_{A,0} = \frac{c_{B,1} k_b dx + D_A^x c_{A,1} (1 + \frac{k_b dx}{D_B^x})}{D_A^x + dx(k_f + \frac{D_A^x}{D_B^x} k_b)} \tag{3.50a}$$

$$c_{B,0} = c_{B,1} + \frac{D_A^x}{D_B^x}(c_{A,1} - c_{A,0}). \tag{3.50b}$$

CHAPTER 4

Modeling Voltammetry Curves for Proton Coupled Electron Transfer: The Importance of Nuclear Quantum Effects

This chapter is adapted from Ref. 102.

4.1. Introduction

The importance of nuclear quantum effects on electron transfer (ET) is well known in the fields of electronic gas-phase spectroscopy[103] and electron transfer theory[104]. For example, it is well known in gas phase spectroscopy that one must account for the displacement of nuclei when measuring electronic energies, which leads to a difference between vertical and adiabatic excitation energies[105]. For electron transfer in solution, it is well known that a classical description of the event can be inadequate, and often one needs to use the full quantum version of Fermi's golden rule (FGR)[106]; there has also been an extensive discussion in the literature regarding the fact that some nuclear modes must be treated quantum mechanically while others can be treated classically when calculating ET rates[107]. Finally, the role of quantum nuclear effects within electrochemical ET has also long been appreciated, dating back to the original work of Butler[108] and has been gradually expanded upon with models by Newns[109], Schmickler[110], and others; here, even though the solvent may be classical, one cannot truly ignore the quantum mechanical features of fast vibrational motion on a surface. With this framework in mind, we would now like to study one more example of potential interest for strong nuclear quantum effects: the intersection of electrochemistry with proton-coupled electron transfer (PCET). There is now a wide-held belief that in many biological systems electronic motion is quantum mechanically coupled to or gated by quantized proton motion, and the same phenomena are likely to occur under electrochemical conditions.

Over the past 20 years, rate constant expressions and theories have been developed to model PCET in a wide variety of contexts[111,112,113,114,115,116,117]. And yet, while much

progress has been made on the theory of photoinduced PCET[118,119,120,121,122], PCET at metal oxide nanoparticle interfaces[123], and homogeneous electrochemical PCET[124,125], to our knowledge there has been little effort to theoretically model voltammetry experiments involving PCET. Specifically, little attention has been paid to nuclear quantum effects on electrochemical electron transfer in systems where the driving force is changed, such as in a linear sweep voltammetry experiment. In general, modeling electrochemistry (or PCET) alone is difficult enough, and so combining classical solvent motion with ET together with quantized proton motion over long time scales with driven boundary conditions poses a substantial difficulty—both theoretical and computational.

For our part, in order to make progress, we would like to separate classical coordinates from quantum coordinates as rigorously and as generally as possible. To that end, our approach in this paper will be to invoke a partial Wigner transformation so as to map one or more quantum coordinates to classical coordinates while leaving all other coordinates unchanged. By Wigner transforming over the classical coordinates influencing the electronic motion, and leaving the proton coordinate quantized, we will obtain a combined quantum classical Liouville equation-classical master equation (QCLE-CME) that can be solved with surface hopping (SH) dynamics. A similar QCLE-CME approach was used previously to study an electronic system with multiple orbitals and electronic states in the presence of a continuum of metallic electronic states[126]. Also, recent work has shown that diffusive electrochemical ET can be modeled with a CME and simulated with SH dynamics[49]. With this technique in mind, below we will simulate PCET subject to a linear voltammetric sweep, which will elucidate new information about the current-potential profile of a driven PCET system.

An outline of this paper is as follows. In Sec. II we present our model PCET Hamiltonian, and show how electrochemical dynamics can be characterized by a QCLE-CME and approximately solved with SH dynamics, which we henceforth refer to as SH-CME. Because many assumptions and quite a few mathematical steps are needed to derive the relevant equations, we will be (we hope) rather pedagogical and explicit in our development of the

equations. This approach will highlight how traditional ET hopping rates must be modified by Franck-Condon (i.e. overlap) factors to account for the influence of proton transfer. In Sec. III we present results for the voltammetry simulations with different PCET parameters, illustrating how nuclear quantum effects can yield quantitatively different voltammograms. In Sec. IV, we discuss the implications of our results as far as understanding electrochemical systems that undergo PCET. In Sec. V, we conclude.

4.2. Theory and Methods

4.2.1. Theoretical Developments for Coupled Nuclear-Electronic Motion at a Metal Surface

Anderson Holstein (AH) Hamiltonian for PCET

To model a PCET electrochemical system, imagine a redox-active molecule coupled to a bath of nuclei, whereby the molecule can exchange an electron with a metal electrode concertedly with proton transfer. We will employ a generalized Anderson Holstein (AH) Hamiltonian of the following form:

$$H = H_s + H_b + H_c \tag{4.1a}$$

$$H_s = H_{sys} \equiv H_{mol} + H_{ph} \tag{4.1b}$$

$$H_{sys} = \underbrace{H_0 \left|\psi_0^{el}\right\rangle \left\langle\psi_0^{el}\right| + H_1 \left|\psi_1^{el}\right\rangle \left\langle\psi_1^{el}\right|}_{H_{mol}} + H_{ph} \tag{4.1c}$$

$$H_0 = \sum_{\mu} U_0^{\mu}(x,\zeta) \left|\mu\right\rangle \left\langle\mu\right| \tag{4.1d}$$

$$H_1 = \sum_{\mu'} U_1^{\mu'}(x,\zeta) \left|\mu'\right\rangle \left\langle\mu'\right| \tag{4.1e}$$

$$H_{ph} = \sum_{\alpha} \left[\tfrac{1}{2}\left(\tfrac{\Pi_\alpha^2}{m_\alpha} + m_\alpha\omega_\alpha^2\left(\kappa_\alpha - \tfrac{g_\alpha^x x}{m_\alpha\omega_\alpha^2} - \tfrac{g_\alpha^\zeta \zeta}{m_\alpha\omega_\alpha^2}\right)\right)\right] + \tfrac{\Pi_\zeta^2}{2m_\zeta} + \tfrac{\Pi_x^2}{2m_x} \tag{4.1f}$$

$$H_b = H_{bath}^{el} = \sum_k \epsilon_k c_k^\dagger c_k \tag{4.1g}$$

$$H_c = H_{coup}^{e-e} = \sum_k W_k(\vec{r})(c_k^\dagger d + d^\dagger c_k). \tag{4.1h}$$

Here $\vec{r} = [x, \zeta, q]$ represent three relevant nuclear coordinates: the distance of the system from the electrode (x), a solvent reorganization coordinate (ζ), and a proton vibrational coordinate (q). The relevant momenta corresponding to those coordinates are Π_x, Π_ζ, and Π_q, respectively. $\left|\psi_0^{el}\right\rangle$ and $\left|\psi_1^{el}\right\rangle$ refer to electronic states of the redox active molecule, where the impurity orbital d is unoccupied or occupied, respectively. $\{|\mu\rangle\}$ and $\{|\mu'\rangle\}$ refer to a complete basis of proton vibrational states for electronic states ψ_0^{el} and ψ_1^{el} respectively (for future reference). The collection of solvent nuclei is indexed by α, and has position and momentum κ_α and Π_α, respectively, with coupling to the electronic impurity given by g_α. μ and μ' represent a given proton vibrational state when the redox molecule is uncharged and charged, respectively. H_0 and H_1 represent the energy of the electronic impurity orbital d in the unoccupied and occupied states, respectively, and the bath of metallic fermions is indexed by energy ϵ_k with coupling to the impurity orbital d given by W_k.

Note that the Hamiltonian in Eq. 4.1 is written in a slightly unorthodox way. After all, the total Hamiltonian is an operator that involves x, ζ, q, k, and d indices, and it acts on the tensor product vector space $\mathcal{H}_{diff} \otimes \mathcal{H}_{solvent} \otimes \mathcal{H}_{vib} \otimes \mathcal{H}_{metal} \otimes \mathcal{H}_{el}$. Here, $\mathcal{H}$ signifies the Hilbert space of all functions, so, e.g. $\mathcal{H}_{el}$ is spanned by the electronic impurity being occupied or not ($|\psi_0\rangle$, $|\psi_1\rangle$). For instance, consider the system Hamiltonian H_s, which consists of a molecule (here, just an electronic impurity level plus a proton), and a phononic bath of solvent H_{ph}. $U_0^\mu(x, \zeta)$ is a function of the diffusion and solvent coordinates so that H_0 and H_1 are first quantized operators that act exclusively on the vector space $\mathcal{H}_{diff} \otimes \mathcal{H}_{solvent} \otimes \mathcal{H}_{vib}$. Therefore, the term $H_{mol} = H_0 \left|\psi_0^{el}\right\rangle \left\langle\psi_0^{el}\right| + H_1 \left|\psi_1^{el}\right\rangle \left\langle\psi_1^{el}\right|$ is a first quantized operator in the vector space $\mathcal{H}_{vib} \otimes \mathcal{H}_{diff} \otimes \mathcal{H}_{solvent} \otimes \mathcal{H}_{el}$, and so we must assume an implicit identity operator acting on all other coordinates. At the same time, however, the term H_{ph} is simply written in terms of a collection of solvent coordinates and momenta. H_{ph} captures interactions between the nuclear motion and the solvent (as a function of distance to the electrode) – in principle this fluctuation could also include direct interactions between the proton and solvent coordinates, though the latter are omitted below for simplicity. Lastly, note that the Hamiltonian for the electronic bath (H_{bath}^{el}) is written in second quantization

in terms of some abstract electronic coupling between the system and the bath. H_{coup}^{e-e} is also written in second quantization, and Eq. 4.1(h) assumes that the proton does not couple to the metallic states (for simplicity).

To reiterate, we have used a slightly unorthodox mixture of first and second quantized notation to express the Hamiltonian for a molecule that can approach a metal surface and exchange an electron (as coupled to proton motion)[127] . We have chosen this mixed notation as it will make all derivations below much simpler, as we will need to simplify the quantum Hamiltonian in Eq. 4.1 for any practical calculations. Nevertheless, all notation questions aside for the reader, we must now explain the key assumptions underlying the Hamiltonian in Eq. 4.1: *Assumption # 1*: no direct coupling between protonic states is mediated directly by solvent (i.e. no $U_0^{\mu\mu'}$ terms in Eq. 4.1), and *Assumption # 2*: no direct coupling between the proton and metallic electronic states (i.e. ϵ_k does not depend on q). The proton is coupled indirectly to the solvent and metal only through coupling to the molecule. Because of this choice of Hamiltonian, Eq. 4.1 can describe *transient* proton dynamics but not PT in its full generality for which direct solvent proton coupling must be allowed (in analogy to ET). That being said, if one sets $U_0^{\mu} = U_1^{\mu'}$ (so that there is no proton reorganization) Eq. 4.1 clearly does include ET. More generally, however, if $U_0^{\mu} \neq U_1^{\mu'}$, Eq. 4.1 can describe some electronic dynamics, but all long term dynamics will necessarily include proton reorganization as well. Thus, Eq. 4.1 should describe concerted PCET accurately (but not sequential ET and PT).

Redfield Perturbation Theory in the Interaction Picture

For the dynamics we are interested in studying, the quantity of interest is the reduced density matrix of the system, ρ_s, and our method for calculating ρ_s will be based on standard quantum master equation (QME) approaches[128,129]. In coordinate form, ρ_s should depend on q, the impurity orbital d, the reaction coordinate ζ, and diffusion coordinate x so that $\rho \in \mathcal{H}_{mol} \otimes \mathcal{H}_{mol}$, where $\mathcal{H}_{mol} = \mathcal{H}_{vib} \otimes \mathcal{H}_{el} \otimes \mathcal{H}_{diff} \otimes \mathcal{H}_{solvent}$.

Because these techniques are not standard in the *electrochemical* literature, and because one

must work with slightly awkward Hamiltonians, we will now present a fairly pedagogical derivation of the relevant equations. First, we begin with the exact quantum Liouville equation (QLE) for the total density matrix, ρ, in the interaction picture. Here, we partition the Hamiltonian such that H_s and H_b are easily diagonalized and H_c is the perturbation that is not easily diagonalizable.

Using the formal identity $\rho(t) = -\frac{1}{\hbar^2}\int_0^t dt'[H_c(t),[H_c(t'),\rho(t')]])$, $\rho(t)$ can be written as

$$\frac{\partial\rho(t)}{\partial t} = -\frac{i}{\hbar}[H_c,\rho(0)] - \frac{1}{\hbar^2}\int_0^t dt'[H_c(t),[H_c(t'),\rho(t')]], \tag{4.2}$$

with

$$H_c(t) \equiv e^{\frac{i(H_s+H_b)t}{\hbar}} H_c e^{\frac{-i(H_s+H_b)t}{\hbar}}. \tag{4.3}$$

Second, we make the relevant QME assumptions: *Assumption # 3a* is the assumption of weak molecule metal coupling (resulting in the Born-Markovian approximation), whereby one replaces the reduced density matrix at time t by $\rho(t) = \rho_b^{eq} \otimes \rho_s(t)$, where ρ_b^{eq} is the equilibrium density matrix of the bath and ρ_s is the reduced density matrix of the system. If one wants to go beyond this assumption in an *ad hoc* way, one can introduce broadening artificially, as in Ref. 130. We also assume (*Assumption # 3b*) that the bath correlations decay fast, so that $\int_0^t \to \int_0^\infty$. We find, after tracing over the bath states,

$$\frac{\partial\rho_s(t)}{\partial t} = -\frac{1}{\hbar^2}\int_0^\infty d\tau Tr_b[H_c(t),[H_c(t-\tau),\rho_b^{eq}\otimes\rho_s(t)]]. \tag{4.4}$$

At time τ, $H_c(\tau) = e^{\frac{i(H_b+H_s)\tau}{\hbar}} H_c(0) e^{\frac{-i(H_b+H_s)\tau}{\hbar}}$, and for our Hamiltonian, this expression reduces to

$$\begin{aligned} H_c(\tau) &= \sum_k e^{\frac{i(H_b+H_s)\tau}{\hbar}} W_k(\vec{r})(c_k^\dagger d + d^\dagger c_k) e^{-\frac{i(H_b+H_s)\tau}{\hbar}} \\ &= \sum_k e^{\frac{i\epsilon_k\tau}{\hbar}} c_k^\dagger e^{\frac{iH_s\tau}{\hbar}} W_k(\vec{r}) d e^{-\frac{iH_s\tau}{\hbar}} + e^{\frac{iH_s\tau}{\hbar}} W_k(\vec{r}) d^\dagger e^{-\frac{iH_s\tau}{\hbar}} c_k e^{\frac{-i\epsilon_k\tau}{\hbar}}. \end{aligned} \tag{4.5}$$

Note that W_k and H_s need not commute. At this point, we must unwind the double com-

mutator in Eq. 4.4. $[H_c(t),[H_c(t-\tau),\rho(t)]]$ can be broken up into 4 separate commutators,

1. $H_c(t-\tau)[H_c(t),\rho(t)]$
2. $[H_c(t),H_c(t-\tau)]\rho(t)$
3. $-\rho(t)[H_c(t),H_c(t-\tau)]$
4. $-[H_c(t),\rho(t)]H_c(t-\tau)$,

yielding four distinct products

1. $H_c(t)H_c(t-\tau)\rho(t)$
2. $-H_c(t)\rho(t)H_c(t-\tau)$
3. $\rho(t)H_c(t-\tau)H_c(t)$
4. $-H_c(t-\tau)\rho(t)H_c(t)$.

Noting that $H_c(\tau)$ can be written as the sum of two terms, this leaves eight total terms on the RHS. We start with the term # 1a, corresponding to $H_c(t)H_c(t-\tau)\rho(t)$,

$$\begin{aligned}
&Tr_b\sum_{k,k'}(e^{\frac{i\epsilon_k t}{\hbar}}e^{-\frac{i\epsilon_{k'}(t-\tau)}{\hbar}}c_k^\dagger c_k' e^{\frac{iH_s t}{\hbar}}W_k(\vec{r})de^{-\frac{iH_s t}{\hbar}}e^{\frac{iH_s(t-\tau)}{\hbar}}W_{k'}(\vec{r})d^\dagger e^{-\frac{iH_s(t-\tau)}{\hbar}})\rho_b^{eq}\otimes\rho_s(t)\\
=&\sum_k e^{\frac{i\epsilon_k\tau}{\hbar}}f(\epsilon_k)e^{\frac{iH_s t}{\hbar}}W_k(\vec{r})de^{-\frac{iH_s\tau}{\hbar}}W_k(\vec{r})d^\dagger e^{-\frac{iH_s(t-\tau)}{\hbar}}e^{\frac{iH_s t}{\hbar}}\rho_s(0)e^{-\frac{iH_s t}{\hbar}}\\
=&\sum_k e^{\frac{i\epsilon_k\tau}{\hbar}}f(\epsilon_k)e^{\frac{iH_s t}{\hbar}}W_k(\vec{r})e^{-\frac{iH_1\tau}{\hbar}}W_k(\vec{r})e^{\frac{iH_0\tau}{\hbar}}\rho_0\left|\psi_0^{el}\right\rangle\left\langle\psi_0^{el}\right|e^{-\frac{iH_s t}{\hbar}}.
\end{aligned}\tag{4.6}$$

Here we have used the identities $\rho_s(t)=e^{\frac{iH_s t}{\hbar}}\rho_s(0)e^{-\frac{iH_s t}{\hbar}}$, $Tr_b(c_k^\dagger c_k\rho_b^{eq})=f(\epsilon_k)$ (where $f(\epsilon_k)=\frac{1}{1+e^{\beta\epsilon_k}}$ is the fermi function) and $\beta=\frac{1}{k_BT}$, and

$$\rho_s(0)=\rho_0\left|\psi_0^{el}\right\rangle\left\langle\psi_0^{el}\right|+\rho_1\left|\psi_1^{el}\right\rangle\left\langle\psi_1^{el}\right|.\tag{4.7}$$

Note that $\rho_0 + \rho_1$ corresponds to one particular electronic state of the molecule, so that ρ_0 and ρ_1 are $\in \{\mathcal{H}_{vib} \otimes \mathcal{H}_{diff} \otimes \mathcal{H}_{solvent}\}$. Term #1b, corresponding to $H_c(t)H_c(t-\tau)\rho(t)$ becomes

$$\begin{aligned}
&Tr_b \sum_{k,k'} (e^{-\frac{i\epsilon_k t}{\hbar}} e^{\frac{i\epsilon_{k'}(t-\tau)}{\hbar}} c_k c_{k'}^\dagger e^{\frac{iH_s t}{\hbar}} W_k(\vec{r}) d^\dagger e^{-\frac{iH_s t}{\hbar}} e^{\frac{iH_s(t-\tau)}{\hbar}} W_{k'}(\vec{r}) d e^{-\frac{iH_s(t-\tau)}{\hbar}}) \rho_b^{eq} \otimes \rho_s(t) \\
=&\sum_k e^{-\frac{i\epsilon_k \tau}{\hbar}} (1 - f(\epsilon_k)) e^{\frac{iH_s t}{\hbar}} W_k(\vec{r}) d e^{-\frac{iH_s \tau}{\hbar}} W_k(\vec{r}) d^\dagger e^{-\frac{iH_s(t-\tau)}{\hbar}} e^{\frac{iH_s t}{\hbar}} \rho_s(0) e^{-\frac{iH_s t}{\hbar}} \\
=&\sum_k e^{-\frac{i\epsilon_k \tau}{\hbar}} (1 - f(\epsilon_k)) e^{\frac{iH_s t}{\hbar}} e^{-\frac{iH_0 \tau}{\hbar}} W_k(\vec{r}) e^{\frac{iH_1 \tau}{\hbar}} W_k(\vec{r}) \rho_1 \left|\psi_1^{el}\right\rangle \left\langle \psi_1^{el}\right| e^{-\frac{iH_s t}{\hbar}}.
\end{aligned} \tag{4.8}$$

Now, we will perform the same reduction on the remaining three terms. The second set of terms, corresponding to $H_c(t)\rho(t)H_c(t-\tau)$, are

Term # 2a:

$$\begin{aligned}
&Tr_b \sum_{k,k'} e^{\frac{i\epsilon_k t}{\hbar}} e^{-\frac{i\epsilon_{k'}(t-\tau)}{\hbar}} (c_k^\dagger e^{\frac{iH_s t}{\hbar}} W_k(\vec{r}) d e^{-\frac{iH_s t}{\hbar}}) (\rho_b^{eq} \otimes \rho_s(t)) (c_{k'} e^{\frac{iH_s(t-\tau)}{\hbar}} W_{k'}(\vec{r}) d^\dagger e^{-\frac{iH_s(t-\tau)}{\hbar}}) \\
=&\sum_k e^{\frac{i\epsilon_k \tau}{\hbar}} (1 - f(\epsilon_k)) e^{\frac{iH_s t}{\hbar}} W_k(\vec{r}) d \rho_s(0) e^{-\frac{iH_s \tau}{\hbar}} W_k(\vec{r}) d^\dagger e^{-\frac{iH_s(t-\tau)}{\hbar}} \\
=&\sum_k e^{\frac{i\epsilon_k \tau}{\hbar}} (1 - f(\epsilon_k)) e^{\frac{iH_s t}{\hbar}} W_k(\vec{r}) \rho_1 \left|\psi_0^{el}\right\rangle \left\langle \psi_0^{el}\right| e^{-\frac{iH_1 \tau}{\hbar}} W_k(\vec{r}) e^{\frac{iH_0 \tau}{\hbar}} e^{-\frac{iH_s t}{\hbar}},
\end{aligned} \tag{4.9}$$

Term # 2b:

$$\begin{aligned}
&Tr_b \sum_{k,k'} e^{-\frac{i\epsilon_k t}{\hbar}} e^{\frac{i\epsilon_{k'}(t-\tau)}{\hbar}} (c_k e^{\frac{iH_s t}{\hbar}} W_k(\vec{r}) d^\dagger e^{-\frac{iH_s t}{\hbar}}) (\rho_b^{eq} \otimes \rho_s(t)) (c_{k'}^\dagger e^{\frac{iH_s(t-\tau)}{\hbar}} W_{k'}(\vec{r}) d e^{-\frac{iH_s(t-\tau)}{\hbar}}) \\
=&\sum_k e^{-\frac{i\epsilon_k \tau}{\hbar}} f(\epsilon_k) e^{\frac{iH_s t}{\hbar}} W_k(\vec{r}) d^\dagger \rho_s(0) e^{-\frac{iH_s \tau}{\hbar}} W_k(\vec{r}) d e^{-\frac{iH_s(t-\tau)}{\hbar}} \\
=&\sum_k e^{-\frac{i\epsilon_k \tau}{\hbar}} f(\epsilon_k) e^{\frac{iH_s t}{\hbar}} W_k(\vec{r}) \rho_0 \left|\psi_1^{el}\right\rangle \left\langle \psi_1^{el}\right| e^{-\frac{iH_0 \tau}{\hbar}} W_k(\vec{r}) e^{\frac{iH_1 \tau}{\hbar}} e^{-\frac{iH_s t}{\hbar}}.
\end{aligned} \tag{4.10}$$

The third set of terms, corresponding to $\rho(t)H_c(t-\tau)H_c(t)$, becomes

Term # 3a:

$$
\begin{aligned}
&Tr_b \sum_{k,k'} e^{-\frac{i\epsilon_k(t-\tau)}{\hbar}} e^{\frac{i\epsilon_{k'}t}{\hbar}} (\rho_b^{eq} \otimes \rho_s(t))(c_k e^{\frac{iH_s(t-\tau)}{\hbar}} W_k(\vec{r}) d^\dagger e^{-\frac{iH_s(t-\tau)}{\hbar}})(c_{k'}^\dagger e^{\frac{iH_s t}{\hbar}} W_{k'}(\vec{r}) d e^{-\frac{iH_s t}{\hbar}}) \\
=&\sum_k e^{\frac{i\epsilon_k\tau}{\hbar}}(1-f(\epsilon_k)) e^{\frac{iH_s t}{\hbar}} \rho_s(0) e^{-\frac{iH_s\tau}{\hbar}} W_k(\vec{r}) d^\dagger e^{\frac{iH_s\tau}{\hbar}} W_k(\vec{r}) d e^{-\frac{iH_s t}{\hbar}} \\
=&\sum_k e^{\frac{i\epsilon_k\tau}{\hbar}}(1-f(\epsilon_k)) e^{\frac{iH_s t}{\hbar}} \rho_1 \left|\psi_1^{el}\right\rangle \left\langle \psi_1^{el}\right| e^{-\frac{iH_1\tau}{\hbar}} W_k(\vec{r}) e^{\frac{iH_0\tau}{\hbar}} W_k(\vec{r}) e^{-\frac{iH_s t}{\hbar}},
\end{aligned}
\tag{4.11}
$$

Term # 3b:

$$
\begin{aligned}
&Tr_b \sum_{k,k'} e^{\frac{i\epsilon_k(t-\tau)}{\hbar}} e^{-\frac{i\epsilon_{k'}t}{\hbar}} (\rho_b^{eq} \otimes \rho_s(t))(c_k^\dagger e^{\frac{iH_s(t-\tau)}{\hbar}} W_k(\vec{r}) d e^{-\frac{iH_s(t-\tau)}{\hbar}})(c_{k'} e^{\frac{iH_s t}{\hbar}} W_{k'}(\vec{r}) d^\dagger e^{-\frac{iH_s t}{\hbar}}) \\
=&\sum_k e^{-\frac{i\epsilon_k\tau}{\hbar}} f(\epsilon_k) e^{\frac{iH_s t}{\hbar}} \rho_s(0) e^{-\frac{iH_s\tau}{\hbar}} W_k(\vec{r}) d e^{\frac{iH_s\tau}{\hbar}} W_k(\vec{r}) d^\dagger e^{-\frac{iH_s t}{\hbar}} \\
=&\sum_k e^{-\frac{i\epsilon_k\tau}{\hbar}} f(\epsilon_k) e^{\frac{iH_s t}{\hbar}} \rho_0 \left|\psi_0^{el}\right\rangle \left\langle \psi_0^{el}\right| e^{-\frac{iH_0\tau}{\hbar}} W_k(\vec{r}) e^{\frac{iH_1\tau}{\hbar}} W_k(\vec{r}) e^{-\frac{iH_s t}{\hbar}}.
\end{aligned}
\tag{4.12}
$$

Finally, the fourth set of term $H_c(t-\tau)\rho(t)H_c(t)$ yields

Term # 4a:

$$
\begin{aligned}
&Tr_b \sum_{k,k'} e^{\frac{i\epsilon_k(t-\tau)}{\hbar}} e^{-\frac{i\epsilon_{k'}t}{\hbar}} (c_k^\dagger e^{\frac{iH_s(t-\tau)}{\hbar}} W_k(\vec{r}) d e^{-\frac{iH_s(t-\tau)}{\hbar}})(\rho_b^{eq} \otimes \rho_s(t))(c_{k'} e^{\frac{iH_s t}{\hbar}} W_{k'}(\vec{r}) d^\dagger e^{-\frac{iH_s t}{\hbar}}) \\
=&\sum_k e^{-\frac{i\epsilon_k\tau}{\hbar}}(1-f(\epsilon_k)) e^{\frac{iH_s(t-\tau)}{\hbar}} W_k(\vec{r}) d e^{\frac{iH_s\tau}{\hbar}} \rho_s(0) W_k(\vec{r}) d^\dagger e^{-\frac{iH_s t}{\hbar}} \\
=&\sum_k e^{-\frac{i\epsilon_k\tau}{\hbar}}(1-f(\epsilon_k)) e^{\frac{iH_s t}{\hbar}} e^{-\frac{iH_0\tau}{\hbar}} W_k(\vec{r}) e^{\frac{iH_1\tau}{\hbar}} \rho_1 \left|\psi_0^{el}\right\rangle \left\langle \psi_0^{el}\right| W_k(\vec{r}) e^{-\frac{iH_s t}{\hbar}},
\end{aligned}
\tag{4.13}
$$

Term # 4b:

$$
\begin{aligned}
&Tr_b \sum_{k,k'} e^{-\frac{i\epsilon_k(t-\tau)}{\hbar}} e^{\frac{i\epsilon_{k'}t}{\hbar}} (c_k e^{\frac{iH_s(t-\tau)}{\hbar}} W_k(\vec{r}) d^\dagger e^{-\frac{iH_s(t-\tau)}{\hbar}}) (\rho_b^{eq} \otimes \rho_s(t)) (c_{k'}^\dagger e^{\frac{iH_s t}{\hbar}} W_{k'}(\vec{r}) d e^{-\frac{iH_s t}{\hbar}}) \\
&= \sum_k e^{\frac{i\epsilon_k \tau}{\hbar}} f(\epsilon_k) e^{\frac{iH_s(t-\tau)}{\hbar}} W_k(\vec{r}) d^\dagger e^{\frac{iH_s\tau}{\hbar}} \rho_s(0) W_k(\vec{r}) d e^{-\frac{iH_s t}{\hbar}} \\
&= \sum_k e^{\frac{i\epsilon_k \tau}{\hbar}} f(\epsilon_k) e^{\frac{iH_s t}{\hbar}} e^{-\frac{iH_1\tau}{\hbar}} W_k(\vec{r}) e^{\frac{iH_0\tau}{\hbar}} \rho_0 \left|\psi_1^{el}\right\rangle \left\langle \psi_1^{el}\right| W_k(\vec{r}) e^{-\frac{iH_s t}{\hbar}}.
\end{aligned}
\tag{4.14}
$$

This completes our derivation of the relevant equations in the interaction picture.

Redfield Perturbation Theory in the Schrödinger Picture

By plugging all eight terms from Eqs. 4.6 - 4.14 into Eq. 4.4, and converting from the interaction picture to the Schrödinger picture, we can recover two equations for the time evolution of ρ_0 and ρ_1:

$$
\begin{aligned}
\frac{\partial \rho_0}{\partial t} = -\frac{i}{\hbar}[H_0, \rho_0] - \sum_k \frac{1}{\hbar^2} \int_0^\infty d\tau (& e^{-\frac{i\epsilon_k\tau}{\hbar}} f(\epsilon_k) \rho_0 e^{-\frac{iH_0\tau}{\hbar}} W_k(\vec{r}) e^{\frac{iH_1\tau}{\hbar}} W_k(\vec{r}) \\
& - e^{-\frac{i\epsilon_k\tau}{\hbar}} (1 - f(\epsilon_k)) e^{-\frac{iH_0\tau}{\hbar}} W_k(\vec{r}) e^{\frac{iH_1\tau}{\hbar}} \rho_1 W_k(\vec{r}) \\
& - e^{\frac{i\epsilon_k\tau}{\hbar}} (1 - f(\epsilon_k)) W_k(\vec{r}) \rho_1 e^{-\frac{iH_1\tau}{\hbar}} W_k(\vec{r}) e^{\frac{iH_0\tau}{\hbar}} \\
& + e^{\frac{i\epsilon_k\tau}{\hbar}} f(\epsilon_k) W_k(\vec{r}) e^{-\frac{iH_1\tau}{\hbar}} W_k(\vec{r}) e^{\frac{iH_0\tau}{\hbar}} \rho_0)
\end{aligned}
\tag{4.15}
$$

and

$$
\begin{aligned}
\frac{\partial \rho_1}{\partial t} = -\frac{i}{\hbar}[H_1, \rho_1] - \sum_k \frac{1}{\hbar^2} \int_0^\infty d\tau (& e^{\frac{i\epsilon_k\tau}{\hbar}} (1 - f(\epsilon_k)) \rho_1 e^{-\frac{iH_1\tau}{\hbar}} W_k(\vec{r}) e^{\frac{iH_0\tau}{\hbar}} W_k(\vec{r}) \\
& - e^{\frac{i\epsilon_k\tau}{\hbar}} f(\epsilon_k) e^{-\frac{iH_1\tau}{\hbar}} W_k(\vec{r}) e^{\frac{iH_0\tau}{\hbar}} \rho_0 W_k(\vec{r}) \\
& - e^{-\frac{i\epsilon_k\tau}{\hbar}} f(\epsilon_k) W_k(\vec{r}) \rho_0 e^{-\frac{iH_0\tau}{\hbar}} W_k(\vec{r}) e^{\frac{iH_1\tau}{\hbar}} \\
& + e^{-\frac{i\epsilon_k\tau}{\hbar}} (1 - f(\epsilon_k)) W_k(\vec{r}) e^{-\frac{iH_0\tau}{\hbar}} W_k(\vec{r}) e^{\frac{iH_1\tau}{\hbar}} \rho_1)
\end{aligned}
\tag{4.16}
$$

These equations can be represented in the following form

$$\frac{\partial \rho}{\partial t} = -\frac{i}{\hbar}[H, \rho] - \hat{\hat{\mathfrak{L}}}\rho, \tag{4.17}$$

which is known as a "Redfield equation", or equivalently

$$\begin{aligned} \frac{\partial \rho_0}{\partial t} &= -\frac{i}{\hbar}[H_0, \rho_0] - \hat{\hat{\mathfrak{L}}}\rho_0 \\ \frac{\partial \rho_1}{\partial t} &= -\frac{i}{\hbar}[H_1, \rho_1] - \hat{\hat{\mathfrak{L}}}\rho_1, \end{aligned} \tag{4.18}$$

with ρ_s partitioned into ρ_0 and ρ_1 using Eq. 4.7. The superoperator $\hat{\hat{\mathfrak{L}}}$ is defined by its operation on ρ_0 and ρ_1,

$$\begin{aligned} \hat{\hat{\mathfrak{L}}}\rho_0 = \sum_k \frac{1}{\hbar^2} \int_0^\infty d\tau e^{\frac{i\epsilon_k \tau}{\hbar}} f(\epsilon_k) W_k(\vec{r}) e^{-\frac{iH_1\tau}{\hbar}} W_k(\vec{r}) e^{\frac{iH_0\tau}{\hbar}} \rho_0 \\ - e^{\frac{i\epsilon_k \tau}{\hbar}} (1 - f(\epsilon_k)) W_k(\vec{r}) \rho_1 e^{-\frac{iH_1\tau}{\hbar}} W_k(\vec{r}) e^{\frac{iH_0\tau}{\hbar}} + h.c. \end{aligned} \tag{4.19}$$

and

$$\begin{aligned} \hat{\hat{\mathfrak{L}}}\rho_1 = \sum_k \frac{1}{\hbar^2} \int_0^\infty d\tau e^{-\frac{i\epsilon_k \tau}{\hbar}} (1 - f(\epsilon_k)) W_k(\vec{r}) e^{-\frac{iH_0\tau}{\hbar}} W_k(\vec{r}) e^{\frac{iH_1\tau}{\hbar}} \rho_1 \\ - e^{-\frac{i\epsilon_k \tau}{\hbar}} f(\epsilon_k) W_k(\vec{r}) \rho_0 e^{-\frac{iH_0\tau}{\hbar}} W_k(\vec{r}) e^{\frac{iH_1\tau}{\hbar}} + h.c. \end{aligned} \tag{4.20}$$

where both ρ_0 and ρ_1 are combined electronic-vibrational density matrices.

A Partial Wigner Transform

Eqs. 4.18 - 4.20 are still too complicated to solve numerically given that all nuclear motion is still quantum mechanical. Thus, at this point, we perform a partial Wigner transformation on Eq. 4.18 over the coordinates (x, ζ), while leaving the proton coordinate quantized. We will depict all quantum operators A with a hat, $\hat{A}$, and a superscript ^{vib} will signify that we have Wigner transformed over everything except the proton coordinate. Thus, we will construct $\rho_0^{vib}(x, \zeta)$ and $\rho_1^{vib}(x, \zeta)$. Note that ρ_0^{vib} and ρ_1^{vib} are $\in \{\mathcal{H}_{proton}\}$, i.e. they are

density operators in the space of the quantum proton.

When taking the Wigner transform of Eq. 4.18, we will need to evaluate the Wigner transform of a product of operators. Recall that $(AB)_W = A_W e^{\frac{\hbar\Lambda}{2i}} B_W$, where Λ is the Poisson bracket operator $\overleftrightarrow{\Lambda} = \overleftarrow{\nabla}_P \cdot \overrightarrow{\nabla}_R - \overleftarrow{\nabla}_R \cdot \overrightarrow{\nabla}_P$. Then, following the standard notation of classical mechanics, let us define $\{\hat{O}_1, \hat{O}_2\} = \sum_\alpha \frac{\partial \hat{O}_1}{\partial R_\alpha}\frac{\partial \hat{O}_2}{\partial p_\alpha} - \frac{\partial \hat{O}_1}{\partial p_\alpha}\frac{\partial \hat{O}_2}{\partial R_\alpha}$ as the usual Poisson bracket. Note that, because $\hat{O}_1$ and $\hat{O}_2$ are operators, the order of the operators is critically important. Thus, $\frac{\partial \hat{O}_1}{\partial x_\alpha}\frac{\partial \hat{O}_2}{\partial p_\alpha} \neq \frac{\partial \hat{O}_1}{\partial p_\alpha}\frac{\partial \hat{O}_2}{\partial x_\alpha}$. Finally, when we calculate the Wigner transformation of the commutator $-\frac{i}{\hbar}[H_s, \rho_s]$ to first order in $\hbar$, which is a classical assumption about the diffusion (x) and solvent (ζ) coordinates (*Assumption # 4*), we find the result $-\frac{i}{\hbar}[H_s, \rho_s] = -\frac{i}{\hbar}[H_s^{vib}, \rho_s^{vib}] + \{H_s^{vib}, \rho_s^{vib}\}_a$ where $\{\hat{O}_1, \hat{O}_2\}_a = \frac{1}{2}(\{\hat{O}_1, \hat{O}_2\} - \{\hat{O}_2, \hat{O}_1\})$. We are left with the famous quantum classical Liouville equation (QCLE) for $\hat{\rho}_s^{vib}$,

$$\begin{aligned}
\frac{\partial \hat{\rho}_0^{vib}}{\partial t} &= \frac{1}{2}(\{\hat{H}_0^{vib}, \hat{\rho}_0^{vib}\} - \{\hat{\rho}_0^{vib}, \hat{H}_0^{vib}\}) - \frac{i}{\hbar}[\hat{H}_0^{vib}, \hat{\rho}_0^{vib}] - \hat{\hat{\mathfrak{L}}}^{vib}\hat{\rho}_0^{vib} \\
\frac{\partial \hat{\rho}_1^{vib}}{\partial t} &= \frac{1}{2}(\{\hat{H}_1^{vib}, \hat{\rho}_1^{vib}\} - \{\hat{\rho}_1^{vib}, \hat{H}_1^{vib}\}) - \frac{i}{\hbar}[\hat{H}_1^{vib}, \hat{\rho}_1^{vib}] - \hat{\hat{\mathfrak{L}}}^{vib}\hat{\rho}_1^{vib}.
\end{aligned} \tag{4.21}$$

One would like to assume that, just as for the QCLE[35], Eq. 4.21 is correct to order $\mathcal{O}(\hbar)$. However, in Eq. 4.21 we have implicitly made one more (fairly standard) assumption, i.e. that $(\hat{\hat{\mathfrak{L}}}\rho_s)^{vib} = \hat{\hat{\mathfrak{L}}}^{vib}\hat{\rho_s}^{vib}$[89], and so Eq. 4.21 is formally less accurate than the usual QCLE. This assumption (which effectively ignores all direct nuclear quantum effects on the transient electron transfer between metal and molecule) is largely comparable with Assumption # 4.

Lastly, at this point we will temporarily make one final assumption, *Assumption # 5*: we assume that W_k is independent of q, which will allow us to rearrange and simplify the equations for $(\hat{\hat{\mathfrak{L}}}\rho_s)^{vib}$. For a treatment of electrochemical PCET that does allow for $W_k(q)$, see Ref. 131 and Appendix III. (Note that any dependence of W_k on x, the distance from the electrode, is different from any dependence on q; for a theoretical treatment of electrochemical PCET that includes the dependence of the electronic coupling on the distance x from the electrode, see Refs. 132 and 133.) Within the framework of Assumption # 5, we can

expand $\hat{\mathfrak{L}}^{vib}\hat{\rho}_0^{vib}$ in vibrational states μ,ν, (using Eqs. 4.19 and 4.20).

$$\begin{aligned}\langle\mu|\,\hat{\mathfrak{L}}^{vib}\hat{\rho}_0^{vib}\,|\nu\rangle = -\sum_{k,\mu',\nu',\xi}\frac{|W_k|^2}{\hbar^2}\int_0^\infty d\tau(&e^{-\frac{i\epsilon_k\tau}{\hbar}}f(\epsilon_k)\,\langle\mu|\,\rho_0\,|\xi\rangle\,\langle\xi|\,e^{-\frac{iH_0\tau}{\hbar}}\,|\mu'\rangle\,\langle\mu'|\,e^{\frac{iH_1\tau}{\hbar}}\,|\nu'\rangle\\ &-e^{-\frac{i\epsilon_k\tau}{\hbar}}(1-f(\epsilon_k))\,\langle\mu|\,e^{-\frac{iH_0\tau}{\hbar}}\,|\mu'\rangle\,\langle\mu'|\,e^{\frac{iH_1\tau}{\hbar}}\rho_1\,|\nu'\rangle\,\langle\nu'|\nu\rangle\\ &-e^{\frac{i\epsilon_k\tau}{\hbar}}(1-f(\epsilon_k))\,\langle\mu|\mu'\rangle\,\langle\mu'|\,\rho_1\,|\nu'\rangle\,\langle\nu'|\,e^{-\frac{iH_1\tau}{\hbar}}e^{\frac{iH_0\tau}{\hbar}}\,|\nu\rangle\\ &+e^{\frac{i\epsilon_k\tau}{\hbar}}f(\epsilon_k)\,\langle\mu|\mu'\rangle\,\langle\mu'|\,e^{-\frac{iH_1\tau}{\hbar}}\,|\xi\rangle\,\langle\xi|\,e^{\frac{iH_0\tau}{\hbar}}\rho_0\,|\nu\rangle)\end{aligned} \tag{4.22}$$

where primed (unprimed) Greek indices correspond to proton vibrational states in the basis of electronic state 1 (state 0). We can similarly expand $\hat{\mathfrak{L}}^{vib}\hat{\rho}_1^{vib}$ in vibrational states μ',ν' to obtain

$$\begin{aligned}\langle\mu'|\,\hat{\mathfrak{L}}^{vib}\hat{\rho}_1^{vib}\,|\nu'\rangle = -\sum_{k,\mu,\nu,\xi'}\frac{|W_k|^2}{\hbar^2}\int_0^\infty d\tau(&e^{\frac{i\epsilon_k\tau}{\hbar}}(1-f(\epsilon_k))\,\langle\mu'|\,\rho_1\,|\xi'\rangle\,\langle\xi'|\,e^{-\frac{iH_1\tau}{\hbar}}\,|\mu\rangle\,\langle\mu|\,e^{\frac{iH_0\tau}{\hbar}}\,|\nu\rangle\\ &-e^{\frac{i\epsilon_k\tau}{\hbar}}f(\epsilon_k)\,\langle\mu'|\,e^{-\frac{iH_1\tau}{\hbar}}\,|\mu\rangle\,\langle\mu|\,e^{\frac{iH_0\tau}{\hbar}}\rho_0\,|\nu\rangle\,\langle\nu|\nu'\rangle\\ &-e^{-\frac{i\epsilon_k\tau}{\hbar}}f(\epsilon_k)\,\langle\mu'|\mu\rangle\,\langle\mu|\,\rho_0\,|\nu\rangle\,\langle\nu|\,e^{-\frac{iH_0\tau}{\hbar}}e^{\frac{iH_1\tau}{\hbar}}\,|\nu'\rangle\\ &+e^{-\frac{i\epsilon_k\tau}{\hbar}}(1-f(\epsilon_k))\,\langle\mu'|\mu\rangle\,\langle\mu|\,e^{-\frac{iH_0\tau}{\hbar}}\,|\xi'\rangle\,\langle\xi'|\,e^{\frac{iH_1\tau}{\hbar}}\rho_1\,|\nu'\rangle).\end{aligned} \tag{4.23}$$

At this point, if we make the substitution $\int_0^\infty d\tau e^{\frac{i\epsilon_k\tau}{\hbar}} = \pi\delta(\epsilon_k)\hbar$, we arrive at a relatively complete expression for $\frac{\partial\rho_0^{\mu\nu}}{\partial t}$,

$$\begin{aligned}\frac{\partial\rho_0^{\mu\nu}}{\partial t} =&\frac{1}{2}\,\langle\mu|\,(\{\hat{H}_0^{vib},\hat{\rho}_0^{vib}\}-\{\hat{\rho}_0^{vib},\hat{H}_0^{vib}\})\,|\nu\rangle\\ &-\frac{i}{\hbar}(U_0^\mu-U_0^\nu)\rho_0^{\mu\nu}\\ &-\frac{\Gamma}{2\hbar}\sum_{\mu',\xi}f(U_1^{\mu'}-U_0^\xi)\,\langle\mu|\mu'\rangle\,\langle\mu'|\xi\rangle\,\rho_0^{\xi\nu}\\ &-\frac{\Gamma}{2\hbar}\sum_{\mu',\xi}\rho_0^{\mu\xi}f(U_1^{\mu'}-U_0^\xi)\,\langle\xi|\mu'\rangle\,\langle\mu'|\nu\rangle\\ &+\frac{\Gamma}{2\hbar}\sum_{\mu',\nu'}(1-f(U_1^{\nu'}-U_0^\nu))\,\langle\mu|\mu'\rangle\,\langle\nu'|\nu\rangle\,\rho_1^{\mu'\nu'}\\ &+\frac{\Gamma}{2\hbar}\sum_{\mu',\nu'}\rho_1^{\mu'\nu'}(1-f(U_1^{\mu'}-U_0^\mu))\,\langle\mu|\mu'\rangle\,\langle\nu'|\nu\rangle\,,\end{aligned} \tag{4.24}$$

and similarly for $\frac{\partial \rho_1^{\mu'\nu'}}{\partial t}$,

$$\begin{aligned}\frac{\partial \rho_1^{\mu'\nu'}}{\partial t} =& \frac{1}{2}\left\langle \mu' \right| \left(\{\hat{H}_1^{vib}, \hat{\rho}_1^{vib}\} - \{\hat{\rho}_1^{vib}, \hat{H}_1^{vib}\}\right) \left| \nu' \right\rangle \\ &- \frac{i}{\hbar}(U_1^{\mu'} - U_1^{\nu'})\rho_1^{\mu'\nu'} \\ &- \frac{\Gamma}{2\hbar}\sum_{\mu,\xi'}(1 - f(U_1^{\mu'} - U_0^{\xi}))\left\langle \mu' \right| \left. \mu \right\rangle \left\langle \mu \right| \left. \xi' \right\rangle \rho_1^{\xi'\nu'} \\ &- \frac{\Gamma}{2\hbar}\sum_{\mu,\xi'}\rho_1^{\mu'\xi'}(1 - f(U_1^{\mu'} - U_0^{\xi}))\left\langle \xi' \right| \left. \mu \right\rangle \left\langle \mu \right| \left. \nu' \right\rangle \\ &+ \frac{\Gamma}{2\hbar}\sum_{\mu,\nu} f(U_1^{\nu'} - U_0^{\nu})\left\langle \mu' \right| \left. \mu \right\rangle \left\langle \nu \right| \left. \nu' \right\rangle \rho_0^{\mu\nu} \\ &+ \frac{\Gamma}{2\hbar}\sum_{\mu,\nu}\rho_0^{\mu\nu} f(U_1^{\mu'} - U_0^{\mu})\left\langle \mu' \right| \left. \mu \right\rangle \left\langle \nu \right| \left. \nu' \right\rangle .\end{aligned} \tag{4.25}$$

Here, $\rho_0^{\mu\nu} = \langle \mu | \hat{\rho}_0^{vib} | \nu \rangle$ and $\Gamma = 2\pi \sum_k |W_k|^2 \delta(\epsilon - \epsilon_k)$ is the metal-molecule coupling in the wide-band limit that characterizes the rate with which electrons can hop between molecule and metal.

Eqs. 4.24 and 4.25 capture the coupling of electron transfer to classical solvent motion as well as to quantum mechanical proton motion. In principle, these equations can be solved using an advanced surface hopping algorithm with an unconstrained number of electrons [130].

A Secular Approximation

In practice, however, it is common to make one final secular approximation, *Assumption # 6*, whereby rapidly oscillating off-diagonal terms are neglected so that we can focus only on

the diagonal (population) terms of the density matrix. $\rho^{\mu\mu}$ then becomes

$$\begin{aligned}
\frac{\partial \rho_0^{\mu\mu}}{\partial t} &= \langle \mu | \left(\{ \hat{H}_0^{vib}, \hat{\rho}_0^{vib} \} \right) | \mu \rangle \\
&\quad - \frac{\Gamma}{\hbar} \sum_{\mu'} \left| F_{\mu \to \mu'} \right|^2 f(U_1^{\mu'} - U_0^{\mu}) \rho_0^{\mu\mu} \\
&\quad + \frac{\Gamma}{\hbar} \sum_{\mu'} \left| F_{\mu \to \mu'} \right|^2 (1 - f(U_1^{\mu'} - U_0^{\mu})) \rho_1^{\mu'\mu'} \\
\frac{\partial \rho_1^{\mu'\mu'}}{\partial t} &= \left\langle \mu' \right| \left(\{ \hat{H}_1^{vib}, \hat{\rho}_1^{vib} \} \right) \left| \mu' \right\rangle \\
&\quad + \frac{\Gamma}{\hbar} \sum_{\mu} \left| F_{\mu \to \mu'} \right|^2 f(U_1^{\mu'} - U_0^{\mu}) \rho_0^{\mu\mu} \\
&\quad - \frac{\Gamma}{\hbar} \sum_{\mu} \left| F_{\mu \to \mu'} \right|^2 (1 - f(U_1^{\mu'} - U_0^{\mu})) \rho_1^{\mu'\mu'},
\end{aligned} \tag{4.26}$$

with $F_{\mu \to \mu'}$ being the Franck-Condon factor (i.e., overlap integral) between wavefunctions μ and μ', $\langle \mu | \mu' \rangle$. In making the secular approximation, we ignore the quantum mechanical coherence of the proton coordinate, so that we lose any capacity for protonic dynamics even at short times: we focus exclusively on coupled proton-electron transfer dynamics. Nevertheless, it will turn out that solving Eq. 4.26 is already a difficult enough task; to go beyond the secular approximation requires including the off-diagonal (coherence) terms, which can be difficult with surface hopping[134].

Final Equations

In the end, for modeling electrochemical PCET, our final equations are of the simple form

$$\begin{aligned}
\frac{\partial \rho_0^{\mu}}{\partial t} &= \left(\{ H_0, \rho_0 \} \right)^{\mu} - \sum_{\mu'} (\gamma_{0 \to 1}^{\mu\mu'} \rho_0^{\mu} - \gamma_{1 \to 0}^{\mu\mu'} \rho_1^{\mu'}) \\
\frac{\partial \rho_1^{\mu'}}{\partial t} &= \left(\{ H_1, \rho_1 \} \right)^{\mu'} - \sum_{\mu} (\gamma_{1 \to 0}^{\mu\mu'} \rho_1^{\mu'} - \gamma_{0 \to 1}^{\mu\mu'} \rho_0^{\mu})
\end{aligned} \tag{4.27}$$

where the hopping rates are

$$\begin{aligned}\gamma_{0\to1}^{\mu\mu'} &= \frac{\Gamma}{\hbar} f(U_1^{\mu'} - U_0^{\mu}) \left|F_{\mu\to\mu'}\right|^2 \\ \gamma_{1\to0}^{\mu\mu'} &= \frac{\Gamma}{\hbar} (1 - f(U_1^{\mu'} - U_0^{\mu})) \left|F_{\mu\to\mu'}\right|^2.\end{aligned} \tag{4.28}$$

Electrochemical PCET is clearly a generalization of electrochemical ET. If we compare Eq. 21(a) and (b) from Ref. 49 to Eq. 4.28 above, the only difference is the inclusion of Franck-Condon (i.e. proton wavefunction overlap) factors in the hopping rates, and the fact that all energy differences are now between combined electron-proton vibronic energetic states, $U_1^{\mu'} - U_0^{\mu}$, instead of the more straightforward electronic diabatic energy difference $U_1 - U_0$. As might be expected, hops can occur from one vibrational state (in electronic state 0 or 1) to all other possible vibrational states (in the opposite electronic state). To allow for comparison to traditional eletrochemical literature definitions, we will henceforth refer to $\gamma_{0\to1}$ as k_f and $\gamma_{1\to0}$ as k_b.

Within Eqs. 4.27-4.28, all PCET dynamics follow directly from the potential energy surfaces $U_0^{\mu}(x,\zeta)$ and $U_1^{\mu}(x,\zeta)$, which will be recast as U_A^{μ} and $U_B^{\mu'}$ (μ and μ' index proton vibrational levels). This naming convention is to allow for more natural comparison to the chemical reaction occurring at the electrode:

$$\mathrm{A} + \mathrm{e}^- \underset{\mathrm{k_b}}{\overset{\mathrm{k_f}}{\rightleftharpoons}} \mathrm{B}$$

where A represents the species oxidized (uncharged) and B represents the species reduced (charged). For the model calculations below, we will now make the simplifying assumption (*Assumption # 7*) that these functions are quadratic wells over the solvent reorganization coordinate ζ, independent of x, so as to avoid a few numerical obstacles and allow for much faster calculations. In general, though, the equations can be solved with x-dependence.

Below, we will choose our PESs to be of the form:

$$U_A^{\mu}(\zeta) = \tfrac{1}{2}m\omega^2(\zeta_A - \zeta)^2 + \tilde{U}_A^{\mu} \tag{4.29a}$$

$$U_B^{\mu'}(\zeta) = \tfrac{1}{2}m\omega^2(\zeta_B - \zeta)^2 + \Delta G + \tilde{U}_B^{\mu'} \tag{4.29b}$$

$$E^{\mu,\mu'}(\zeta) = U_B^{\mu'} - U_A^{\mu} = \tfrac{1}{2}m\omega^2(\zeta_B^2 - \zeta_A^2 - 2(\zeta_B - \zeta_A)\zeta) + \Delta G + (\tilde{U}_B^{\mu'} - \tilde{U}_A^{\mu}). \tag{4.29c}$$

Here, U_A^{μ} and $U_B^{\mu'}$ correspond to the vibronic contribution to the energy for electronic states A and B and proton vibrational state μ and μ', respectively. $\tilde{U}_A^{\mu}$ and $\tilde{U}_B^{\mu'}$ are the energy contributions for electronic states A and B (respectively) due to the quantized proton, which will depend on the nature of the proton PES and the vibrational states μ, μ'. ΔG is the applied driving force, and ζ_A and ζ_B are the minima positions in ζ for $U_A^{\mu}(\zeta)$ and $U_B^{\mu}(\zeta)$, respectively. Therefore, the solvent reorganization energy can be defined as $\lambda = \frac{1}{2}m\omega^2(\zeta_B - \zeta_A)^2$.[135] In Sec. III we will introduce different models of $\tilde{U}^{\mu}$ (quadratic, Morse, and quartic double well) and demonstrate how to calculate the Franck-Condon factors for these various models. While dynamics will not be explicitly simulated over ζ in this work, the influence of these PESs will directly affect the hopping rates k_f and k_b, which will be discussed in the upcoming section.

4.2.2. Simulation Methods for Generating IV Curves on a Grid

We will now describe how to use the equation developed above to model IV curves in practice.

Classical master equation (CME) for solving the PCET AH mode in 1D

In the limit of strong friction, weak coupling Γ and high temperature kT (where nuclear motions are classical), translational motion for the system is diffusive and governed by the Smoluchowski equation. Therefore, for simulating a voltammetry experiment, the dynamics

from Eq. 4.27 can be solved by a classical master equation (CME) of the following form,

$$\frac{\partial c_A^\mu}{\partial t} = D_A^x \frac{\partial^2 c_A^j}{\partial x^2} - \sum_{\mu'} (k_f^{\mu\to\mu'} c_A^\mu - k_b^{\mu'\to\mu} c_B^{\mu'})\delta(x) \tag{4.30a}$$

$$\frac{\partial c_B^{\mu'}}{\partial t} = D_B^x \frac{\partial^2 c_B^j}{\partial x^2} + \sum_{\mu} (k_f^{\mu\to\mu'} c_A^\mu - k_b^{\mu'\to\mu} c_B^{\mu'})\delta(x) \tag{4.30b}$$

where μ, μ' is an index for the proton vibrational state in species A and B, respectively, and $k_{f/b}^{\mu\to\mu'}$ are the forward/backward hopping rates between vibrational states μ and μ'. c_A^μ and $c_B^{\mu'}$ are the concentration densities of A and B in the μ and μ' proton vibrational states, respectively. The $\delta(x)$ term ensures that there is hopping between electronic states only at the electrode surface at $x = 0$, and we have assumed equal diffusion coefficients for all proton vibrational states in species A and B ($D_A^x = D_B^x \equiv D$). To visualize these combined electronic-vibrational energy surfaces, see Fig. 4.1.

Note that equation 4.30 does not contain any ζ coordinate terms; we will not explicitly simulate diffusive dynamics over this coordinate, and instead incorporate this dimension solely through the hopping rates $k_f^{\mu\to\mu'}$ and $k_b^{\mu'\to\mu}$; see Eq. 4.32 below. For all results below, we will choose spatial and initial boundary conditions as follows:

$$c_A^\mu(t=0,x) = \frac{e^{-\beta U_A^\mu}}{\sum_\nu e^{-\beta U_A^\nu}} \tag{4.31a}$$

$$c_B^\mu(t=0,x) = 0 \tag{4.31b}$$

$$c_A^\mu(t,x=-1) = c_A^\mu(t,x=0) \tag{4.31c}$$

$$c_B^\mu(t,x=-1) = c_B^\mu(t,x=0) \tag{4.31d}$$

$$c_A^\mu(t,x=\infty) = \frac{e^{-\beta U_A^\mu}}{\sum_\nu e^{-\beta U_A^\nu}} \tag{4.31e}$$

$$c_B^\mu(t,x=\infty) = 0. \tag{4.31f}$$

Eq. 4.31 states that the initial concentrations at all x are equal to the bath concentrations of species A and B, (e) - (f) implies that these bath concentrations (at $x = \infty$) remain

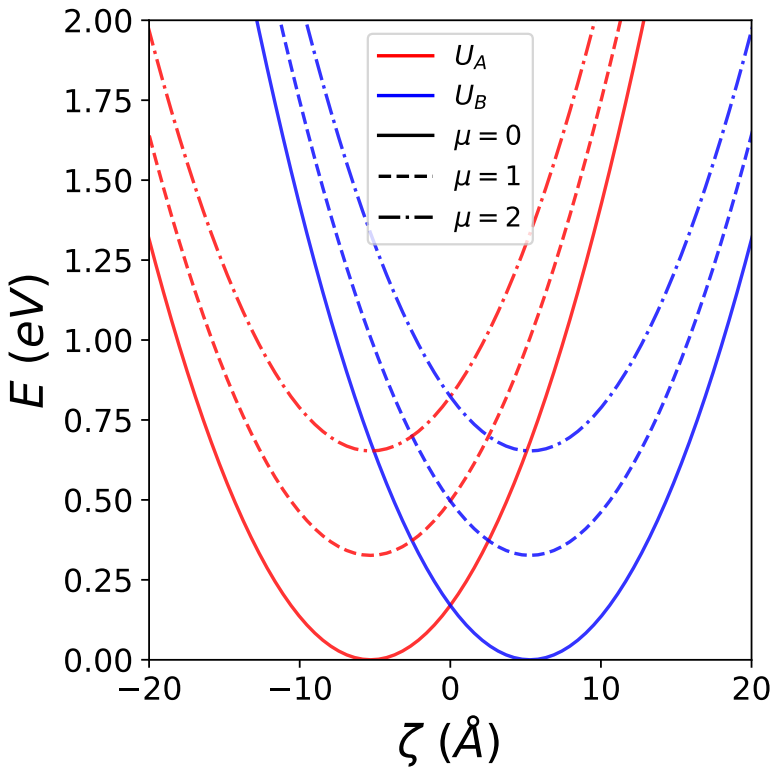

Figure 4.1: Diabatic PESs for A and B for a system with three proton vibrational states, where μ is the vibrational state index. Here, the proton vibrational states are treated as harmonic oscillator states, with energy spacing $\hbar\omega_p$. All parameters are in atomic units (a.u.), and are $m = 2000$, $\omega = 0.00025$ (from Eq. 4.29), $\omega_p = 0.012$, $\Gamma = 10^{-5}$, $\Delta G = 0$, and $kT = 0.00095$.

unchanged throughout the simulation, and (c)-(d) implies the boundary conditions at $x = -1$ are chosen to satisfy a no flux boundary condition. These boundary conditions ensure equivalence between the SH algorithm and traditional electrochemical Butler-Volmer (BV) ET boundary conditions when there are only two states involved.[136]

Unless stated otherwise, we will employ the rate constants k_f and k_b as found by averaging the full rate constant over the solvent coordinate ζ, resulting in the Marcus-Hush-Chidsey

(MHC) rate constant:

$$k_f^{\mu\to\mu'} = \frac{\Gamma}{\hbar}\frac{\int_{-\infty}^{\infty} d\zeta\ e^{-\beta U_A^{\mu}(\zeta)} f(E^{\mu,\mu'}(\zeta))}{\int_{-\infty}^{\infty} d\zeta\ e^{-\beta U_A^{\mu}(\zeta)}} \tag{4.32a}$$

$$k_b^{\mu'\to\mu} = \frac{\Gamma}{\hbar}\frac{\int_{-\infty}^{\infty} d\zeta\ e^{-\beta U_B^{\mu'}(\zeta)} (1-f(E^{\mu,\mu'}(\zeta)))}{\int_{-\infty}^{\infty} d\zeta\ e^{-\beta U_B^{\mu'}(\zeta)}}. \tag{4.32b}$$

By reducing all dynamics to 1D, and estimating solvent effects entirely through a coarse-grained hopping rate, one can achieve an enormous reduction in computational cost. For instance, we have found that simulating IV curves over both coordinates x and ζ, as was done in Ref. 49, is computationally unfeasible on our cluster with more than three proton vibrational states. For this reason, we have made *Assumption # 7*, i.e. we assume U_A and U_B do not depend on x. If U_A or U_B were to depend on x (as well as ζ), a 1D reduction would not be straightforward. That being said, in Ref. 49 it was shown that simulating ET over the diffusive dimension x (with hopping rates given by Eq. 4.32) is analytically and numerically equivalent to simulating diffusion over both x and ζ (as long as there was no explicit x dependence on the diabatic PESs for species A and B). Future work (on a larger computer) may well explore 2D PCET dynamics, with explicit nuclear motion in x and ζ. In Appendix I we show that simulation in 1D with the MHC rate is equivalent to simulation in 2D for PCET in a simple case.

Simulating voltammetry and measuring current

To simulate a voltammetry experiment, the external potential ΔG (which is equivalent to the difference in free energy of the product and reactant) must be changed as Eq. 4.30 is propagated forward in time. A common experimental approach is linear sweep voltammetry, whereby the potential is ramped linearly with scan rate ν,

$$\Delta G(t) = \Delta G_i + \nu t, \tag{4.33}$$

and ΔG_i is the starting driving force. This ramp in ΔG is maintained until reaching the final ΔG value, ΔG_f. For this work, $\Delta G_f = -\Delta G_i$. To measure current, we use the difference in forward and backward rates,

$$I(t) = \sum_{\mu,\mu'} (k_f^{\mu\to\mu'}(t) c_A^{\mu}(t) - k_b^{\mu'\to\mu}(t) c_B^{\mu'}(t))|_{x=0}, \tag{4.34}$$

where the double sum is over all proton vibrational states for both electronic states A and B. Eq. 4.34 is equivalent to measuring the current from the flux of either species A or B at $x = 0$,

$$I(t) = D_A^x \sum_{\mu} \frac{\partial c_A^{\mu}}{\partial x}|_{x=0} = -D_B^x \sum_{\mu'} \frac{\partial c_B^{\mu'}}{\partial x}|_{x=0}, \tag{4.35}$$

Solving the CME: Diagonalizing the operator for diffusion and hopping

In order to propagate Eq. 4.30 over a long enough time to simulate a voltammetry experiment, we will diagonalize the operator for diffusion and stochastic hopping. This approach has been previously applied to study ET dynamics in a two state system with diffusion[89], and more recently, to study electrochemical ET under liner sweep conditions[49]. The method below is very similar to that found in Ref. 49, with the exception being the addition of proton vibrational states through the quantized proton coordinate. In order to demonstrate the method from scratch, let us rewrite Eq. 4.30 in the following way:

$$\frac{\partial c_A^{\mu}}{\partial t} = \mathfrak{L}_A c_A^{\mu} - \sum_{\mu'} (k_f^{\mu\to\mu'} c_A^{\mu} - k_b^{\mu'\to\mu} c_B^{\mu'})\delta(x) \tag{4.36a}$$

$$\frac{\partial c_B^{\mu'}}{\partial t} = \mathfrak{L}_B c_B^{\mu'} + \sum_{\mu} (k_f^{\mu\to\mu'} c_A^{\mu} - k_b^{\mu'\to\mu} c_B^{\mu'})\delta(x). \tag{4.36b}$$

Here, we define superoperators:

$$\mathfrak{L}_A = \frac{\partial}{\partial x}(D_A \frac{\partial}{\partial x}) \tag{4.37a}$$

$$\mathfrak{L}_B = \frac{\partial}{\partial x}(D_B \frac{\partial}{\partial x}). \tag{4.37b}$$

To be as specific as possible, let us now consider the case of a two vibrational state system, with energy spacing $\hbar\omega_p$. Combining $\mathfrak{L}_A, \mathfrak{L}_B, k_f$, and k_b, we can obtain the general matrix equation for c_A and c_B,

$$\begin{pmatrix} \dot{c}_A^0 \\ \dot{c}_A^1 \\ \dot{c}_B^0 \\ \dot{c}_B^1 \end{pmatrix} = \begin{pmatrix} \mathfrak{L}_A - \sum_i^2 k_f^{0\to i}\delta(x) & 0 & k_b^{0\to 0}\delta(x) & k_b^{1\to 0}\delta(x) \\ 0 & \mathfrak{L}_A - \sum_i^2 k_f^{1\to i}\delta(x) & k_b^{0\to 1}\delta(x) & k_b^{1\to 1}\delta(x) \\ k_f^{0\to 0}\delta(x) & k_f^{1\to 0}\delta(x) & \mathfrak{L}_B - \sum_i^2 k_b^{0\to i}\delta(x) & 0 \\ k_f^{0\to 1}\delta(x) & k_f^{1\to 1}\delta(x) & 0 & \mathfrak{L}_B - \sum_i^2 k_b^{1\to i}\delta(x) \end{pmatrix} \begin{pmatrix} c_A^0 \\ c_A^1 \\ c_B^0 \\ c_B^1 \end{pmatrix} + \vec{y}$$

$$\dot{\vec{c}} = \mathfrak{M}\vec{c} + \vec{y} \tag{4.38}$$

The generalization to many vibrational states is straightforward. Here, in Eq. 4.38, the $\vec{y}$ term is used to include the bath conditions from Eqs. 4.31 (e) and (f), which maintain a static condition at the bath boundary, i.e. $\dot{\vec{c}}(x = \infty) = \vec{0}$. In other words, $\vec{y}(x \neq \infty) = 0$ and $\vec{y}(x = \infty) = -(\mathfrak{M}\vec{c})(x = \infty)$. The size of the grid in x space is chosen to be large enough such that no numerical issues are introduced by the possible discontinutiy of going from $\vec{y} = 0 \to \vec{y} = -(\mathfrak{M}\vec{c})$ at $x = \infty$.

$\mathfrak{M}$ can be non-Hermitian, since the off-diagonal elements of $\mathfrak{M}$ are not equal ($k_f^{i\to i'} \neq k_b^{i'\to i}$) in general. Since diagonalization of non-Hermitian matrices is often unstable, one needs to transform $\mathfrak{M}$ into a Hermitian matrix. To do so, we define the transformation matrix S as

$$S = \begin{pmatrix} 1 & 0 & 0 & 0 \\ 0 & e^{\frac{\beta\hbar\omega_p}{2}} & 0 & 0 \\ 0 & 0 & e^{\frac{\beta\Delta G}{2}} & 0 \\ 0 & 0 & 0 & e^{\frac{\beta(\Delta G + \hbar\omega_p)}{2}} \end{pmatrix}, \tag{4.39}$$

such that the new operator $\widetilde{\mathfrak{M}}$ satisfies:

$$\widetilde{\mathfrak{M}} = S\mathfrak{M}S^{-1} = \begin{pmatrix} \mathfrak{L}_A - \sum_i^2 k_f^{0\to i}\delta(x) & 0 & k_b^{0\to 0}\delta(x)e^{-\frac{\beta E^{0,0}}{2}} & k_b^{1\to 0}\delta(x)e^{-\frac{\beta E^{0,1}}{2}} \\ 0 & \mathfrak{L}_A - \sum_i^2 k_f^{1\to i}\delta(x) & k_b^{0\to 1}\delta(x)e^{-\frac{\beta E^{1,0}}{2}} & k_b^{1\to 1}\delta(x)e^{-\frac{\beta E^{1,1}}{2}} \\ k_f^{0\to 0}\delta(x)e^{\frac{\beta E^{0,0}}{2}} & k_f^{1\to 0}\delta(x)e^{\frac{\beta E^{1,0}}{2}} & \mathfrak{L}_B - \sum_i^2 k_b^{0\to i}\delta(x) & 0 \\ k_f^{0\to 1}\delta(x)e^{\frac{\beta E^{0,1}}{2}} & k_f^{1\to 1}\delta(x)e^{\frac{\beta E^{1,1}}{2}} & 0 & \mathfrak{L}_B - \sum_i^2 k_b^{1\to i}\delta(x) \end{pmatrix} \tag{4.40}$$

Note that $\widetilde{\mathfrak{M}}$ is Hermitian and can be easily diagonalized (and that $S\mathfrak{L}_A S^{-1} = \mathfrak{L}_A$ because D_A is a constant, with no x-dependence). While the eigen*vectors* of $\widetilde{\mathfrak{M}}$ will differ from those of $\mathfrak{M}$, $\mathfrak{M}$ and $\widetilde{\mathfrak{M}}$ are related by a similarity transformation, so that the eigen*values* are identical for both and one can analyze the dynamics of the system at any arbitrary time using either.

By diagonalizing $\widetilde{\mathfrak{M}}$ at each time step we can simulate a linear sweep voltammetry experiment. Once we have the eigenvectors P and eigenvalues Λ of $\widetilde{\mathfrak{M}} = P\Lambda P^T$ we can change variables and recast the differential equation for the time evolution of c_A and c_B into renormalized coordinates:

$$\vec{b} \equiv P^T S\vec{c} \tag{4.41a}$$

$$\vec{z} \equiv P^T S\vec{y}. \tag{4.41b}$$

The final equation of motion becomes:

$$\dot{\vec{b}} = \Lambda\vec{b} + \vec{z}. \tag{4.41c}$$

Eq. 4.41c can be solved for any time step exactly, given by

$$\vec{b}(t) = \vec{b}_{eq} + (\vec{b} - \vec{b}_{eq})e^{\Lambda t} \tag{4.42a}$$

$$\vec{b}_{eq} = -\Lambda^{-1}\vec{z}. \tag{4.42b}$$

With Eq. 4.41a, we can change $\vec{b}(t)$ to $\vec{c}(t) = \begin{pmatrix} c_A \\ c_B \end{pmatrix}$ using P and S: $\vec{c} = S^{-1}P\vec{b}$. Therefore, the current at each time step can be calculated with complete numerical stability.

4.2.3. Parameters

We will work in both atomic and standard units throughout this paper and, unless stated otherwise, set ν = 112 V/sec (10^{-16} a.u.), Γ = 0.00027 eV (10^{-5} a.u.), $D = 5.5 \cdot 10^{-4}$ cm^2/sec ($4.75 \cdot 10^{-4}$ a.u.), $\omega = 1.03 \cdot 10^{13}$ sec^{-1} (0.00025 a.u.), $m = 1.82 \cdot 10^{-27} kg$ (2000 a.u.), $T = 300K$ (0.00095 a.u.), $\zeta_A = -5.29$ Å (-10 a.u.), $\zeta_B = 5.29$ Å (10 a.u.), $N_x = 50$. The size of the grid in x is given by $L_x = 6\sqrt{Dt_T}$, where t_T is the total time of the simulation, defined by the starting and ending ΔG and ν, $t_T = \frac{|\Delta G_f - \Delta G_i|}{\nu}$, and the grid spacing is uniform, such that $dx = \frac{L_x}{N_x}$. In general, we will break apart a IV curve into $N_T = 2000$ discrete changes in driving force, and use Eq. 4.42 to propagate the system for each discrete time step.

4.2.4. Understanding and Interpreting IV Curves

Typically speaking, in electrochemistry without any quantized proton motion, the shape of IV curves and peak parameters are functions of a unit-less parameter $\Lambda = \frac{k^0}{\sqrt{D\nu \frac{F}{RT}}}$ [50,78]. In the regime where $\Lambda > 10$, the kinetic behavior is reversible, i.e. the rate of ET is much faster than any other time scale in the simulation, and the peak parameters are dictated entirely by D and ν. When $\Lambda < 0.001$, the kinetic behavior is totally irreversible and the peak parameters should be dictated by the ET kinetics through the parameter k^0. Finally, when $10 \geq \Lambda \geq 0.001$, the behavior is deemed "quasireversible" by Matsuda and Ayabe, where neither ET kinetics, mass transfer, or scan rate uniquely dictate the IV curve shape and peak parameters. With this framework in mind, and in order to help the reader interpret our our simulation data intuitively, we will include values of Λ in the caption of each figure below (for each relevant set of data). Obviously, one cannot fully understand PCET in the context of simple ET rates (see Sec. IV.B), but we believe having a rough estimate of Λ should be

useful as far as establishing the proper transport regime. To that end, for k^0, we use the value $\Gamma \cdot FC(0,0)$, where $FC(0,0)$ is the Franck-Condon factor between ground vibrational states in electronic states 0 and 1. However, using Λ as a true estimate for the reversibility or irreversibility of a given reaction can be dangerous: after all, for the PCET framework above, for every single donor vibronic state there are multiple acceptor vibronic states (each with a different Franck-Condon factor), and the relevant acceptor state can depend on scan rate, diffusion constant, and/or mass (hydrogen/deuterium). Thus, one cannot ascribe to a given Hamiltonian a unique Λ value. Furthermore, we also mention that in the context of Matsuda/Yamuda Λ values, one usually presumes that electrochemical dynamics occur with Bulter-Volmer rate constants (rather than the MHC rate constants defined above in Eq. 4.32); nevertheless, we believe the Λ values reported below in each figure should be meaningful, at least qualitatively.

4.3. Results

All results below will depend critically on the choice of Hamiltonian for the proton, which generates the key parameters U_0^{μ} and $U_1^{\mu'}$. We will work with three different functional forms of the proton potential; harmonic potentials, Morse potentials, and double well quartic potentials.

4.3.1. Harmonic Oscillator Eigenstates

The simplest possible choice for proton PESs are harmonic oscillators with energy spacing $\hbar\omega_p$. If V_0 is the potential for the proton assuming the molecule is uncharged, and V_1 is the potential for the proton assuming the molecule is charged, we can write:

$$\begin{aligned} V_0(q) &= \frac{1}{2} m\omega_p^2 q^2 \\ V_1(q) &= \frac{1}{2} m\omega_p^2 (q - g_p)^2, \end{aligned} \tag{4.43}$$

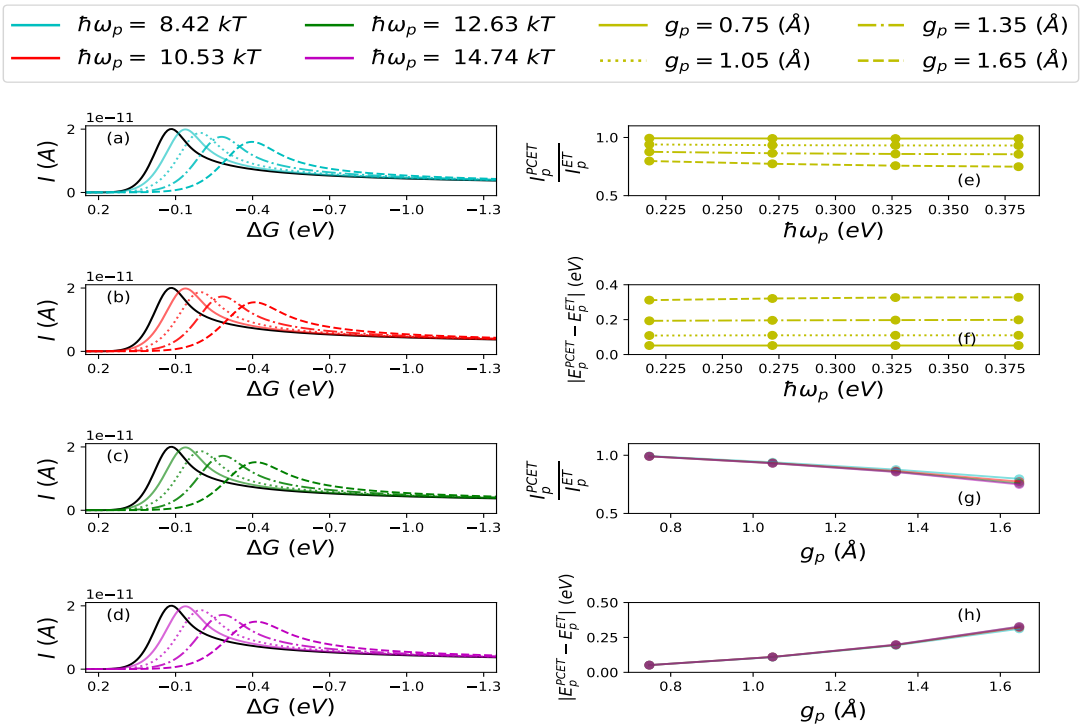

Figure 4.2: (a)-(d) 1D Linear sweep voltammograms for the harmonic oscillator model at different values of ω_p and g_p. (a) $\omega_p = 8.42kT$, (b) $\omega_p = 10.53kT$, (c) $\omega_p = 12.63kT$, (d) $\omega_p = 14.74kT$. (e) and (g) show the ratio of the peak current in the PCET simulation to that of the ET simulation, with respect to frequency ω_p and displacement in q (g_p), respectively. (f) and (h) show the deviation of the peak potential in the PCET simulation and the ET simulation, with respect to frequency ω_p and g_p, respectively. In (g) through (h) the colors of points and lines correspond to their respective ω_p values from (a) - (d). The different curves correspond to different values of g_p, ranging from $0.75 - 1.65$. The black trace shows the case with no proton coordinate, for reference. From the data in (e) – (g), we see that there is no dependence on ω_p for either I_p or E_p, suggesting that all hops are between ground vibrational states in electronic states A and B. Thus, the dependence of I_p and E_p on g_p suggests that the main influence of PCET on the rate of ET is through the orbital overlaps between the two ground vibrational states at a given value of g_p, and therefore the overall effect of the proton is just to reduce the value of the standard rate constant. For these systems, Λ values are well defined and range from $\Lambda = 520.26$ for $g_p = 0.75$ to $\Lambda = 11.18$ for $g_p = 1.65$. Here, we are operating largely in the reversible regime.

which allows for an analytical calculation of the Franck-Condon factors. Note that $[\frac{\Pi^2}{2m_q} + V_0(q)]\,|\mu\rangle = \tilde{U}_A^{\mu}\,|\mu\rangle$. The Franck-Condon factors are

$$F_{\mu\to\mu'} = \langle\mu|\mu'\rangle = \int dq\phi_\mu(q+g_p)\phi_{\mu'}(q), \tag{4.44}$$

where $\phi_\mu(q)$ is the μ^{th} eigenstate of the harmonic oscillator at position q and g_p is the normalized displacement of the two eigenstates in q. $F_{\mu\to\mu'}$ can be calculated by the following expression[137,138]:

$$F_{\mu\to\mu'} = \frac{p!}{Q!}^{0.5} (\frac{g_p}{\sqrt{2}})^{Q-p} e^{-\frac{g_p^2}{4}} L_p^{Q-p}(\frac{g_p^2}{2})[sgn(\mu'-\mu)]^{\mu-\mu'}. \tag{4.45}$$

Here, p/Q are the minimum/maximum of μ and μ', sgn is the sign function, and L_m^n is a generalized Laguerre polynomial. The reorganization energy in the proton coordinate, λ_p, is defined as $\lambda_p = \frac{\hbar\omega_p g_p^2}{2}$. In Fig. 4.2 we show that different IV curves do arise from inclusion of the proton coordinate. Here, (i) linear voltammograms are plotted for different combinations of ω_p and g_p, along with (ii) the ratio of peak currents for PCET and ET, $\frac{I_p^{PCET}}{I_p^{ET}}$ and (iii) the deviation of the peak potential between PCET and ET, $|E_p^{PCET} - E_p^{ET}|$. Here E_p corresponds to the overpotential at which the IV curve has its maximum value, while I_p is the maximum current attained throughout the course of the voltammetry simulation. E_p^{ET} and I_p^{ET} are the values that are obtained from a simulation with identical electronic parameters, but no proton transfer. The most noticeable trends from Fig. 4.2 are (1) the relative independence of I_p and E_p with regards to ω_p, and (2) the decrease in I_p and increase in $|E_p^{PCET} - E_p^{ET}|$ with regards to increasing g_p. Taken together, these two observations suggest that the main effect of the proton transfer in this model is to decrease the standard rate constant, k^0, through the incomplete orbital overlap of the two ground proton vibrational states in electronic states A and B (see Eq. 4.45).

4.3.2. Morse Potential

In addition to harmonic oscillator eigenstates, the proton coordinate can be represented by a basis of Morse oscillator eigenstates. The Franck-Condon factors for these potentials can be numerically calculated using Eq. 4.44, with eigenstates and energy spacings from analytical

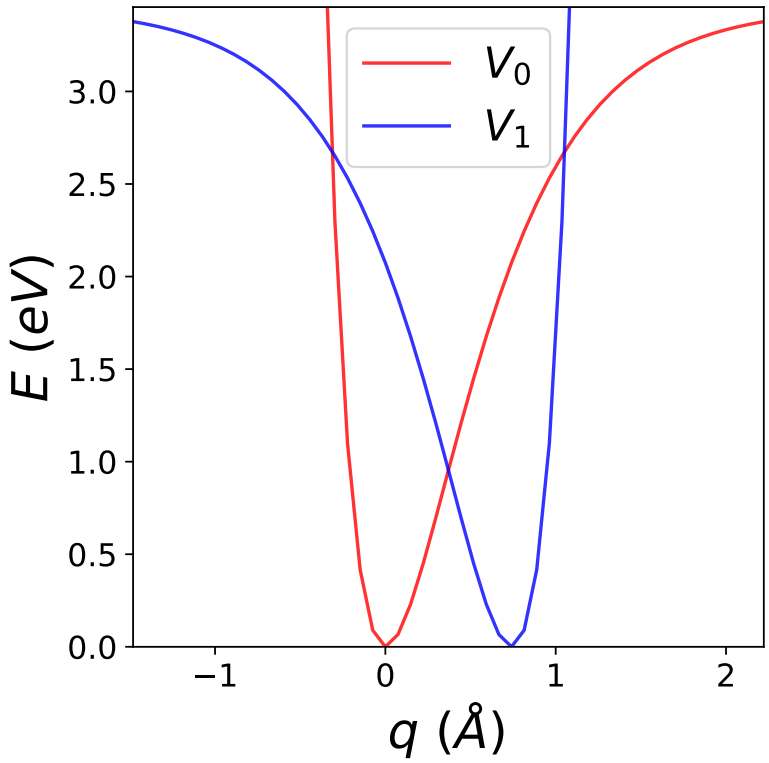

Figure 4.3: Example of $V_0(q)$ and $V_1(q)$ for the Morse potential, $\omega_p = 12.63\ kT$, $g_p = 0.741$.

solutions[139]. In this instance, the PESs in the proton coordinate are

$$\begin{aligned} V_0(q) &= D_e(1 - e^{aq})^2 \\ V_1(q) &= D_e(1 - e^{-a(q-g_p)})^2, \end{aligned} \tag{4.46}$$

where $a = \sqrt{\frac{m\omega_p^2}{2D_e}}$, and we allow g_p to vary. The energy levels are given by $E_n = \hbar\omega_p \frac{2D_e + 4nD_e - \hbar\omega_p(n^2+n+\frac{1}{4})}{4D_e}$, and we set $D_e = 10\omega_p$. Therefore, ω_p affects the energy level spacing, and g_p affects the proton wavefunction overlap between states A and B. The voltammograms comparing ET to PCET with Morse oscillators for the proton states are shown in Fig. 4.4. We see some of the same qualitative behavior as compared with the harmonic oscillator case, whereby I_p decreases and E_p increases as a function of increased spacing in the proton coordinate. However, Fig. 4.4 (d) shows that at large spacings in q the peak potential is dependent on ω_p, in contrast to the harmonic oscillator case. This suggests

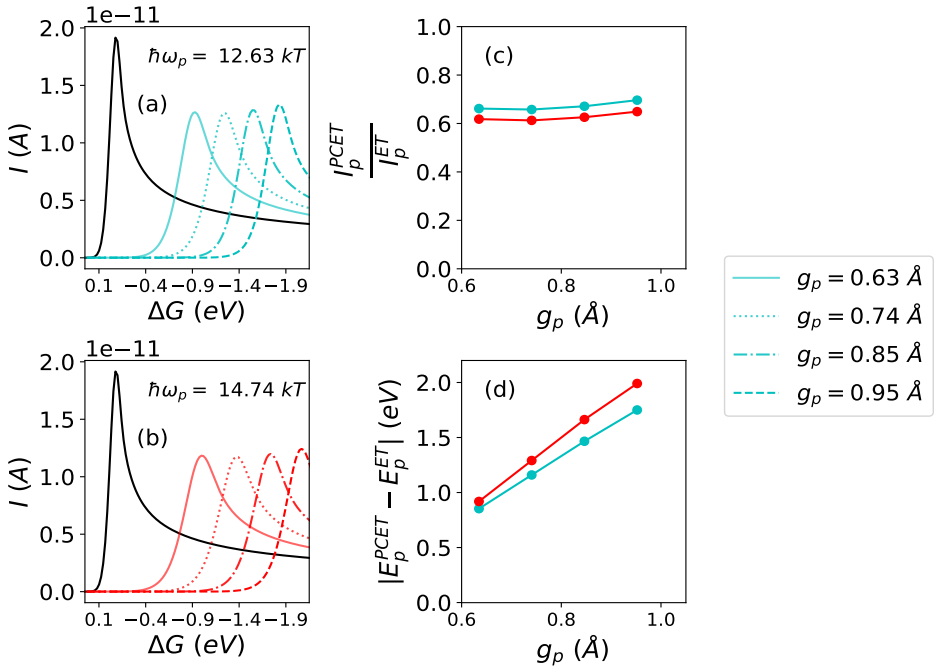

Figure 4.4: (a), (b) 1D Linear sweep voltammograms for the Morse oscillator model at different values of ω_p and g_p. (a) $\omega_p = 10.53kT$, (b) $\omega_p = 14.74kT$. (c) Ratio of the peak current in the PCET simulation to that of the ET simulation, with respect to displacement in q (g_p) of the two electronic states 0 and 1. (d) Deviation of the peak potential in the PCET simulation versus the ET simulation, with respect to g_p. The black trace shows the case with no proton coordinate, for reference. Qualitatively, we see some of the same behavior as the harmonic oscillator case, such as E_p increasing; though bizarrely, we find that I_p seems to modestly increase with g_p. Even more interestingly, at large g_p we see that there is now a ω_p dependence on the peak position. This suggests that the mechanism of PCET is different from that of the harmonic oscillator proton PES, as hops can now occur between ground and excited states in 0 and 1, respectively, instead of between ground state and ground state. Thus, Λ values for these reactions are not entirely well-defined. Using the 0-0 (ground-to-ground) transition as reference, the Λ values for these results range from $\Lambda = 0.0541$ for $g_p = 0.63$ to $\Lambda = 4.38 \cdot 10^{-7}$ for $g_p = 0.95$. If the Λ values above are relevant, then here we operate in the quasi-reversible and irreversible regimes (whereas Fig. 4.2 operates in the reversible regime).

that the ET mechanism can be different in the Morse oscillator case versus the harmonic oscillator case; apparently, hops can occur (in practice) between the ground vibrational state in A and excited vibrational states in B.

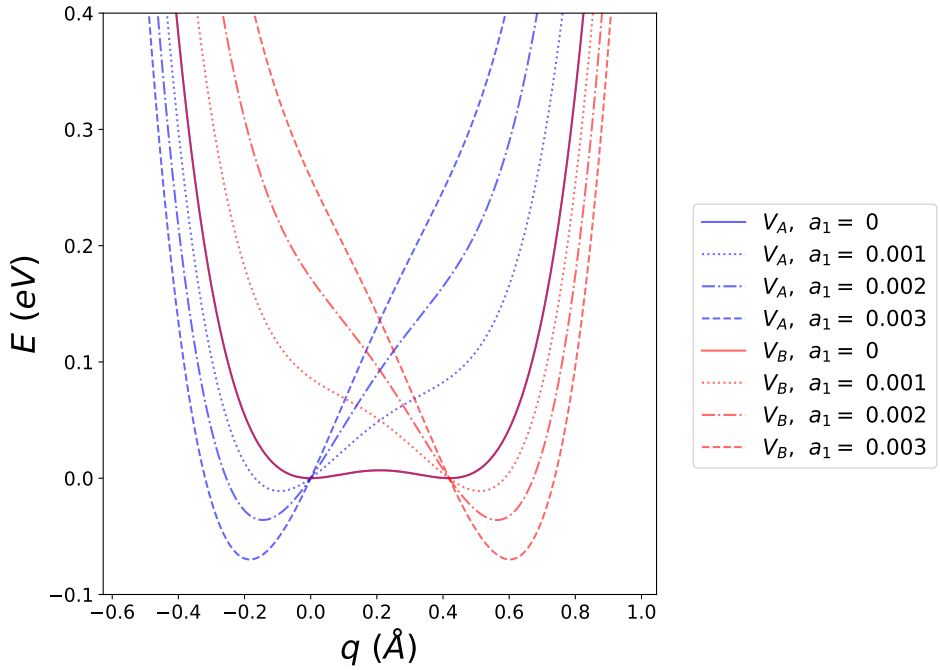

Figure 4.5: Proton PESs for A and B in q for different values of a_1. $m = 1.82 \cdot 10^{-27} kg$, $\omega_p = 8.42kT$, $a_4 = 0.005$, $a_2 = 0.05$. Note that the PESs for A and B are symmetric with $q_c = \sqrt{\frac{2.5\hbar}{m\omega_p}}$.

4.3.3. Quartic Potential

Our last model potential will be the quartic double well proton PES[140,141,142]. The PESs are given by

$$V_A(q) = E_{ref}\left(\frac{a_4^A}{L^4}(q-q_c)^4 - \frac{a_2^A}{L^2}(q-q_c)^2 + \frac{a_1^A}{L}(q-q_c)\right) \tag{4.47a}$$

$$V_B(q) = E_{ref}\left(\frac{a_4^B}{L^4}(q_c-q)^4 - \frac{a_2^B}{L^2}(q_c-q)^2 + \frac{a_1^B}{L}(q_c-q)\right) \tag{4.47b}$$

where q_c is the crossing of the two PESs for A and B. For our simulations, we restrict ourselves to the case where the a coefficients are the same for species A and B (i.e. $a_i^A = a_i^B$ for $i = 1, 2, 4$). L is a reference length scale, $L = \sqrt{\frac{\hbar}{m\omega_p}}$, and E_{ref} is a reference energy scale. q_c is chosen as $\sqrt{\frac{a_2\hbar}{4a_4 m\omega_p}}$, and shown in Fig. 4.5 are example quartic PESs for four different values of a_1. When $a_4 = a_1 = 0$, $a_2 = -1$, this model is identical to the quadratic

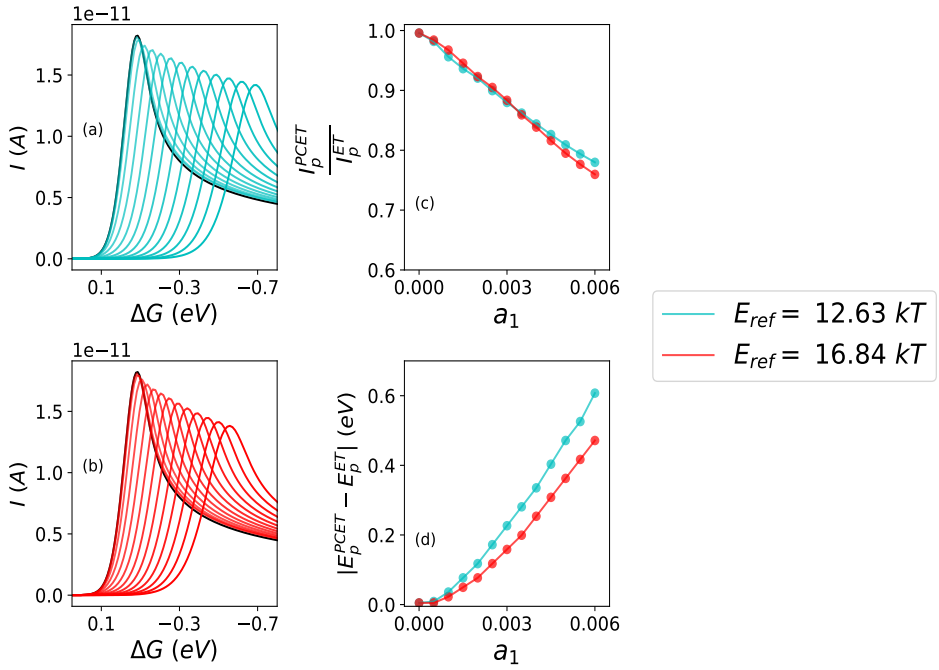

Figure 4.6: 1D Linear sweep voltammograms at different values of ω_p and a_1 for the quartic PES in the proton coordinate. (a) $L = 0.25$ ($\omega_p = 8.42kT$), $E_{ref} = 8.42kT$. (b) $L = 0.204$ ($\omega_p = 12.63kT$), $E_{ref} = 12.63kT$. $a_4 = 0.005$, $a_2 = 0.05$. a_4 and a_2 are chosen such that q_c is the same for both models in (a) and (b). The black trace shows the case with no proton coordinate, for reference. (c) Ratio of the peak current in the PCET simulation to that of the ET simulation, with respect to the parameter a_1 of the quartic PES. (d) Deviation of the peak potential in the PCET simulation and the ET simulation, with respect to the parameter a_1 of the quartic PES. Qualitatively, we see very similar behavior to the anharmonic Morse oscillator. This finding reaffirms the notion that anharmonicity in the proton coordinate PES due to a_1 can give rise to slightly different effects in the voltammetric simulation, suggesting that knowledge of the proton PES is essential for modeling an IV experiment quantitatively accurately. As in Fig. 4.4, from the fact that different E_{ref} values give different curves for E_p and I_p, we find that not all transitions are 0-0 vibronic, and thus again the Λ values may not be well defined. Nevertheless, for reference, the 0-0 Lambda values range from $\Lambda = 1414.21$ for $a_1 = 0$ to $\Lambda = 0.090$ for $a_1 = 1.65, E_{ref} = 12.63$, and $\Lambda = 1.25$ for $a_1 = 1.65, E_{ref} = 16.84$. If these Λ values are relevant, then as in Fig. 4.2, we are largely operating in the reversible and quasi-reversible regimes.

harmonic oscillator model. The parameter a_1 dictates the asymmetry of the two wells in the quartic model, and yields symmetric double wells when $a_1 = 0$. We compute the energy levels/spacings and wavefunctions/Franck-Condon factors numerically, and we use the lowest 10 levels in our simulations. In Fig. 4.6 we show voltammograms for different values of ω_p and a_1. When $a_1 = 0$, the proton coordinate PESs are identical for both electronic states

A and B, and as expected we see no deviation from the ET case for this parameter choice. However, as a_1 is increased, the asymmetry between proton PESs increases, introducing quantitative differences in I_p and E_p when compared to ET. Similar to the other two models examined, I_p decreases and E_p increases as a function of increasing g_p (i.e. decreasing the orbital overlap between ground proton vibrational states). However, much like the Morse potential, I_p and E_p both depend on ω_p, which is also a direct probe of the energy spacings in this model.[143] Interestingly, these results, along with those from the Morse potential, suggest that including anharmonicity in the proton PES can result in different mechanisms for ET when including a quantized proton.

4.3.4. Proton Coordinate Spacing of A and B as an Additional Degree of Freedom

Up to this point, we have restricted our attention to cases where the displacement between the proton PESs $\tilde{U}_A^{\mu}$ and $\tilde{U}_B^{\mu'}$ is constant (see Fig. 4.2). However, it is well known from the PCET literature that the this spacing in q between energetic minima can change on a very fast timescale due to the proton donor-acceptor vibrational motion, which can be influenced by other coordinates within the system as well. One way to model a non-constant displacement in the proton PESs is by sampling from a distribution of displacement values at each time step. To this end, we can perform simulations in the harmonic oscillator basis where g_p (see Eq. 4.44) at every time step of the simulation is drawn from a lognormal distribution of g_p values, with mean $\bar{g}_p$ and variance σ. Plotted in Fig. 4.7 are voltammograms for various g_p distribution parameters, along with the same simulations for a single g_p value, equal to $\bar{g}_p$. Overall, the results have a simple interpretation. At small σ values, the distribution of g_p values simulations gives the same IV curve as the single g_p value, as anticipated. However, at larger σ values, we see an earlier onset of current with respect to overpotential. This early onset effect is due to the presence of smaller g_p values in our electrochemical simulations, allowing for the possibility of much larger Franck-Condon factors between the ground vibrational states in A and B as compared to the case when g_p is fixed. This finding

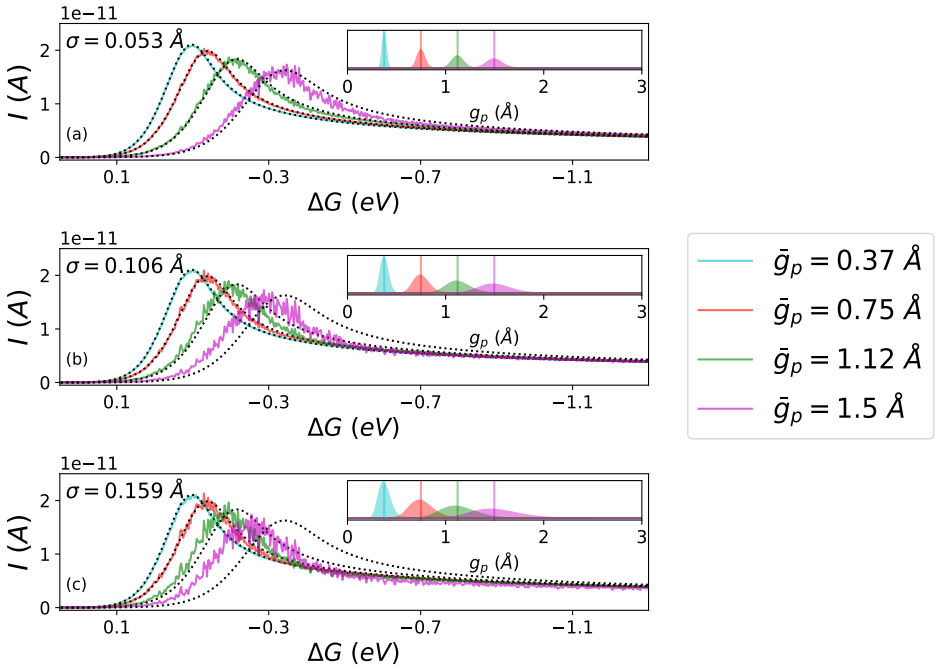

Figure 4.7: 1D Linear sweep voltammograms at different values of $\bar{g}_p$ and σ, the mean and variance respectively, of the lognormal distribution from which g_p values are selected at each time step of the simulation, $\omega_p = 12.63kT$. Simulations are for the harmonic oscillator PESs. The dotted black trace shows the case with where g_p takes a single value throughout the simulation, equal to the mean of the underlying distribution. The inset of each subplot shows the probability distribution function of g_p values for each parameterization. Due to the stochastic nature of the g_p sampling process, the curves here are averaged over 200 simulations. (a) $\sigma = 0.1$, (b) $\sigma = 0.2$, (c) $\sigma = 0.3$. As σ approaches zero, the IV curve approaches the single value g case, as expected. However, at larger $\bar{g}_p$ and σ values, we see that the onset of current occurs at lower overpotential. This early onset arises because, as the distribution widens, lower g_p values can be selected with much higher probability, increasing the Franck-Condon factors between the ground vibrational state in 0 and ground vibrational state in 1.

is particularly noteworthy, as experimental IV curves are more likely to resemble the noisy curves seen in Fig. 4.7 than those of the static g_p case in Fig. 4.2.

4.4. Discussion

The data above has demonstrated that the presence of proton motion can influence the nature of the IV curve, leading to final results that can be different quantitatively from the bare ET case. For instance, we observe that E_p can often occur at large overpotentials that

depend on the nature of the proton PES and I_p can be reduced by as much as 40%. These differences between ET and PCET behavior represent a significant finding. As such, one would very much like a diagnostic tool for assessing whether or not proton motion is inherent in a given electrochemical experiment. With this intention in mind, one can ask whether one can find single quantitative diagnostics of PCET. To that end, we have investigated the usual electrochemical tools from the literature: first, the dependence of peak current and peak potential on diffusion strength (as measured by the diffusion constant) and scan rate, and second, the effect on the IV curve of changing the hydrogen isotope to deuterium (related to the kinetic isotope effect). While we find that scan rate and diffusion constant analysis does not yield conclusive evidence of PCET, it appears that isotope effects have a specific signature whereby the peak potential E_p can shift as a function of isotope, but I_p remains relatively unchanged.

4.4.1. Dependence on Diffusion Constant and Scan Rate

In Fig. 4.8 we show the dependence of peak current and peak potential on diffusion constant and scan rate, for multiple g_p values (in the harmonic oscillator eigenstate PCET model). The $g_p = 0$ trace is the same as the ET case, and is included for reference. We see that the peak current closely follows the expected square root dependence on the diffusion constant and scan rate for all values of g_p studied[50]. For E_p, there appears to be a slight change in the behavior with respect to g_p; however, because there is no simple analytical form for E_p that we can compare against, it is not clear whether plotting E_p versus scan rate or diffusion constant can serve as a useful means of identifying whether a quantized proton is important for the mechanism being investigated.

4.4.2. Hydrogen / Deuterium Isotope Effects in a Quartic Potential

Let us now discuss another important effect in PCET, the kinetic isotope effect (KIE), whereby different isotopes of the hydrogen being transferred can greatly influence the rate constant of the overall reaction. The effect of changing the isotope from hydrogen to deu-

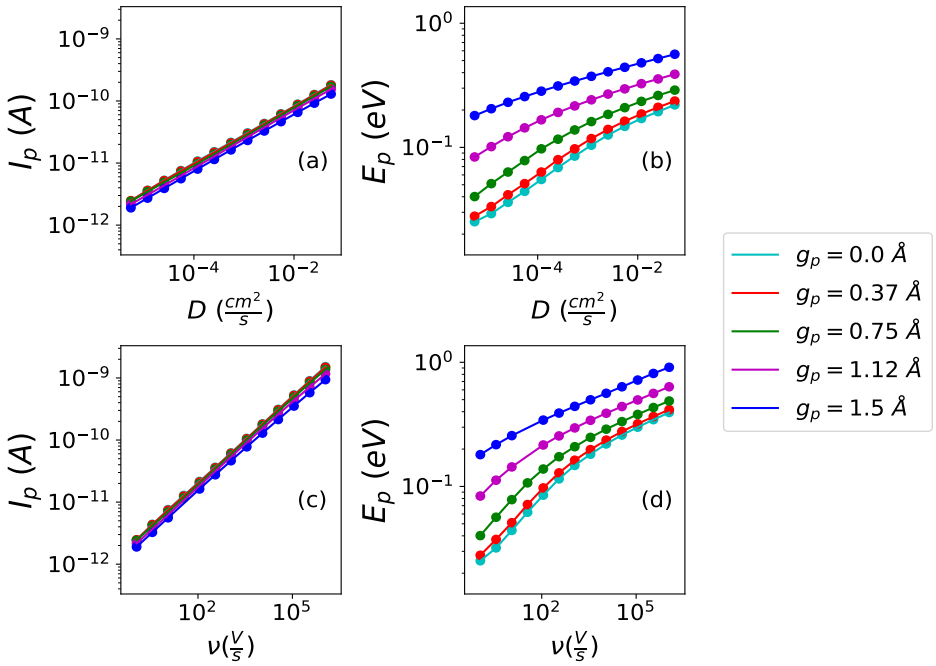

Figure 4.8: Peak current and peak potential as a function of diffusion constant and scan rate for various g_p values for the harmonic oscillator model, $\omega_p = 12.63kT$. (a), (c) Peak current versus diffusion constant and scan rate, respectively. (b), (d) Peak potential versus diffusion constant and scan rate, respectively. The square root dependence of I_p with respect to ν and D applies over a wide range of g_p values, suggesting that this observable is not suitable for determining the presence of proton transfer in an electrochemical ET/PCET experiment. While the behavior of E_p with respect to ν and D does appear to be different depending on g_p, there exists no simple analytical comparison for non-Nernstian ET, and thus no means to use Eq. 4.44 to diagnose whether a given reaction is ET or PCET.

terium leads to different Franck-Condon factors and effective coupling elements, and can lead to large changes in rate constants in other contexts. As far as electrochemical PCET simulations are concerned, within our quartic model, changing the isotope of hydrogen amounts to simply changing the mass and thereby the energy levels and the protonic wavefunctions.

The first thing we note is that, apparently, the peak current I_p does not seem to differentiate much between hydrogen and deuterium. This creates a very interesting state of affairs. After all, in Fig. 4.2 (for the case of harmonic oscillators), we showed that I_p can depend on g_p (and the electron transfer rate) in the reversible or quasi-reversible regimes. In Fig. 4.9, however, we show that I_p can sometime be roughly independent of g_p in this same regime –

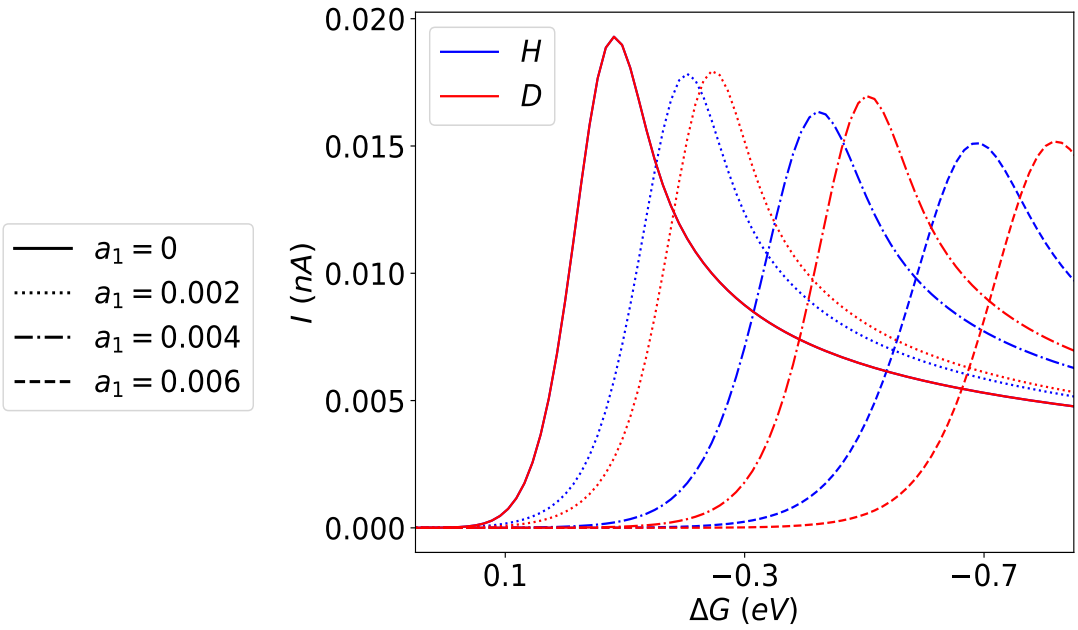

Figure 4.9: Voltammograms for a quartic potential PCET simulation for hydrogen and deuterium for multiple values of a_1. Voltammograms for hydrogen and deuterium, with $L = 0.204$, $E_{ref} = 12.63kT$, $a_4 = 0.005$, and $a_2 = 0.05$. The traces, going for left to right, are for increasing values of a_1. Blue traces correspond to hydrogen, red traces to deuterium. Note that, for $a_1 = 0$, hydrogen and deuterium yield equivalent voltammetry curves, as expected. While I_p shows almost identical behavior regardless of a_1, and is not drastically different between hydrogen and deuterium, E_p is considerably larger for the hydrogen case compared to deuterium, suggesting that there are significant isotope effects on E_p. The difference in E_p between hydrogen and deuterium is independent of scan rate and diffusion constant (not shown). Note that the peak position can shift by up to almost 150 mV. The Λ values for these results range from $\Lambda = 1414.21$ for $a_1 = 0$ to $\Lambda = 0.09$ for $a_1 = 0.006$ for hydrogen, and $\Lambda = 0.00065$ for $a_1 = 0.006$ for deuterium. For reference, the Λ values for $a_1 = 0.002$ are $\Lambda = 106.06$ for hydrogen and $\Lambda = 16.24$ for deuterium.

the relative contribution of donor and acceptor states may change as a function of mass (just as they change as a function of E_{ref} in Fig. 4.6). Obviously, one cannot perfectly match up intuition from the standard electrochemical theory (with only two quantized, electronic states) with the current problems in PCET (with more than two quantized, vibronic states): the notion of reversibility and irreversibility becomes more complicated (and interesting). To complicate the picture even more, note that we are using Marcus-Hush rate constants, rather than the more standard Butler-Volmer rate constants (see Sec. II.B.1).

Finally, let us turn to the peak potential. In Fig. 4.9 we investigate IV curves that arise when we change the proton to deuterium, and we plot voltammograms for multiple a_1 values from the quartic potential model, as well as a plot of $E_p^{PCET(D)} - E_p^{PCET(H)}$. For the peak potential, hydrogen exhibits a much earlier peak current than deuterium, on the order of up to 150 mV. Thus, one possible signature of PCET would be an IV curve whose peak position is shifted but peak current is not reduced significantly. While these results on their own do not yet offer any rigorous means of quantifying the absolute effect of isotope on the IV curve for PCET versus ET, they do suggest that the identity of the isotope being transferred concertedly with ET can have a measurable effect on the resultant voltammogram.

4.5. Conclusion

In this paper we have presented a means of simulating PCET dynamics under a time dependent driving force by propagating a SH-CME which can be solved with SH dynamics. Our approach is based on the following seven assumptions:

- Assumption # 1: No direct coupling between the proton and the solvent (no $U_0^{\mu\mu'}$ terms in Eq. 4.1)
- Assumption # 2: No direct coupling between the proton and metallic electronic states (ϵ_k does not depend on q)
- Assumption # 3: Born-Markovian approximation (weak metal-molecule coupling and fast metallic electrons); $\rho(t) = \rho_b^{eq} \otimes \rho_s(t)$
- Assumption # 4: Classical x and ζ
- Assumption # 5: W_k (electronic coupling) is independent of q (proton coordinate)
- Assumption # 6: Secular approximation (off-diagonal terms of density matrix ignored)
- Assumption # 7: U_A and U_B (electronic PESs) are independent of x (distance from the electrode)

We find that merging PT and ET in this system yields quantitatively different voltammagrams, though the IV curves are often similar qualitatively (just shifted); the exact resultant effect depends on the specific nature of the proton PES or excited vibrational states and, from the data above, we find it can be very difficult to know ahead of time whether one is operating in the reversible or irreversible regimes. Clearly, with more than one acceptor and more than one donor vibronic state, the entire concept of reversible and irreversible regimes becomes more complicated. New analytic theory will be needed to explore the nature of I_p/E_p curves as a function of a collection of reduced parameters, along the lines of what Matsuda did for standard electrochemical dynamics. Finally, turning to the specific question of isotopes, we find that isotope effects lead to deviations in E_p (though not I_p). Ultimately, however, we find that an IV curve is most likely insufficient on its own to establish the presence of PCET, and will need to be supplemented by some other type of experiment for characterizing the nature of electrochemical dynamics.

Now, some of the observations above are dependent on our choice of model Hamiltonian; namely, the lack of direct interaction between the proton and the solvent, and an absence of any relaxation pathways between excited vibrational states on a given electronic state. This choice of Hamiltonian thus prevents us from seeing alternative dynamics, such as sequential proton and electron transfer. Looking forward, the next step would be to perform these simulations with actual PCET PESs inferred from theory and experiment; once this is done, parameters could be obtained from ab-initio calculations and this framework could be applied to known experimental PCET systems to see if this approach can recover experimentally observed IV curves that deviate from current electrochemical simulation models. Also, pH effects can have a large influence on the dynamics of electrochemical systems undergoing PCET events, which were neglected for this work. Looking forward, several arenas still remain unexplored in our quest to understand PCET in electrochemical dynamics. For the interested reader, the code used in this paper will soon be available on GitHub at the address https://github.com/alecja/electrochemistry_sim.

4.6. Acknowledgements

We thank the DoD High Performance Computing Modernization Program for computer time.

4.7. Appendix I: Equivalence of 2D and 1D simulations

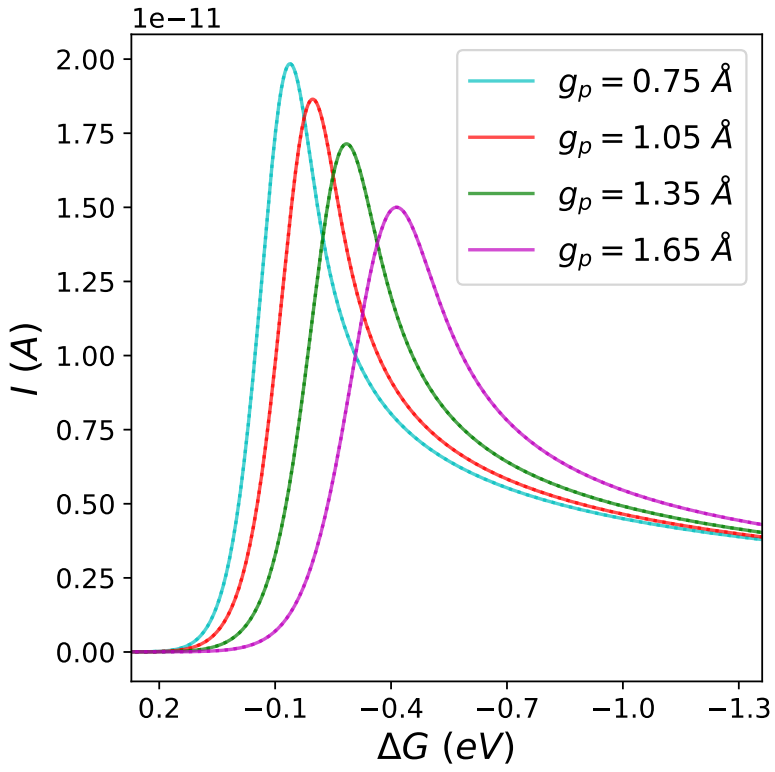

Figure 4.10: 1D Linear sweep voltammograms showing agreement between 1D and 2D simulations for a case with two vibrational states. $\omega_p = 14.74kT$, $D = 4.75 \cdot 10^{-4}$, $\nu = 10^{-16}$, $\omega = 0.00025$, $\Gamma = 10^{-5}$. All parameters are in atomic units. The 2D simulations are represented by dashed lines, and the 1D simulations by solid lines. Since the 2D and 1D simulations are in quantitative agreement, we can simulate using the less computationally intensive 1D model to study these PCET systems.

In Ref. 49, it was shown that, in the absence of PES entanglement between coordinates, a 1D model with Marcus-Hush-Chidsey rates gave quantitatively identical results to simulations over 2D (with a solvent coordinate explicitly modeled in addition to a diffusive coordinate). We would like to confirm that this result still stands true for PCET, and that inclusion

of the proton coordinate does not break this equivalency between 1D and 2D models. In Fig. 4.10 we show the equivalence of full 2D simulations over x and ζ with 1D simulations over only x for the harmonic oscillator model, where the contribution of ζ is incorporated through the Marcus-Hush-Chidsey rate. We see quantitative agreement for all values of ω_p, suggesting that the 1D model (in Eq. 4.30) is sufficient for capturing the IV behavior in these simulations.

4.8. Appendix II: Convergence of simulations with respect to number of vibrational states

Throughout this paper, we have limited our attention to $N_\mu = 2$ for the harmonic oscillator system, but one may wonder whether different effects would emerge if we were to include even more vibrational states. Plotted in Fig. 4.11 are simulations for $N_\mu = 2$ and $N_\mu = 5$ for multiple combinations of ω_p and g_p. Since the two simulations give identical results, we can surmise that there is no additional information lost or gained by choosing N_μ anywhere in the range from 2 to 5, and all simulations seem converged by $N_\mu = 5$. This conclusion makes intuitive sense, after all, as for even the smallest vibrational state spacing examined ($\omega_p = 8.42kT$), there is a spacing of over $42kT$ between the ground and highest excited vibrational state.

4.9. Appendix III: W_k dependence on proton coordinate

The QCLE-CME derivation of Sec. II can be expanded to allow for dependence of the molecule-metal coupling, W_k, on the proton coordinate q. The following derivation will focus on ρ_0 only, as the final result for ρ_1 can easily be solved by analogy. We first start

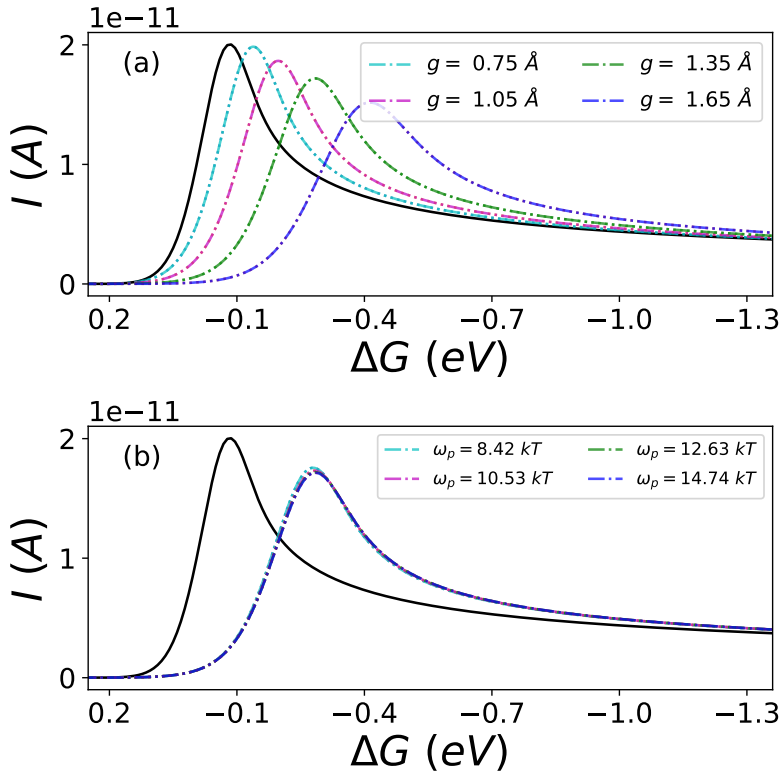

Figure 4.11: 1D Linear sweep voltammograms showing agreement between simulations with 2 and 5 vibrational states. In both subfigures the dotted lines correspond to $N_\mu = 2$ and solid, semi-transparent lines to $N_\mu = 5$. The black trace shows the same simulation, but with no proton coordinate. (a) ω_p held constant at $12.63kT$ (b) g_p held constant at 2.83. Since the $N_\mu = 2$ and $N_\mu = 5$ simulations are in quantitative agreement (the curves are on top of each other in the figure), we surmise that the relevant chemistry occurs between no more than the first two vibrational states, and no additional information is gained or lost by increasing the number of vibrational states.

with the analog of Eq. 4.22,

$$\begin{aligned}\langle\mu|\,\hat{\tilde{\mathfrak{L}}}^{vib}\hat{\rho}_0^{vib}\,|\nu\rangle = -\sum_{k,\mu',\nu',\xi}\frac{1}{\hbar^2}\int_0^\infty d\tau(&e^{-\frac{i\epsilon_k\tau}{\hbar}}f(\epsilon_k)\,\langle\mu|\,\rho_0 e^{-\frac{iH_0\tau}{\hbar}}\,|\xi\rangle\,\langle\xi|\,W_k\,|\mu'\rangle\,\langle\mu'|\,e^{\frac{iH_1\tau}{\hbar}}W_k\,|\nu\rangle\\ &-e^{-\frac{i\epsilon_k\tau}{\hbar}}(1-f(\epsilon_k))\,\langle\mu|\,e^{-\frac{iH_0\tau}{\hbar}}W_k e^{\frac{iH_1\tau}{\hbar}}\,|\mu'\rangle\,\langle\mu'|\,\rho_1\,|\nu'\rangle\,\langle\nu'|\,W_k\,|\nu\rangle\\ &-e^{\frac{i\epsilon_k\tau}{\hbar}}(1-f(\epsilon_k))\,\langle\mu|\,W_k\,|\mu'\rangle\,\langle\mu'|\,\rho_1 e^{-\frac{iH_1\tau}{\hbar}}\,|\nu'\rangle\,\langle\nu'|\,W_k e^{\frac{iH_0\tau}{\hbar}}\,|\nu\rangle\\ &+e^{\frac{i\epsilon_k\tau}{\hbar}}f(\epsilon_k)\,\langle\mu|\,W_k\,|\mu'\rangle\,\langle\mu'|\,e^{-\frac{iH_1\tau}{\hbar}}W_k\,|\xi\rangle\,\langle\xi|\,e^{\frac{iH_0\tau}{\hbar}}\rho_0\,|\nu\rangle).\end{aligned} \tag{4.48}$$

Next, we arrive at the analog of Eq. 4.24,

$$\begin{aligned}\frac{\partial \rho_0^{\mu\nu}}{\partial t} =& \frac{1}{2}\left\langle \mu\right| \left(\{\hat{H}_0^{vib}, \hat{\rho}_0^{vib}\} - \{\hat{\rho}_0^{vib}, \hat{H}_0^{vib}\}\right) \left|\nu\right\rangle \\ &- \frac{i}{\hbar}(U_0^{\mu} - U_0^{\nu})\rho_0^{\mu\nu} \\ &- \frac{\pi}{\hbar}\sum_{k,\mu',\xi} f(U_1^{\mu'} - U_0^{\xi}) \left\langle \mu\right| W_k \left|\mu'\right\rangle \left\langle \mu'\right| W_k \left|\xi\right\rangle \rho_0^{\xi\nu} \\ &- \frac{\pi}{\hbar}\sum_{k,\mu',\xi} \rho_0^{\mu\xi} f(U_1^{\mu'} - U_0^{\xi}) \left\langle \xi\right| W_k \left|\mu'\right\rangle \left\langle \mu'\right| W_k \left|\nu\right\rangle \\ &+ \frac{\pi}{\hbar}\sum_{k,\mu',\nu'} (1 - f(U_1^{\nu'} - U_0^{\nu})) \left\langle \mu\right| W_k \left|\mu'\right\rangle \left\langle \nu'\right| W_k \left|\nu\right\rangle \rho_1^{\mu'\nu'} \\ &+ \frac{\pi}{\hbar}\sum_{k,\mu',\nu'} \rho_1^{\mu'\nu'} (1 - f(U_1^{\mu'} - U_0^{\mu})) \left\langle \mu\right| W_k \left|\mu'\right\rangle \left\langle \nu'\right| W_k \left|\nu\right\rangle .\end{aligned} \tag{4.49}$$

Now, we define a wide-band limit molecule-metal coupling strength that is dependent on the proton vibrational state,

$$\Gamma_{\nu\nu'}^{\mu\mu'} = 2\pi \sum_k \left\langle \mu\right| W_k \left|\mu'\right\rangle \left\langle \nu\right| W_k \left|\nu'\right\rangle \delta(\epsilon - \epsilon_k), \tag{4.50}$$

that when is substituted into Eq. 4.49 yields

$$\begin{aligned}\frac{\partial \rho_0^{\mu\nu}}{\partial t} =& \frac{1}{2}\left\langle \mu\right| \left(\{\hat{H}_0^{vib}, \hat{\rho}_0^{vib}\} - \{\hat{\rho}_0^{vib}, \hat{H}_0^{vib}\}\right) \left|\nu\right\rangle \\ &- \frac{i}{\hbar}(U_0^{\mu} - U_0^{\nu})\rho_0^{\mu\nu} \\ &- \frac{1}{2\hbar}\sum_{\mu',\xi} \Gamma_{\mu'\xi}^{\mu\mu'} f(U_1^{\mu'} - U_0^{\xi}) \rho_0^{\xi\nu} \\ &- \frac{1}{2\hbar}\sum_{\mu',\xi} \Gamma_{\mu'\nu}^{\xi\mu'} \rho_0^{\mu\xi} f(U_1^{\mu'} - U_0^{\xi}) \\ &+ \frac{1}{2\hbar}\sum_{\mu',\nu'} \Gamma_{\nu'\nu}^{\mu\mu'} (1 - f(U_1^{\nu'} - U_0^{\nu})) \rho_1^{\mu'\nu'} \\ &+ \frac{1}{2\hbar}\sum_{\mu',\nu'} \Gamma_{\nu'\nu}^{\mu\mu'} \rho_1^{\mu'\nu'} (1 - f(U_1^{\mu'} - U_0^{\mu})).\end{aligned} \tag{4.51}$$

Finally, taking the secular approximation we arrive at

$$\begin{aligned}\frac{\partial \rho_0^{\mu\mu}}{\partial t} = &\langle \mu | \left(\{ \hat{H}_0^{vib}, \hat{\rho}_0^{vib} \} \right) | \mu \rangle \\ &- \frac{1}{\hbar} \sum_{\mu'} \Gamma_{\mu'\mu}^{\mu\mu'} f(U_1^{\mu'} - U_0^{\mu}) \rho_0^{\mu\mu} \\ &+ \frac{1}{\hbar} \sum_{\mu'} \Gamma_{\mu'\mu}^{\mu\mu'} (1 - f(U_1^{\mu'} - U_0^{\mu})) \rho_1^{\mu'\mu'},\end{aligned} \tag{4.52}$$

which is similar to Eq. 4.26, except $\Gamma \left| F_{\mu \to \mu'} \right|^2$ has been replaced with the more general $\Gamma_{\mu'\mu}^{\mu\mu'}$.

CHAPTER 5

A Grid-free Approach for Simulating Sweep and Cyclic Voltammetry

This chapter is adapted from *J. Chem. Phys.* **154**, 161101 (2021).

5.1. Introduction

5.1.1. Models for Outer-Sphere Electrochemical electron transfer (ET) and Voltammetry

A common experimental technique throughout the field of electrochemistry is sweep voltammetry, where the electrostatic potential of a metal electrode (relative to an electrochemical cell containing an electroactive redox species) is changed with time. The resultant current is usually plotted as a function of this change in driving force[144]. When the potential is ramped in a linear fashion, $E(t) = E_0 + \nu t$, (where ν is the scan rate), the resulting plot is known as a linear sweep voltammetric (LSV) curve. When the scan is carried out in both directions (oxidation and reduction), it is known as cyclic voltammetry (CV). The current in such experiments arise from both (i) the change in the electron transfer (ET) kinetics at the electrode (due to changing the driving force for the ET reaction), and also (ii) diffusional effects which create a concentration gradient of the redox active species in solution. This combination of effects driving the current vs. potential profile makes linear sweep voltammetry an ideal experiment for inferring unknown chemical and physical parameters of interest in the electrochemical system. In particular, nowadays, it is routine to use LSV to infer the diffusion constant of the redox active species[145] or the standard rate constant for an ET reaction, k^0 (the rate constant where the forward and backward rate for the redox reactions are equal)[146].

In order to properly analyze an LSV experiment, one requires a mathematical model with

a reasonable description of both the diffusional and ET effects. Consider the most basic electrochemical reaction, the reduction of a redox species A to its reduced form B,

$$\mathrm{A} + \mathrm{e}^- \underset{\mathrm{k_b}}{\overset{\mathrm{k_f}}{\rightleftharpoons}} \mathrm{B} \quad .$$

where species A exists in bulk solution but, before a reaction, must be brought to the metal surface. For most simulations, diffusional effects are modeled through a standard parabolic, second order partial differential equation (PDE)[50],

$$\begin{aligned} \frac{\partial c_A}{\partial t} &= D_A \frac{\partial^2 c_A}{\partial x^2} \\ \frac{\partial c_B}{\partial t} &= D_B \frac{\partial^2 c_B}{\partial x^2}. \end{aligned} \tag{5.1}$$

Thereafter (and see Eq. 5.8 below), ET effects are incorporated through either a source term in the PDE or electrode boundary conditions. This approach has widespread applicability and can be adadpted to take into account electrical double layer (EDL) effects (which are also called Frumkin corrections to the rate constant that account for uncompensated resistance due to field drop at the point/plane of ET)[147,148], surface adsorption of a species pre-ET[149,150,151,152], coupled homogenous chemical reactions[153,154,155], and many other effects as well. Some of the relevant PDEs can be solved analytically if the ET kinetics are considered to be infinitely fast (i.e. when ET is taken to be instantaneous and dependent upon only the thermodynamics of the redox couple at a given external potential); this is known as the Nernstian limit (again, see below). Realistically, however, most ET kinetics are not infinitely fast and the Nernstian limit is an idealization. In practice, in order to interpret his/her data, the experimentalist will usually need to model voltammetry experiments explicitly, i.e. one requires a computer to solve the necessary PDEs (e.g., in Eq. 5.8) that incorporate (at minimum) both diffusion and a time-dependent ET rate constant.

Finally, for completeness, a few words are appropriate as far as how most electrochemical simulations model electron transfer if one wishes to go beyond the Nernstian limit. In general, there are two common choices for the rate constant: Butler-Volmer (BV) and Marcus-Hush-Chidsey (MHC)[57].

1. One common choice for the ET rate constant is the Butler-Volmer (BV) expression. BV dynamics are characterized by two parameters: the charge transfer coefficient, α, and the standard prefactor k^0. The charge transfer coefficient's physical interpretation has historically been a matter of some debate[156], but mathematically is defined as the change in the log of the current with respect to change in the driving force (in unitless form): $\alpha = \left|\frac{RT}{F}\frac{d\ln I}{dE}\right|$. The total BV forward ($k_f$) and backward ($k_b$) rate constants take the form

$$\begin{aligned} k_f &= k^0 e^{-\alpha\frac{F}{RT}(E-E^{0'})} \\ k_b &= k^0 e^{(1-\alpha)\frac{F}{RT}(E-E^{0'})}, \end{aligned} \tag{5.2}$$

   where $E^{0'}$ is the formal potential (which is dependent on the experimental setup), F is the Faraday constant, and R is the universal gas constant.

2. The other common form for the ET rate constant is the MHC expression. Like BV, MHC can also be characterized by two parameters, the prefactor k^0, and the reorganization energy λ. While the prefactor k^0 has the same interpretation as in BV theory, the reorganization energy λ is defined as the free energy change associated with relaxing the local solvent environment from one configuration (equilibrated to the reactant state) to another configuration (equilibrated to the product state), all the while keeping the molecule's electronic state fixed as the product. Historically, BV theory has been the first choice amongst electrochemists, due in large part to its inherent simplicity and ease of use. However, MHC theory application is now relatively ubiquitous, as it has closer ties to microscopic phenomena and many situations exist where BV theory is incapable of capturing the correct ET behavior[157,158].

   - For homogenous ET in solution, at high temperature, MHC theory is roughly equivalent to transition state theory (insofar as they are exponential in the barrier

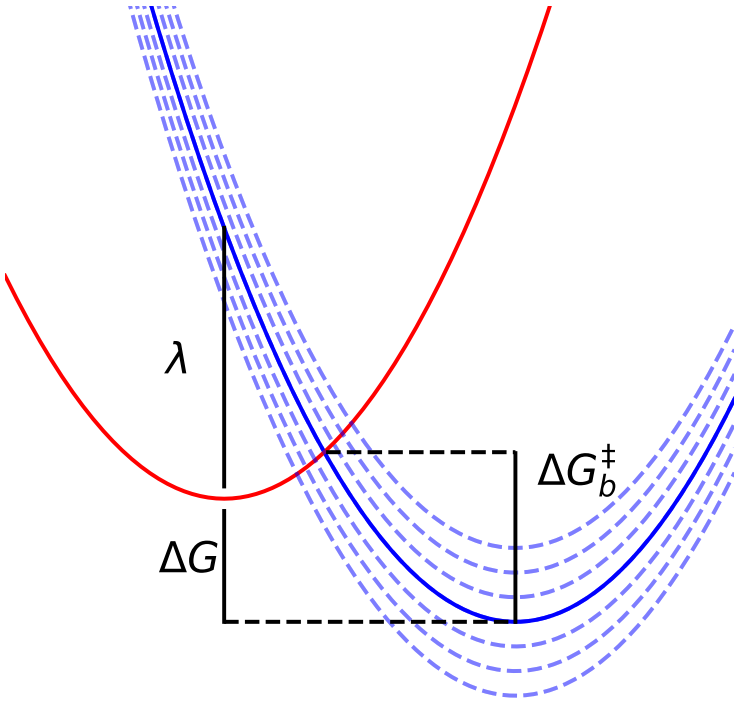

Figure 5.1: The standard harmonic potential energy surfaces over a general solvent reorganization coordinate within the Marcus picture. The red curve represents the charge located on a redox species molecule, while the blue curves represent the charge being located on one of the continuum of possible electronic states that are accessible in the metal electrode. The free energy difference between the charge being located on the molecule versus the metallic state at the fermi level of the metal electrode is given by ΔG, while the reorganization energy (λ) is the energy required to change the relaxed conformation of the redox active species from a local solvent environment of reactant state to the local solvent environment in the product state (all while keeping the charge fixed in the product state). The barrier for transferring an electron from the product to reactant state is also shown, labeled by $\Delta G_b^{\ddagger}$.

height), such that:

$$k = k^0 e^{-\frac{\Delta G^{\ddagger}}{k_B T}} \tag{5.3}$$

where $\Delta G^{\ddagger}$ is the barrier height associated with the transition state, while k_B and T have their usual definitions as the Boltzmann constant and temperature, respectively . While the exact form of k^0 can be a complicated integral expres-

sion and depend on the nature of the reaction (inner or outer sphere)[74], such a distinction will not be relevant for our present purposes. There are multiple analytical series expansions that can be used to calculate the MHC rate constants[58], but these complicated scenarios can often be avoided by assuming symmetric, quadratic free energy surfaces. In practice, if one makes a parabolic free energy assumption, the Marcus rate takes on the famous form:

$$k = k^0 e^{\frac{(\lambda+\Delta G)^2}{4k_B T}}, \tag{5.4}$$

where ΔG is the free energy difference between the electron being located on the acceptor versus the donor.

- For a heterogeneous electrochemical ET, the Marcus rate constant must be modified to account for the fact that the product is no longer a chemical species in solution, but rather a metal electrode with a continuum of electronic states, which obeys an occupancy dictated by a Fermi distribution at a given external potential. By integrating the rate constants over the distribution of electronic states in the electrode, one obtains the so-called MHC rate constant for electrochemical ET[74],

$$\begin{aligned} k_f &= k^0 \int_{-\infty}^{\infty} f(\epsilon) e^{-\frac{\Delta G_f^{\ddagger}(\epsilon)}{RT}} d\epsilon \\ k_b &= k^0 \int_{-\infty}^{\infty} f(-\epsilon) e^{-\frac{\Delta G_b^{\ddagger}(\epsilon)}{RT}} d\epsilon, \end{aligned} \tag{5.5}$$

Here $f(\epsilon) = \frac{1}{1+e^{\beta\epsilon}}$ is the fermi function and $\beta = \frac{1}{k_B T}$.

5.1.2. Adsorptive Effects in Linear Sweep Voltammetry-A First Step Towards Inner-Sphere ET

The above description of ET in LSV experiments is usually sufficient for ET that occurs in solution between redox species. However, if ET occurs between redox species that are adsorbed to the surface of the electrode, many new factors are introduced that complicate the mathematics. These factors include (i) possible changes in the driving force for ET due to the adsorbed species being located within the electrical double layer (EDL); (ii) possibly different reaction mechanisms that can affect both the kinetics and thermodynamics, i.e. inner vs. outer sphere, adiabatic vs. nonadiabatic mechanisms; (iii) the introduction of an additional timescale for mass transfer, i.e. one must now account not only for a species in the bulk approaching the surface, but also for the rate of adsorption and desorption of the oxidized and reduced species (as well as a diffusion times moving along the surface). This list of important focuses at a surface is by no means exhaustive, but these three effects are likely the most important.

Historically, the numerical simulation of adsorption effects in voltammetry experiments has been challenging because adsorption introduces nonlinearity into the differential equation in Eq. 5.1; see Eq. 5.8 below. In order to conceptually separate nonlinear adsorption from the actual ET event, electrochemists have developed a few different model isotherms that quantify what concentration of a species A is expected to be adsorbed on a given surface (Γ_A) given a bulk concentration in solution (c_A). The most common adsorption isotherm is the Langmuir isotherm[159], which assumes that, at high enough solution concentrations, there is a saturating coverage of the electrode (denoted Γ_s). The Langmuir isotherm further assumes that there are no interactions between the species on the electrode surface and that there is no surface heterogeneity. Mathematically, for a single species A, the Langmuir isotherm is given by:

$$\frac{\Gamma_A}{\Gamma_s - \Gamma_A} = \beta_A c_A \Longleftrightarrow \frac{\Gamma_A}{\Gamma_s} = \frac{\beta_A c_A}{1 + \beta_A c_A}, \tag{5.6}$$

where β_A is the equilibrium constant for the adsorption/desorption of A, $\beta_A = \frac{k^A_{ads}}{k^A_{des}}$. For the case of multiple species (for example, A and B, where B is the reduced form of A), the surface concentration of species i ($i = A, B$) can be expressed as

$$\Gamma_i = \frac{\Gamma_s \beta_i c_i}{1 + \beta_i c_i + \sum_{j \neq i} \beta_j c_j} \tag{5.7}$$

More complicated isotherms are sometimes used in the literature, such as the Frumkin isotherm[160] (which allows for interactions between adsorbed species and the surface which can be coverage/concentration dependent). Below, we will present data from only the Langmuir isotherm (though the method itself will be quite general).

5.2. Algorithm

5.2.1. Discretized Method

Before presenting our grid-free approach, we quickly review the standard approach for electrochemical voltammetry in the absence of adsorption. Assuming that all electron transfer occurs only at the boundary, the differential equation for the time evolution of the concentration of each species is:

$$\begin{aligned} \frac{\partial c_A}{\partial t} &= D_A \frac{\partial^2 c_A}{\partial x^2} - (k_f c_A - k_b c_B)\delta(x) \\ \frac{\partial c_B}{\partial t} &= D_B \frac{\partial^2 c_B}{\partial x^2} + (k_f c_A - k_b c_B)\delta(x), \end{aligned} \tag{5.8}$$

Here, c_A and c_B are the normalized concentrations of species A and B, respectively, and D_A and D_B are the diffusion constants for species A and B. The delta function source term is used to enforce that ET occurs only at the solution-electrode interface, defined as $x = 0$.

The equations above are typically solved on a discretized one-dimensional grid. In other words, for a discrete set of points $\{x_1, x_2, ..., x_N\}$ with spacing Δx and a time step Δt, one solves for $c(j\Delta x, k\Delta t)$ in a big loop. In principle, it is usually trivial to solve the differential

equation in Eq. 5.8 using the Euler method with a small enough time step. Unfortunately, however, the ET source terms at the metal electrode (i.e. those terms proportional to $\delta(x)$) usually lead to a myriad of numerical problems for any realistic time discretization (that would certainly dissuade most undergraduates). Moreover, we cannot emphasize enough that electrochemistry occurs over a vast array of time scales. While electron transfer may occur on the time scale of picoseconds, an electrochemical sweep over 1 V with a scan rate of 10mV/s occurs over 100 seconds; one must propagate Eq. 5.8 over an immensely long time range.

The most common solution to such numerical difficulties[50] is to transform the source terms in the above equation into boundary conditions, utilizing a no-flux boundary condition at the electrode surface; for details see Ref. 49. Thereafter, one must still invoke an implicit ODE solver, as the equations are stiff[161]. Alternatively, because the operator on the right hand side of Eq. 5.8 is linear, the simplest approach is to just diagonalize the corresponding (non-Hermitian) operator for diffusion and ET. While diagonalization of a non-Hermitian operator is usually unstable, it is well known that the non-Hermitian diffusion operator (in one dimension) can be transformed into a Hermitian operator[90]. As a result, if one is prepared to work with a grid of points in one-spatial dimension, and one is not concerned with adsoprtion, there are a few numerically stable techniques available as far calculating LSV curves. Our recent work has shown that one can use such a brute force approach to capture more complicated electrochemical scenarios, including proton coupled electon transfer[49,102].

5.2.2. Grid-Free Method

Unfortunately, the methods above face great difficulties when nonlinear adsorption and desorption are considered. On the one hand, the presence of non-linear Langmuir isotherms lead to an even stronger stiffening of the coupled set of PDEs, such that using an implicit differntial equation solver to solve for the dynamics on a grid often fails. On the other hand,

diagonalization is obviously impossible with nonlinear equations of motion. As a result, modeling adsorption is daunting for most parameter sets. The most successful algorithm to date comes from Compton *et al* who have used a spatial grid in a recent article to study phase transitions of adsorbed electroactive species[152].

The goal of the present letter is to present a different solution to this problem, one that completely removes the necessity for a grid in space. In so doing, we will vastly reduce the number of variables that must be propagated in time and, rather than spend time solving the heat equation in solution (and calculating the free solution concentration c_A), we will focus our attention exclusively at the surface where the electron transfer occurs (and calculate the surface concentration Γ_A).

The relevant PDEs

Before outlining our new approach, let us define the differential equations for coupling diffusion, ET, and adsorption that we wish to solve. The PDEs for the solution concentrations (c_A, c_B) take the standard form (following Eq. 5.8 above), with the addition of adsorption/desorption rates, ν_{ads}/ν_{des} at the electrode surface ($x = 0$):

$$\frac{\partial c_A}{\partial t} = D_A \frac{\partial^2 c_A}{\partial x^2} - [(k_f^{sol}(t) c_A - k_b^{sol}(t) c_B) + (\nu_{ads,A} - \nu_{des,A})]\delta(x) \tag{5.9a}$$

$$\frac{\partial c_B}{\partial t} = D_B \frac{\partial^2 c_B}{\partial x^2} + [(k_f^{sol}(t) c_A - k_b^{sol}(t) c_B) - (\nu_{ads,B} - \nu_{des,B})]\delta(x). \tag{5.9b}$$

The ODEs for the surface concentrations, Γ_A and Γ_B involve both electron transfer as well as surface adsorption/desoprtion:

$$\frac{\partial \Gamma_A}{\partial t} = \nu_{ads,A}(t) - \nu_{des,A}(t) - (k_f^{ads}(t)\Gamma_A(t) - k_b^{ads}(t)\Gamma_B(t)) \tag{5.10a}$$

$$\frac{\partial \Gamma_B}{\partial t} = \nu_{ads,B}(t) - \nu_{des,B}(t) + (k_f^{ads}(t)\Gamma_A(t) - k_b^{ads}(t)\Gamma_B(t)). \tag{5.10b}$$

The choice of isotherm will dictate the exact form of ν^i_{ads}/ν^i_{des}; e.g. for the case of a Langmuir isotherm, we choose

$$\nu_{ads,A}(t) = k^A_{ads} c_A(t, x=0)[\Gamma_s - (\Gamma_A(t) + \Gamma_B(t))] \tag{5.11a}$$

$$\nu_{des,A}(t) = k^A_{des}\Gamma_A(t) \tag{5.11b}$$

$$\nu_{ads,B}(t) = k^B_{ads} c_B(t, x=0)[\Gamma_s - (\Gamma_A(t) + \Gamma_B(t))] \tag{5.11c}$$

$$\nu_{des,B}(t) = k^B_{des}\Gamma_B(t). \tag{5.11d}$$

$k^{ads}_f/k^{sol}_f(k^{ads}_b/k^{sol}_b)$ can follow different ET rate laws and are parameterized in different ways (different $\alpha/\lambda, k^0, E^0$, etc.) to reflect the correct underlying physics.

Lastly, when calculating the current, note that in principle there will be separate contributions from both solution and adsorbed ET,

$$I(t) = nFA[(k^{sol}_f(t)c_A(t, x=0) - k^{sol}_b(t)c_B(t, x=0)) + (k^{ads}_f(t)\Gamma_A(t) - k^{ads}_b(t)\Gamma_B(t))], \tag{5.12}$$

where n is the number of electrons, A the surface area of the electrode, and F is the Faraday constant. The time dependence of the rate constants k_f and k_b enters only through their dependencies on the overpotential (which is linearly changed as a function of time in a sweep voltammetry experiment). Formally, the current depends only on four variables at a single time: $c_A(x=0,t), c_B(x=0,t), \Gamma_A(t)$, and $\Gamma_B(t)$.

A Green's Function Approach

Given that $\nu_{ads,i}/\nu_{des,i}$ and $I(t)$ depend only on $c_A(x=0), c_B(x=0), \Gamma_A$, and Γ_B (and specifically not on any of the remaining $c_A(x \neq 0), c_B(x \neq 0)$), our goal is to find a maximally efficient algorithm that tracks only these four values (without tracking the remaining solution concentrations away from the electrode surface). Here, for simplicity, we will assume that species A and B have equal diffusivities ($D_A = D_B$); all of the following results can be simply modified to accommodate unequal diffusion constants, if needed.

Following standard practice in modeling diffusion[50], we will introduce a Green's function formalism in order to integrate Eqs. 5.9 - 5.11 above without a spatial grid. Note that, in the absence of adsorption, Green's functions and Laplace transforms have been used previously by Bazant et al. to model CV curves for the case of thin double sweep voltammetry. In particular, various analytical CV results can be obtained in the Nernstian limit[50,51], especially if one focuses on processes with one ion of interest. Here, we will extend such approaches to the case of several ions with adsorption where no analytic result is possible. We begin by invoking Duhamel's principle[162] to recast our coupled differential equations modeling c_A and c_B as integral equations. For an inhomogeneous diffusion equation of the form Eq. 5.9, with initial and boundary conditions $c_B(t=0,x) = \ c_B(t,x=\pm\infty) = 0$, $c_A(t=0,x) = \ c_A(t,x=\pm\infty) = 1$, one can formally invert these equations of motion to solve for the solution concentration in integral form (we will show c_B, but the derivation is identical for c_A):

$$\begin{aligned} c_B(t,x) &= \int_0^t \int_0^x G(x-y,t-s)[(k_f^{sol}(s)c_A(s,y) - k_b^{sol}(s)c_B(s,y)) - \nu_{ads,B} + \nu_{des,B}]\delta(y)ds\ dy \\ &= \int_0^t \int_0^x G(x-y,t-s)[b(s,y) + a(s)c_B(s,y)]\delta(y)ds\ dy \\ &= \int_0^t G(x,t-s)[b(s,y) + a(s)c_B(s,0)]ds \end{aligned} \tag{5.13}$$

where

$$G(x-y,t-s) = \frac{1}{\sqrt{D_B\pi(t-s)}} e^{-\frac{|x-y|^2}{4(t-s)}} \tag{5.14}$$

is one half of the heat equation Greens function in one dimension[162]. Note that a factor of 2 appears here because the original diffusion equation spans only the half-space $x \in [0,\infty)$.

In Eq. 5.13, the expression for $b(s,y)$ and $a(s)$ are obtained directly from reorganization of

Eq. 5.9; for a Langmuir isotherm, these expressions are

$$\begin{aligned} b(s,y) &= k_f^{sol}(s)c_A(s,y) + k_{des}^B\Gamma_B(s) \\ a(s) &= -(k_b^{sol}(s) + k_{ads}^B[\Gamma_s - (\Gamma_A(s) + \Gamma_B(s))]). \end{aligned} \tag{5.15}$$

Since we are only concerned with the solution concentration at $x = 0$, the equation we wish to numerically solve is given by

$$c_B(t,0) = \int_0^t \frac{1}{\sqrt{D_B\pi(t-s)}}[b(s,0) + a(s)c_B(s,0)]ds. \tag{5.16}$$

We face two challenges to employing Eq. 5.16 to measure electrochemical currents:

1. $b(s,0)$ and $a(s)$ depend on Γ_A, Γ_B, and c_A explicitly, while Γ_A and Γ_B depend explicitly on c_A and c_B.

2. There is a singularity in Eq. 5.16 at $s = t$, which must be carefully accounted for due to the importance of accurate integral evaluation at this point.

Let us begin with the second challenge. To treat the singularity, we cast the integrand in Eq. 5.16 into a general form of $\frac{f(s)}{\sqrt{t-s}}$, where $f(s) = b(s,0) + a(s)c_B(s,0)$. We then break this term into two pieces; $\frac{f(s)-f(t)}{\sqrt{t-s}}$ and $\frac{f(t)}{\sqrt{t-s}}$. The first piece goes to zero at $s = t$, and the second piece can be integrated analytically, removing the singularity. By integrating analytically, the second piece reduces to $2[f(t)\sqrt{t-t} - f(t)\sqrt{t-0}] = -2f(t)\sqrt{t}$. By using nonweighted numerical quadrature (according to the trapezoid rule), one can obtain a numerical prescription for calculating $c_B(t)$ as a function of $b(s,0)$, $a(s)$, and the prior history of c_B (expressed on a grid $[s_1, s_2, ..., s_N]$, with spacing Δs):

$$c_B(t,0) = \frac{\Delta s(\sum_{i=1}^{N-1} \frac{b(s_i,0)+a(s_i)c_B(s_i,0)-b(t,0)}{\sqrt{t-s_i}} + \frac{b(0,0)-b(t,0)}{2\sqrt{t}}) + 2b(t,0)\sqrt{t}}{\sqrt{D_B\pi} - a(t)[2\sqrt{t} - \Delta s(\frac{1}{2\sqrt{t}} + \sum_{i=1}^{N-1} \frac{1}{t-s_i})]}. \tag{5.17}$$

For a derivation, see Appendix I. Note that, in the absence of adsorption, Eq. 5.17 is entirely

sufficient for calculating the current as a function of time/voltage for a sweep voltammetry simulation – without any need for solving an ODE on a discretized grid in space. For instance, suppose that A and B have equal diffusion constants for A and B[163]. In such a case, $c_A(t,0) + c_B(t,0) = c_A(0, x = \infty) + c_B(0, x = \infty) = c_{bulk}$, so that $c_A(t, x = 0)$ can be determined by $c_A(t,0) = c_{bulk} - c_B(t,0)$. Therefore, since k_f^{sol} and k_b^{sol} are analytic expressions (already needed for evaluation of Eq. 5.17), one can easily calculate the current at time t using Eq. 5.12 and 5.17, and thus challenge #1 above disappears[164] . Implementing equation 5.17 is as fast as (or faster than) any implicit ODE based scheme for evaluating equations of the type in Eq. 5.8, and requires no black-box type assumptions that are often inherent when implicitly solving stiff ODEs with common numerical software packages[161].

Next, let us consider the first challenge, i.e. how to self consistently calculate concentrations when there is adsorption of redox active species. In order to simultaneously solve Eq. 5.10 (a standard ODE) and Eq. 5.17 (an integro-differential equation) in coupled fashion, we will apply the procedure below:

1. At $t = dt$, calculate $c_B(0, dt)$ using Eq. 5.17 and the values of Γ_A, Γ_B and c_A at their prior time step values.

2. Calculate $c_A(0, dt)$ using the analogous Eq. 5.17 for c_A, with the value of $c_B(0, dt)$ calculated in step 1 and the values of Γ_A and Γ_B at their prior time step values.

3. Return to step 1-2 until the tolerated convergence is achieved for $c_A(0, dt)$ and $c_B(0, dt)$.

4. Calculate $\Gamma_A(dt)$ and $\Gamma_B(dt)$ using Eq. 5.10 and an implicit ODE solver (in this case, backward differentiation formula of order 5).

5. Return to step 1 of this procedure until simultaneous convergence to a predetermined tolerance is achieved for all four values $c_A(0, dt)$, $c_B(0, dt)$, $\Gamma_A(dt)$, and $\Gamma_B(dt)$ within one single convergence step.

6. Move on to the next time step, repeating steps 1-5 at each time step until the end of

the simulation is reached.

Note that, in step 1) above, for the first guess of Γ_A and Γ_B at a given time step, extrapolation methods can be used to obtain a better initial guess than simply using the prior time step; this usually yields much faster convergence. In our experience, linear extrapolation using two prior times ($\Gamma_A(t) = 2\Gamma_A(t - \delta t) - \Gamma_A(t - 2\delta t)$) yields a substantial improvement in convergence time, while higher order extrapolations do little for accelerating convergence.

In Fig. 5.2 we show a set of illustrative examples of CVs generated with this methodology, both in the case (a) without and (b) with adsorptive effects. From the voltamogramms in Fig. 5.2(a) without adsorption, at low scan rate we see the expected peak separation of 57 mV for a reversible ET reaction in solution, and the peak separation increases slightly as the scan rate increases and approaches the irreversible ET regime. Conversely, in Fig. 5.2(b), we see no peak separation in the case where ET occurs between surface bound species, as expected[50]. These results demonstrate that the above algorithm can capture the behavior of both coupled mass and electron transfer in solution and at surface bound electrochemical interfaces under a sweeping potential. Unfortunately, these simulations should also make clear that any attempt to invert[165] a voltammogram to back out the relevant parameters in Eqs. 5.9 - 5.11 would be extremely difficult.

Additionally, to demonstrate the computational benefit of the present algorithm, below we show two tables illustrating the computational improvement of this method. Table 5.1 shows computation times for the results shown in Fig. 5.2, where we see that this present algorithm is relatively invariant to scan rate – even with adsorption. This behavior stands in contrast to the typical grid based ODE methods, which can require longer times at smaller scan rates, as more time is needed to propagate dynamics using an implicit ODE solver in order to cover a given potential range. Lastly, Table 5.2 below shows the relative improvement in computation time for the present algorithm as compared to the more traditional approach where one solves the spatial grid-based coupled ODEs through discretization of the relevant propagator over a set of grid points and diagonalization of the diffusion operator[49]. Similar

to the above argument about scan rate for traditional grid based methods, more spatial points implies larger computational cost, whereas for the method outlined in present paper, no such discretization is required as there is no added computational cost. All simulations were performed in Python, using the NumPy and SciPy libraries, on a 2.8 GHz Dual-Core Intel Core i5 processor with 16 GB of RAM.

Table 5.1: Computational wall time by method (Python)

Scan rate (V/sec)	No adsorption	Adsorption
0.05	3.70 s	22.06 s
0.1	4.89s	21.13 s
1	3.40 s	20.54 s
5	3.67 s	19.87 s

Table 5.2: Computation time by method (Python)

Algorithm	wall time
Grid-free	2.34 s
Discretized, $N_x = 50$	9.94 s
Discretized, $N_x = 100$	30.91 s
Discretized, $N_x = 200$	83.02 s

5.3. Conclusion

In this article, as an alternative to traditional grid based methods, we have introduced an integral based approach for simulating electrochemical ET to model ET along with adsorption of redox species. Our approach is in quantitative agreement with grid based PDE solutions for a single ET experiment; more generally, however, the present algorithm should allow us to simulate more complicated sweep experiments that involve adsorption kinetics and beyond. Code implementing this algorithm can be found at https://github.com/alecja/electrochemistry_sim. Looking forward, one can imagine several applications of the present methodology. First, one would like to study the various parameter regimes of electrochemical voltammetry experiments where adsorption plays a key role. After all, the addition of another timescale/parameter set corresponding to adsorption/desorption rates, plus the potential asymmetry in redox behavior of charge/uncharged species on a

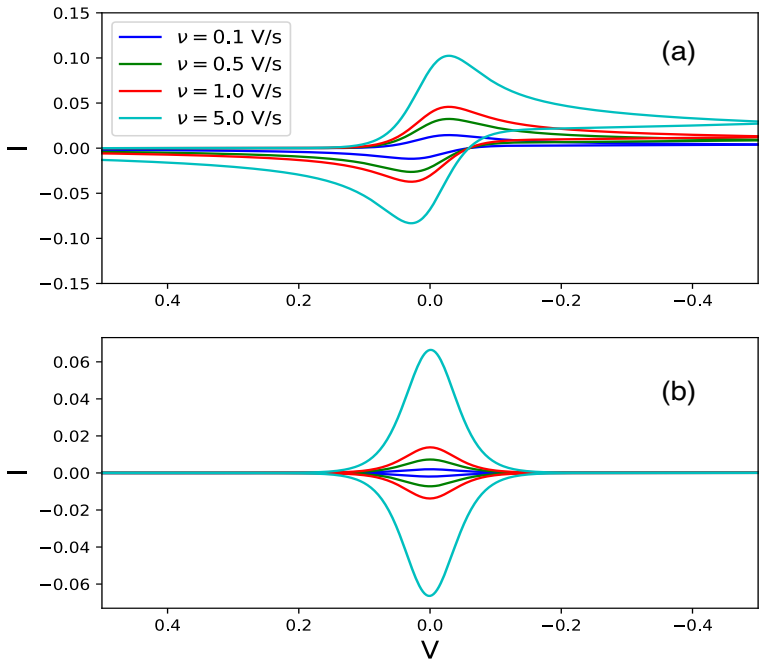

Figure 5.2: Example CVs using the above method for at various scan rates, for the case with (a) no adsorption and (b) with adsorption. The units for current here are $\frac{I}{nFA}$, while V is in volts. Mathematically, "no adsorption" means simulations using only Eq. 5.9 and not Eq. 5.10, i.e. ν_{ads} and ν_{des} are set to zero. "With adsorption" implies using both Eqs. 5.9 and 5.10, with k_f^{sol} and k_b^{sol} set to zero. The parameters for these simulations are $D = 5.5 \cdot 10^{-4}$ cm^2/sec, $T = 300$ K, $N_T = 500$, $k_0 = 10^5$ cm/sec, $\alpha = 0.5$ (BV kinetics are used for ET). Wall times for each simulation can be found in Table 5.2.

surface, implies that a realistic description of electrochemical dynamics and kinetics can and must go beyond the standard Nernstian and irreversible regimes that we have all grown up with. Second, one can imagine extending the present methodology to two and three dimensional surfaces, investigating how geometry and defects in the electrode surface affect current; indeed previous work with diagonalization have precluded such large scale simulation, but Green's function techniques in three dimensions have proven successful as far

as modeling heat transfer in environments with finite domains[165]. Third and finally, integrating the present diffusion equations with microscopic (atomistic) models of interfaces remains very difficult, especially if one wishes to construct ab initio models of bond-making and bond-breaking electrochemistry, and for maximum impact, the present algorithm will certainly need to be extended to far larger simulations with more intermediates and even more dynamical time scales.

5.4. Acknowledgements

This work was supported by the U.S. Air Force Office of Scientific Research (USAFOSR) under Grant Nos. FA9550-18-1-0497 and FA9550-18-1-0420, and the National Science Foundation under Grant No. DMS-2012286.

5.5. Data Availability

The data that support the findings of this study are available within the article.

5.6. Appendix I: Derivation of Equation 5.17

Below we will carry out a general derivation of Eq. 5.17 from Eq. 5.16, for either species A or B, with arbitrary initial conditions. We first break the integrand into two pieces, $\frac{f(s)-f(t)}{\sqrt{t-s}}$ and $\frac{f(t)}{\sqrt{t-s}}$, where $f(s) = b(s,0) + a(s)c_j(s,0)$. The first integral is evaluated using the trapezoidal rule, while the second integral is evaluated analytically:

$$\begin{aligned} c_j(t,0) = c_j(0,0) + (D_j\pi)^{-0.5}[&\int_0^t \frac{[b(s,0)+a(s)c_j(s,0)] - [b(t,0)+a(t)c_j(t,0)]}{\sqrt{t-s}} ds + \\ &\int_0^t \frac{[b(t,0)+a(t)c_j(t,0)]}{\sqrt{t-s}} ds] \\ c_j(t,0) = c_j(0,0) + (D_j\pi)^{-0.5}[&\Delta s(\sum_{i=i}^{N-1} \frac{b(s_i,0)+a(s_i)c_j(s_i,0) - b(t,0) - a(t)c_j(t,0)}{\sqrt{t-s_i}} + \\ &\frac{b(0,0) - b(t,0) + a(0)c_j(0,0) - a(t)c_j(t,0)}{2\sqrt{t}}) + 2\sqrt{(}t)(b(t,0)+a(t,0)c_j(t,0))]. \end{aligned} \tag{5.18}$$

Rearrangement of all $c_j(t,0)$ terms to the left hand side yields

$$c_j(t,0)[\sqrt{D_j\pi} - 2a(t)\sqrt{t} + \Delta s(\sum_{i=1}^{N-1} \frac{a(t)}{\sqrt{t-s_i}} + \frac{a(t)}{2\sqrt{t}})] - c_j(0,0)\sqrt{D_j\pi} =$$
$$\Delta s(\sum_{i=1}^{N-1} \frac{b(s_i,0) + a(s_i)c_j(s_i,0) - b(t,0)}{\sqrt{t-s_i}} + \frac{0.5(b(0,0) - b(t,0) + a(0)c_j(0,0))}{\sqrt{t}}) + 2b(t,0)\sqrt{t}. \tag{5.19}$$

Finally, isolation of $c_j(t,0)$ yields the final result,

$$c_j(t,0) = \frac{\Delta s(\sum_{i=1}^{N-1} \frac{b(s_i,0)+a(s_i)c_j(s_i,0)-b(t,0)}{\sqrt{t-s_i}} + \frac{b(0,0)-b(t,0)+a(0)c_j(0,0)}{2\sqrt{t}}) + 2b(t,0)\sqrt{t} + c_j(0,0)\sqrt{D_j\pi}}{\sqrt{D_j\pi} - a(t)[2\sqrt{t} - \Delta s(\sum_{i=1}^{N-1} \frac{1}{\sqrt{t-s_i}} + \frac{1}{2\sqrt{t}})]} \tag{5.20}$$

Note that Eq. 5.17 is recovered exactly when the index j is replaced with B and the initial condition $c_B(0,0) = 0$ is substituted.

CHAPTER 6

Conclusion

Throughout this dissertation we have presented new approaches for simulating and modeling nonadiabatic dynamics in electrochemical systems. In chapter 2, we examined whether electronic friction with Langevin dynamics in general can capture nonadiabatic effects in molecule-metal systems. We found in this work that, in general, electronic friction is insufficient for capturing nonadiabatic effects in these systems, and that future work would require a broadened classical master equation, solved with surface hopping. In chapter 3 we illustrated how to simulate diffusive electrochemical systems using a surface hopping approach that is identical to traditional methods in electrochemistry, but affords more flexibility in simulating complicated, higher dimensional systems. In chapter 4 we extended the methodology from chapter 3 to systems that contain nuclear quantum effects, specifically proton-coupled electron transfer (PCET), and showed that traditional voltammetry experiments would be insufficient for completely understanding systems that undergo PCET. In chapter 5, we presented a computational approach for simulating electrochemical systems that exhibit complicated dynamics, such as adsorption, in a (spatial) grid-free manner, opening up future avenues for more readily simulating and modeling these systems.

Looking forward, the next logical step is to extend the above methods and algorithms to studying real-world electrochemical systems, with parameters obtained from *ab-initio* simulations. These simulations are very expensive computationally, but nuanced application of statistical approaches could allow for molecular level parameter inferences that could, in tandem with the above methods, yield new insights into realistic electrochemical systems. Additionally, there still remain effects in electrochemical voltammetry which could stand to be modeled at a higher level. Acid-base effects in electrochemical voltammetry are notoriously hard to model to a high level, and approaches detailed within this dissertation could reasonably be extended to incorporate effects of this nature.

BIBLIOGRAPHY

[1] J. C. Tully, J. Chem. Phys. **93**, 1061 (1990).

[2] W. Dou and J. E. Subotnik, J. Chem. Phys. **146**, 092304 (2017).

[3] W. Dou, G. Miao, and J. E. Subotnik, Phys. Rev. Lett. **119**, 046001 (2017).

[4] W. Dou and J. E. Subotnik, Phys. Rev. B **96**, 104305 (2017).

[5] W. Ouyang, W. Dou, A. Jain, and J. E. Subotnik, J. Chem. Theory Comput. **12**, 4178 (2016).

[6] M. Silva, R. Jongma, R. W. Field, and A. M. Wodtke, Annu. Rev. Phys. Chem. **52**, 811 (2001).

[7] A. M. Wodtke, J. C. Tully, and D. J. Auerbach, Int. Rev. Phys. Chem. **23**, 513 (2004).

[8] O. Bunermann, H. Jiang, Y. Dorenkamp, A. Kandratsenka, S. M. Janke, D. J. Auerbach, and A. M. Wodtke, Science **350**, 1346 (2015).

[9] B. C. Krüger, S. Meyer, A. Kandratsenka, A. M. Wodtke, and T. Schäfer, J. Phys. Chem. Lett. **7**, 441 (2016).

[10] A. M. Wodtke, Chem. Soc. Rev. **45**, 3641 (2016).

[11] S. Gosavi and R. Marcus, J. Phys. Chem. B **104**, 2067 (2000).

[12] J. H. Mohr and W. Schmickler, Phys. Rev. Lett. **84**, 1051 (2000).

[13] S. Hammes-Schiffer and A. V. Soudackov, J. Phys. Chem. B **112**, 14108 (2008).

[14] W. Ouyang, J. G. Saven, and J. E. Subotnik, J. Phys. Chem. C **119**, 20833 (2015).

[15] Y. Huang, C. T. Rettner, D. J. Auerbach, and A. M. Wodtke, Science **290**, 111 (2000).

[16] C. Bartels, R. Cooper, D. J. Auerbach, and A. M. Wodtke, Chem. Sci. **2**, 1647 (2011).

[17] W. Dou, A. Nitzan, and J. E. Subotnik, J. Chem. Phys. **142**, 084110 (2015).

[18] W. Dou, A. Nitzan, and J. E. Subotnik, J. Chem. Phys. **143**, 054103 (2015).

[19] E. G. D'Agliano, P. Kumar, W. Schaich, and H. Suhl, Phys. Rev. B **11**, 2122 (1975).

[20] M. Head-Gordon and J. C. Tully, J. Chem. Phys. **96**, 3939 (1992).

[21] M. Head-Gordon and J. C. Tully, J. Chem. Phys. **103**, 10137 (1995).

[22] M. S. Mizielinski, D. M. Bird, M. Persson, and S. Holloway, J. Chem. Phys. **122**, 084710 (2005).

[23] M. S. Mizielinski, D. M. Bird, M. Persson, and S. Holloway, J. Chem. Phys. **126**, 034705 (2007).

[24] B. B. Smith and J. T. Hynes, J. Chem. Phys. **99**, 6517 (1993).

[25] V. Krishna, J. Chem. Phys. **125**, 034711 (2006).

[26] M. Plihal and D. Langreth, Phys. Rev. B **58**, 2191 (1998).

[27] M. Plihal and D. Langreth, Phys. Rev. B **60**, 5969 (1999).

[28] N. Bode, S. V. Kusminskiy, R. Egger, and F. von Oppen, Beilstein J. Nanotechnol. **3**, 144 (2012).

[29] M. Thomas, T. Karzig, S. V. Kusminskiy, G. Zaránd, and F. Von Oppen, Phys. Rev. B **86**, 195419 (2012).

[30] M. Galperin and A. Nitzan, J. Phys. Chem. Lett. **6**, 4898 (2015).

[31] M. Brandbyge, P. Hedegård, T. F. Heinz, J. A. Misewich, and D. M. Newns, Phys. Rev. B **52**, 6042 (1995).

[32] J. Daligault and D. Mozyrsky, Phys. Rev. E **75**, 026402 (2007).

[33] D. Mozyrsky, M. B. Hastings, and I. Martin, Phys. Rev. B **73**, 035104 (2006).

[34] C. Martens and J.-Y. Fang, J. Chem. Phys. **106**, 4918 (1997).

[35] R. Kapral and G. Ciccotti, J. Chem. Phys. **110**, 8919 (1999).

[36] V. Romero-Rochin, A. Orsky, and I. Oppenheim, Physica A **156**, 244 (1989).

[37] V. Romero-Rochin and I. Oppenheim, Physica A **155**, 52 (1989).

[38] W. Dou and J. E. Subotnik, J. Chem. Phys. **144**, 024116 (2016).

[39] N. Shenvi, S. Roy, and J. C. Tully, J. Chem. Phys. **130**, 174107 (2009).

[40] N. Shenvi, S. Roy, and J. C. Tully, Science **326**, 829 (2009).

[41] S. Li and H. Guo, J. Chem. Phys. **117**, 4499 (2002).

[42] S. Monturet and P. Saalfrank, Phys. Rev. B **82**, 075404 (2010).

[43] S. P. Rittmeyer, J. Meyer, J. I. Juaristi, and K. Reuter, Phys. Rev. Lett. **115** (2015).

[44] G. Miao, W. Dou, and J. E. Subotnik, J. Chem. Phys. **147**, 224105 (2017).

[45] T. Holstein, Ann. Phys. - New York **8**, 343 (1959).

[46] P.W. Anderson, Phys. Rev. **124**, 41 (1961).

[47] R. Zwanzig, *Nonequilibrium statistical mechanics* (Oxford University Press, 2001).

[48] There is a curious result in Fig. 2.2(a) in the case of $K = 0.001$. Here, we see that the ratio of the SH rate over the EF-LD rate is maximized when $\Gamma_0 = 0.1$ and then decreases again as Γ_0 decreases further. This state of affairs is actually consistent with the other data provided in the body of this paper. A detailed analysis shows that, for $K = 0.001$, the surface hopping distribution is more bimodal at $\Gamma_0 = 0.1$ and less bimodal at $\Gamma_0 = 0.01$.

[49] A. J. Coffman, A. K. Harshan, S. Hammes-Schiffer, and J. E. Subotnik, J. Phys. Chem. C **123**, 13304 (2019).

[50] A. J. Bard and L. R. Faulkner, *Electrochemical Methods: Fundamentals and Applications* (Wiley, New York, 2001).

[51] D. Yan, M. Z. Bazant, P. M. Biesheuvel, M. C. Pugh, and F. P. Dawson, Phys. Rev. E **95** (2017).

[52] J. F. Smalley, C. E. D. Chidsey, S. E. Creager, J. P. Ferraris, H. O. Finklea, K. Chalfant, T. Zawodzinsk, M. D. Newton, S. W. Feldberg, and M. R. Linford, J. Am. Chem. Soc. **125**, 2004 (2003).

[53] S. W. Feldberg, Anal. Chem. **82**, 5176 (2010).

[54] M. C. Henstridge, E. Laborda, N. V. Rees, and R. G. Compton, Electrochim. Acta **84**, 12 (2012).

[55] E. Laborda, M. C. Henstridge, C. Batchelor-McAuley, and R. G. Compton, Chem. Soc. Rev. **42**, 4894 (2013).

[56] D. V. Matyushov and M. D. Newton, Phys. Chem. Chem. Phys. **20**, 24176 (2018).

[57] K. B. Oldham and J. C. Myland, J. Electroanal. Chem. **655**, 65 (2011).

[58] A. Migliore and A. Nitzan, J. Electroanal. Chem. **671**, 99 (2012).

[59] M. C. Henstridge, E. Laborda, Y. Wang, D. Suwatchara, N. Rees, Á. Molina, F. Martínez-Ortiz, and R. G. Compton, J. Electroanal. Chem. **672**, 45 (2012).

[60] M. C. Henstridge, E. Laborda, E. J. F. Dickinson, and R. G. Compton, J. Electroanal. Chem. **664**, 73 (2012).

[61] E. E. Tanner, L. Xiong, E. O. Barnes, and R. G. Compton, J. Electroanal. Chem. **727**, 59 (2014).

[62] Y. Okajima, Y. Shibuta, and T. Suzuki, Comput. Mater. Sci. **50**, 118 (2010).

[63] E. Skúlason, V. Tripkovic, M. E. Björketun, S. Gudmundsdóttir, G. Karlberg, J. Rossmeisl, T. Bligaard, H. Jónsson, and J. K. Nørskov, J. Phys. Chem. C **114**, 18182 (2010).

[64] A. Roldan, Curr. Opin. Electrochem. **10**, 1 (2018).

[65] L. D. Zusman, Chem. Phys. **49**, 295 (1980).

[66] I. Rips and J. Jortner, J. Chem. Phys. **87**, 2090 (1987).

[67] J. E. Straub and B. J. Berne, J. Chem. Phys. **87**, 6111 (1987).

[68] D. V. Matyushov and R. Schmid, J. Phys. Chem. **98**, 5152 (1994).

[69] R. C. Dorfman and M. D. Fayer, J. Chem. Phys. **96**, 7410 (1992).

[70] V. S. Gladkikh, A. I. Burshtein, H. L. Tavernier, and M. D. Fayer, J. Phys. Chem. A **106**, 6982 (2002).

[71] V. Gladkikh, A. I. Burshtein, S. V. Feskov, A. I. Ivanov, and E. Vauthey, J. Chem. Phys. **123**, 4894 (2005).

[72] P. Bai and M. Z. Bazant, Nat. Commun. **5**, 3585 (2014).

[73] S. K. Reed, P. A. Madden, and A. Papadopoulos, J. Chem. Phys. **128**, 124701 (2008).

[74] W. Schmickler and E. Santos, *Interfacial Electrochem.* (Springer-Verlag Berlin Heidelberg, 2010).

[75] J. E. Randles, Trans. Faraday Soc. **44**, 327 (1948).

[76] A. Ševčík, Collect. Czechoslov. Chem. Commun. **13**, 349 (1948).

[77] R. S. Nicholson and I. Shain, Anal. Chem. **36**, 706 (1964).

[78] H. Matsuda and Y. Ayabe, Z. Electrochem **59**, 494 (1955).

[79] R. S. Nicholson, Anal. Chem. **37**, 1351 (1965).

[80] J. C. Myland and K. B. Oldham, J. Electroanal. Chem. **153**, 43 (1983).

[81] Interestingly, although this manuscript will not address dynamics in the adiabatic representation, for E defined in equation 3.9, if one commits to the adiabatic representation, the electronic friction tensor here arises exclusively from non-Condon effects (i.e. the electronic friction tensor is proportional to $\frac{\partial \Gamma}{\partial \vec{r}}$). For details, see Ref. 2.

[82] In other words, for SH, the relevant boundary conditions are $\frac{\partial c_A}{\partial x}|_{x=0^-} = \frac{\partial c_B}{\partial x}|_{x=0^-}$.

[83] R. A. Marcus, J. Chem. Phys. **43**, 679 (1965).

[84] R. G. Compton, E. Laborda, and K. R. Ward, *Understanding Voltammetry* (Imperial College Press, 2014).

[85] W. H. Press, S. A. Teukolsky, W. T. Vetterling, and B. P. Flannery, *Numerical Recipes in C : The Art of Scientific Computing* (Cambridge University Press, 1992).

[86] T. E. Hull, W. H. Enright, B. M. Fellen, and A. E. Sedgwick, SIAM J. Numer. Anal. **9**, 603 (1972).

[87] P. N. Brown, G. D. Byrne, and A. C. Hindmarsh, SIAM J. Sci. Stat. Comput. **10**, 1038 (1989).

[88] Note that the mathematics in this section can be safely skipped by the reader who is not concerned about the stability of diagonalizing a non-Hermitian matrix. For the practical reader who wants to repeat our calculations, however, these details will be essential.

[89] Y. J. Jung and J. Cao, J. Chem. Phys. **117**, 3822 (2002).

[90] H. Risken, *The Fokker-Planck Equations, Method of Solution and Applications*, 2nd ed. (Springer-Verlag, 1989) p. 103.

[91] In this paper, if we don't use enough grid points, we must sometimes force the lowest eigenvalue to be equal to zero for numerical stability.

[92] The transfer coefficient α represents the slope of the log current with respect to the external potential, ΔG, at zero external potential, i.e. $\alpha = -kT\frac{\partial log(I)}{\partial \Delta G}|_{\Delta G = \Delta G^\circ}$ [74].

[93] Note that this long time simulation is not equivalent to a Tafel measurement. For the present paper, we allow the concentrations of A and B to change at the electrode surface subject to diffusion, as to study the effect of mass transfer on the voltammetry curves. By contrast, for a Tafel plot, one works under the assumption that the concentrations of A and B are largely fixed at the electrode surface and are not affected by diffusion.

[94] M. Rudolph, J. Electroanal. Chem. **529**, 97 (2002).

[95] M. Rudolph, J. Electroanal. Chem. **543**, 23 (2003).

[96] M. Rudolph, J. Electroanal. Chem. **571**, 289 (2004).

[97] M. Rudolph, J. Comput. Chem. **26**, 619 (2005).

[98] M. Rudolph, J. Comput. Chem. **26**, 633 (2005).

[99] M. Rudolph, J. Comput. Chem. **26**, 1193 (2005).

[100] M. Rudolph, D. P. Reddy, and S. W. Feldberg, Anal. Chem. **66**, 589 (1994).

[101] H. B. Keller and V. Pereyra, Math. Comput. **32**, 955 (1978).

[102] A. J. Coffman, W. Dou, S. Hammes-Schiffer, and J. E. Subotnik, J. Chem. Phys. **152**, 234108 (2020).

[103] G. Herzberg, *Molecular spectra and molecular structure,* (Van Nostrand, New York, 1950).

[104] H. Sumi and R. A. Marcus, J. Chem. Phys. **84**, 4894 (1986).

[105] J. Lappe and R. J. Cave, J. Phys. Chem. A **104**, 2294 (2000).

[106] X. Sun and E. Geva, J. Phys. Chem. A **120**, 2976 (2016).

[107] E. Buhks, M. Bixon, J. Jortner, and G. Navon, J. Phys. Chem. **85**, 3759 (1981).

[108] J. A. V. Butler, Proc. R. Soc. London. Ser. A - Math. Phys. Sci. **157**, 423 (1936).

[109] D. M. Newns, Phys. Rev. **178**, 1123 (1969).

[110] W. Schmickler, J. Electroanal. Chem. **204**, 31 (1986).

[111] A. Soudackov and S. Hammes-Schiffer, J. Chem. Phys. **111**, 4672 (1999).

[112] A. Soudackov and S. Hammes-Schiffer, J. Chem. Phys. **113**, 2385 (2000).

[113] A. Soudackov, E. Hatcher, and S. Hammes-Schiffer, J. Chem. Phys. **122**, 014505 (2005).

[114] J. Grimminger, S. Bartenschlager, and W. Schmickler, Chem. Phys. Lett. **416**, 316 (2005).

[115] D. R. Weinberg, C. J. Gagliardi, J. F. Hull, C. F. Murphy, C. A. Kent, B. C. Westlake, A. Paul, D. H. Ess, D. G. McCafferty, and T. J. Meyer, Chem. Rev. **112**, 4016 (2012).

[116] M. T. Koper, Chem. Sci. **4**, 2710 (2013).

[117] C. Costentin and J. M. Savéant, J. Am. Chem. Soc. **139**, 8245 (2017).

[118] P. Goyal and S. Hammes-Schiffer, J. Phys. Chem. Lett. **6**, 3515 (2015).

[119] P. Goyal, C. A. Schwerdtfeger, A. V. Soudackov, and S. Hammes-Schiffer, J. Phys. Chem. B **120**, 2407 (2016).

[120] K. Song and Q. Shi, J. Chem. Phys. **146**, 184108 (2017).

[121] P. Goyal and S. Hammes-Schiffer, Proc. Natl. Acad. Sci. U. S. A. **114**, 1480 (2017).

[122] A. Mandal, F. A. Shakib, and P. Huo, J. Chem. Phys. **148**, 244102 (2018).

[123] S. Ghosh, J. Castillo-Lora, A. V. Soudackov, J. M. Mayer, and S. Hammes-Schiffer, Nano Lett. **17**, 5762 (2017).

[124] C. Venkataraman, A. V. Soudackov, and S. Hammes-Schiffer, J. Phys. Chem. C **112**, 12386 (2008).

[125] M. T. Huynh, S. J. Mora, M. Villalba, M. E. Tejeda-Ferrari, P. A. Liddell, B. R. Cherry, A. L. Teillout, C. W. MacHan, C. P. Kubiak, D. Gust, T. A. Moore, S. Hammes-Schiffer, and A. L. Moore, ACS Cent. Sci. **3**, 372 (2017).

[126] W. Dou and J. E. Subotnik, J. Chem. Phys. **144**, 024116 (2016).

[127] H_{sys} can also be expressed in second quantized notation, as $H_{sys} = \sum_{\mu} U_0^{\mu}(\mathbb{1} - d^{\dagger}d)a_{\mu}^{\dagger}a_{\mu} + \sum_{\mu'} U_1^{\mu'} d^{\dagger}d \; a_{\mu'}^{\dagger}a_{\mu'} + H_{ph}$, where $a_{\mu}(a_{\mu}^{\dagger})$ are annihilation (creation) operators for the proton vibrational state μ, and $\mathbb{1}$ is the identity operator.

[128] K. Blum, *Density matrix theory and applications*, 3rd ed. (Springer-Verlag Berlin Heidelberg, 2012).

[129] For a previous application of the QME to photo-induced PCET, see Refs. 166 and 167.

[130] W. Dou and J. E. Subotnik, J. Chem. Phys. **144**, 024116 (2016).

[131] I. Navrotskaya, A. V. Soudackov, and S. Hammes-Schiffer, J. Chem. Phys. **128**, 244712 (2008).

[132] Of course, W_k must depend strongly on x, and it is for this reason that we allow hopping only at the $x = 0$ grid point. Moreover, in Ref. 49, it was shown that, as long as the coupling decays quickly with distance from the electrode (e.g. exponentially), we can incorporate an x-dependence in the coupling by integrating over the relevant hopping regime and redefining the hopping rate at the first grid point in x. In practice, for any reasonably spaced uniform grid (which is usually on the order of microns), all relevant hopping should be only at the first grid point.

[133] C. Venkataraman, A. V. Soudackov, and S. Hammes-Schiffer, J. Phys. Chem. C **112**, 12386 (2008).

[134] Z. Zhou, H.-T. Chen, A. Nitzan, and J. E. Subotnik, JCTC **16**, 821 (2020).

[135] We note that recent work by Matyushov and Newton[168] has shown that nonergodic effects due to a slowly relaxing medium (of comparable order to the reaction time) can play a significant role in electrochemical ET, by reducing the solvent reorganization energy below its thermodynamic limit from Marcus theory. This effect is mainly noticeable in electrochemical ET, due to the multiple orders of magnitude in rates covered over the course of the entire potential sweep. While we do not account for this effect in our framework, this observation provides an additional way that one could fine tune the above model, by incorporating an overpotential dependence into λ.

[136] For a more rigorous justification for this choice of electrode boundary condition, see Ref. 49.

[137] J. Koch, F. Von Oppen, Y. Oreg, and E. Sela, Phys. Rev. B - Condens. Matter Mater. Phys. **70**, 1 (2004).

[138] J. Koch, M. Semmelhack, F. Von Oppen, and A. Nitzan, Phys. Rev. B - Condens. Matter Mater. Phys. **73**, 155306 (2006).

[139] J. P. Dahl and M. Springborg, J. Chem. Phys. **88**, 4535 (1988).

[140] A. Migliore, N. F. Polizzi, M. J. Therien, and D. N. Beratan, Chem. Rev. **114**, 3381 (2014).

[141] A. V. Soudackov and S. Hammes-Schiffer, J. Chem. Phys. **143**, 194101 (2015).

[142] Z. K. Goldsmith, A. V. Soudackov, and S. Hammes-Schiffer, Faraday Discuss. **216**, 363 (2019).

[143] Despite not being shown here, the choice of parameters a_4 and a_2 can also change the observed IV behavior, but do not have as simple of physical intuition as the a_1 parameters with regards to the shape of the proton PESs for electronic states A and B. Thus, we have chosen to show only the a_1 dependence, as this illustrates qualitatively how the quartic oscillator shows similar current versus potential trends as the other oscillators examined.

[144] N. Elgrishi, K. J. Rountree, B. D. McCarthy, E. S. Rountree, T. T. Eisenhart, and J. L. Dempsey, J. Chem. Educ. **95**, 197 (2018).

[145] M. Bogdan, D. Brugger, W. Rosenstiel, and B. Speiser, J. Cheminform. **6** (2014).

[146] E. P. Randviir, Electrochim. Acta **286**, 179 (2018).

[147] M. Van Soestbergen, Russ. J. Electrochem. **48**, 570 (2012).

[148] A. M. Limaye and A. P. Willard, J. Phys. Chem. C **124**, 1352 (2020).

[149] C. Lin, C. Batchelor-McAuley, E. Laborda, and R. G. Compton, J. Phys. Chem. C **119**, 22415 (2015).

[150] A. J. Samin, AIP Adv. **6** (2016).

[151] M. Yang and R. G. Compton, J. Electroanal. Chem. **836**, 68 (2019).

[152] M. Yang and R. G. Compton, J. Phys. Chem. C **124**, 18031 (2020).

[153] T. V. Shea and A. J. Bard, Anal. Chem. **59**, 2101 (1987).

[154] A. W. Bott, Curr. Sep. **18**, 9 (1999).

[155] H. Chen, J. R. Elliott, H. Le, M. Yang, and R. G. Compton, J. Electroanal. Chem. **869** (2020).

[156] R. Guidelli, R. G. Compton, J. M. Feliu, E. Gileadi, J. Lipkowski, W. Schmickler, and S. Trasatti, *Pure Appl. Chem.*, (2014).

[157] M. J. Honeychurch, Langmuir **15**, 5158 (1999).

[158] C. Léger and P. Bertrand, *Chem. Rev.*, **108**, 2379 (2008).

[159] I. Langmuir, J. Am. Chem. Soc. **40**, 1361 (1918).

[160] A. N. Frumkin, J. Electroanal. Chem. **7**, 152 (1964).

[161] A. C. Hindmarsh, P. N. Brown, K. E. Grant, S. L. Lee, R. Serban, D. E. Shumaker, and C. S. Woodward, ACM Trans. Math. Softw. **31**, 363 (2005).

[162] F. John, *Partial Differential Equations*, Applied Mathematical Sciences, Vol. 1 (Springer US, New York, NY, 1978).

[163] When $D_A \neq D_B$, then one must use the more strict condition that there is no net flux $D_A \frac{dc_A}{dx} = -D_B \frac{dc_B}{dx}$, which implies $D_A c_A = D_B c_B$ is a constant in space.

[164] Eq. 5.17 can be written as $c_B(t,0) = \zeta_B + \chi_B c_A(t,0)$, where ζ_B and χ_B are defined appropriately. An analogous equation holds for c_A, $c_A(t,0) = \zeta_A + \chi_A c_B(t,0)$. Overall, these two equations can be recast as a matrix equation of the form $\begin{pmatrix} 1 & -\chi_A \\ -\chi_B & 1 \end{pmatrix} \begin{pmatrix} c_A \\ c_B \end{pmatrix} = \begin{pmatrix} \zeta_A \\ \zeta_B \end{pmatrix}$. To speed up convergence in steps 1 and 2, such a matrix equation can be solved exactly to yield solutions for $c_A(t,0)$ and $c_B(t,0)$; $c_A(t,0) = \frac{\zeta_A + \chi_A \zeta_B}{1-\chi_A \chi_B}$ and $c_B(t,0) = \frac{\zeta_B + \chi_B \zeta_A}{1-\chi_A \chi_B}$.

[165] A. L. Cottrill, R. Goulet, F. Fremy, J. Meulemans, M. R. Sheldon, and M. Z. Bazant, Int. J. Heat Mass Transf. **163**, 120445 (2020).

[166] C. Venkataraman, A. V. Soudackov, and S. Hammes-Schiffer, J. Chem. Phys. **131**, 154502 (2009).

[167] C. Venkataraman, A. V. Soudackov, and S. Hammes-Schiffer, J. Phys. Chem. C **114**, 487 (2010).

[168] D. V. Matyushov and M. D. Newton, J. Chem. Phys. **147**, 194506 (2017).